2005-03-29

Electrothermomechanical Modeling of a Surface-micromachined Linear Displacement Microactuator

Christian D. Lott
Brigham Young University - Provo

ELECTROTHERMOMECHANICAL MODELING OF A SURFACE-MICROMACHINED LINEAR DISPLACEMENT MICROACTUATOR

by

Christian D. Lott

A thesis submitted to the faculty of

Brigham Young University

in partial fulfillment of the requirements for the degree of

Master of Science

Department of Mechanical Engineering

Brigham Young University

August 2001

BRIGHAM YOUNG UNIVERSITY

GRADUATE COMMITTEE APPROVAL

of a thesis submitted by

Christian D. Lott

This thesis has been read by each member of the following graduate committee and by majority vote has been found to be satisfactory.

_____	_____
Date	Timothy W. McClain, Chair
_____	_____
Date	Larry L. Howell
_____	_____
Date	John N. Harb

BRIGHAM YOUNG UNIVERSITY

As the chair of the candidate's graduate committee, I have read the thesis of Christian D. Lott in its final form and have found that (1) its format, citations, and bibliographical style are consistent and acceptable and fulfill university and department style requirements; (2) its illustrative materials including figures, tables, and charts are in place; and (3) the final manuscript is satisfactory to the graduate committee and is ready for submission to the university library.

_____ _____

Date

Timothy W. McLain
Chair, Graduate Committee

Accepted for the Department

_____

Craig C. Smith
Graduate Coordinator

Accepted for the College

_____

Douglas M. Chabries
Dean, College of Engineering and Technology

ABSTRACT

ELECTROTHERMOMECHANICAL MODELING OF A SURFACE-MICROMACHINED LINEAR DISPLACEMENT MICROACTUATOR

Christian D. Lott

Department of Mechanical Engineering

Master of Science

The electrothermomechanical characteristics of an electrically-heated polycrystalline-silicon microactuator are explored. Using finite-difference techniques, an electrothermal model based on the balance of heat dissipation and heat losses is developed. For accurate simulation, the relevant temperature dependent properties from the microactuator material are included in the model. The electrothermal model accurately predicts the steady-state power required to hold position, and the energy consumed during the thermal transient. Thermomechanical models use the predictions of temperature from the electrothermal solution to calculate displacement and force from pseudo-rigid-body approximations and commercial finite-element code. The models are verified by comparing experimental data to simulation results of a single leg-pair on a particular configuration of the device.

The particular microactuator studied is called a Thermomechanical In-plane Microactuator, or TIM, and was fabricated with surface micromachining technology. A

TIM requires a single releasable structural layer, is extremely flexible in design, and can operate with simple drive and control circuitry. The TIM produces linear motion of a center shuttle when slender legs on either side move the shuttle as a result of constrained thermal expansion.

In a single example, when the current through a leg with dimensions $250 \times 3 \times 3.5\,\mu m^3$ and suspended 2 μm off the substrate is sufficient to maintain an average temperature of 615 C in air and vacuum environments, model simulated temperatures along the leg have a peak of 860 C in air and 1100 C in vacuum. The final measured and predicted displacement is 14 μm. In air, the power predicted by the model needed to maintain this average temperature profile is 95 mW while consuming 16.4 μJ in 0.22 ms to reach 90 percent of the final average temperature. In a vacuum, only 6.4 mW are required to maintain the same average temperature with 97.6 μJ consumed in 18.5 ms. Simulation results suggest that short-duration high-current pulses can improve the transient response and energy consumed in a vacuum when steady-state temperatures are not required. For a TIM leg with the dimensions above, the maximum measured force is approximately 47 μN per leg-pair when enough current is provided to move the TIM 8 μm as a result of ohmic heating and thermal expansion.

ACKNOWLEDGMENTS

I acknowledge and thank my Heavenly Father for His hand in the completion of this work. He has provided me with guidance and inspiration many times through the course of my studies and given me needed encouragement when I thought I was capable of less.

I am certain that I will forever be in awe for the opportunity to work with the members of my committee. I admire these men greatly and appreciate their patience with me and encouragement of this work. Thanks to Dr. McLain for many hours of consultation and for his insights and input into this work. Thanks to Dr. Howell for giving me the opportunity to participate in MEMS research. Thanks to Dr. Harb for always letting me know that this research was important and for his sharp insight and critiques.

I express my gratitude for all those in CB 152 for many hours of enjoyment. Numerous individuals have lent a listening ear and contributed suggestions to the development of the models. Specifically, I would like to take the opportunity to thank Scott Lyon, Nathan Masters, Mike Baker, Cynthia Christianson, Jenny Cutler, Jon Wittwer, and Sydney Stanton.

Finally, I consider my family to be my greatest blessing. My parents' continual support and prayers in behalf of my schooling has provided me with motivation and the encouragement to go on. A special thanks goes to my wife Rachel. Her sacrifices for our family while I struggled with the details of this work are the main reason this thesis was ever finished. Thank you to my daughter Natalie for the breaks on the swing set in the park and singing songs to cheer me up.

CONTENTS

LIST OF FIGURES

Chapter 1

INTRODUCTION

Actuators perform useful work on their environment in response to a command or a control signal. The energy they require to do the desired work and the amount of work they perform depend heavily on the method of actuation. Numerous strategies for actuation at the microscale exist and are often separated into categories such as electrostatic, magnetic, piezoelectric, phase change, and thermal expansion. Actuation by thermal expansion has many advantages and a motivation for the study of the phenomena in surface-micromachined polysilicon will be examined in Section 1.1. Section 1.2 describes the goals pertaining to this work and introduces the objectives of this thesis. In Section 1.3, the methods used to accomplish the objectives are briefly discussed. Section 1.4 outlines the contributions of this thesis. Finally, Section 1.5 provides a reader's guide for the remainder of this thesis.

1.1 MOTIVATION

Although the vast majority of today's microelectromechanical system (MEMS) products are probably best categorized as components or subsystems, a major struggle for researchers in this field is with the systems aspect of the technology. The work in this thesis provides a crucial step towards making it possible to have functional and reliable microsystems by providing theoretical and experimental research on the modeling of an enabling microactuator, identified in prior research as a Thermomechanical In-plane Microactuator or TIM [10]. Recently, the TIM has demonstrated its ability to be

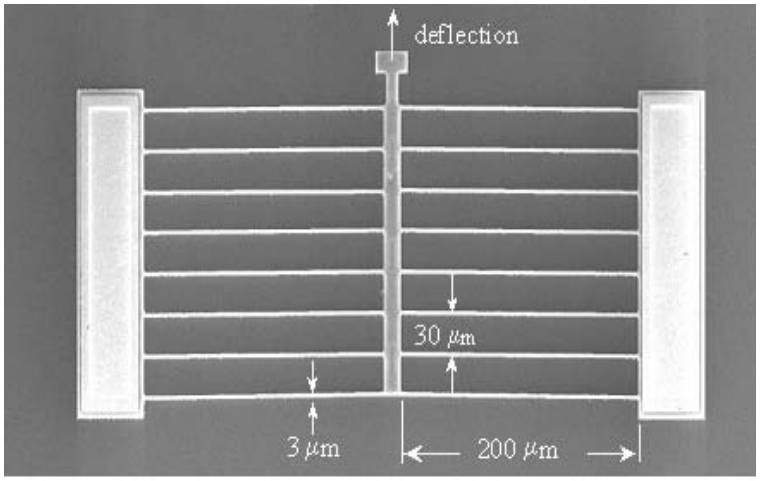

Figure 1.1 - Thermomechanical In-plane Microactuator or (TIM)

integrated at a system level with several micromechanisms, including a bistable mechanical switch. At BYU's Integrated Microelectronics Laboratory (IML), a single TIM has successfully actuated an optimized partially-compliant bistable four-bar mechanism [25] between both stable positions. Additionally, an amplified arrangement of the TIM has toggled a linear displacement bistable micromechanism [2], requiring 55 μm of deflection.

This microactuator can be fabricated with any process that allows a single releasable material layer to be placed on top of an electrically insulating substrate. As shown in Figure 1.1, the basic TIM design consists of a moveable shuttle connected to electrical contact pads on the substrate by slender thermal expansion legs. As a voltage difference is applied across the contact pads, current flows through the legs and the center shuttle. The high current density in the legs causes ohmic heating and thermal expansion, resulting in linear motion of the shuttle in the direction that is determined by the slight inclination angle at which the legs are attached.

Electrothermal microactuators have distinguished themselves from their common electrostatic counterparts in MEMS applications because of their combined large displacements and force output, together with their ability to be driven at CMOS compatible voltages and currents [8]. Because of these benefits, this type of actuation is

an enticing choice for system-level design despite significant inefficiencies. In fact, thermal actuation consumes considerably more power than electrostatic or piezoelectric actuation strategies. The need exists, therefore, to understand how to improve thermal efficiency in thermally actuated microsystems. Specifically, research to determine a method for raising the temperature in these microactuators to get a desired deflection using minimal energy is warranted. At the very least, to design effectively at the system level, the power to hold the actuator at a steady position and the energy expenditure required to get it there must be identifiable for any particular TIM configuration.

The TIM has the benefit of being extremely flexible in design. As the length of the expansion legs is increased, the available displacement also increases. As the length of the expansion legs is decreased, the TIM is made more rigid in buckling towards lower modes – thus enhancing the available output force. The available actuation force also increases linearly with the number of leg pairs. The effect of these design changes on the TIM's power requirements, however, is not immediately identifiable.

For system-level design, a number of items must usually be considered. If the TIM itself is acting as a micropositioner, then precise deflection and the range of motion is key. If the TIM is exerting force on an object, then maximum force versus displacement curves will be a required specification. A model that will allow for designs to be evaluated based on the actuator's performance requirements is needed.

In addition to characterizing force, displacement, and power requirements, the dynamic behavior of the TIM must be modeled. This information will allow the TIM to be used for system-level design in switching applications where speed is a performance metric. With an accurate model of the electrothermal response of the TIM, the knowledge of the transient behavior will then be useful for feedback control of this microactuator.

1.2 RESEARCH OBJECTIVES

In response to the needs discussed above, a comprehensive electrothermomechanical model of a TIM is needed. This thesis undertakes as its primary goal, the extensive electrothermomechanical modeling of a TIM. By analytical, finite-difference, and finite-element approaches, the models developed here are capable of fully simulating a TIM device. Through simulations of the TIM under varying ambient conditions and geometric designs, knowledge of how the microactuator performs is developed and verified, in many cases, by experimental means. Another goal for this research is to use the model and simulations for use in developing a reliable model that is appropriate for feedback position control of the TIM. Finally, a review of the model by MEMS designers will also be a noteworthy pursuit; its study will give valuable feedback in the form of design intuition, guidelines, and strategies that will be helpful in developing a modular family of actuators designed for specific tasks.

1.3 METHODS

In this thesis, mathematical based models are developed to predict the performance of the TIM. The controlling differential equation for one-dimensional heat flow by conduction is used to determine the steady-state temperature profile of the TIM in response to an input current. The equation is solved both analytically and by the finite-difference method. Although subject to stability requirements, an explicit formulation will be used over an implicit approach because of the desire for a fine resolution in the time step in order to study transient heating; this choice also eliminates the need for repeated matrix inversion and back-substitution and allows easy updates of material properties that change with temperature [14]. A collection of the important material properties that dictate the electrothermomechanical response of surface micromachined polysilicon has been gathered from the most recent literature.

Because of the difficulty in obtaining direct temperature measurements from the micron-sized geometry, an indirect approach is used to experimentally validate the temperature profile. The nodal temperatures that result from the finite-difference method are used as body-force loads in a finite-element package (Ansys 5.5) along with a pseudo-rigid-body-model approach to predict the resulting displacement from thermal strains. Transient deflections result when the pseudo-rigid-body approach is coupled to the transient temperature distribution as predicted with the finite-difference model.

1.4 CONTRIBUTIONS OF THIS THESIS

This thesis makes the following contributions specific to the TIM that can be directly applied to electrothermomechanical microactuators in general:

1. Based on a priori knowledge of critical material properties, the models developed in this research can predict the temperature profile of the TIM along the current path resulting from an applied voltage. This temperature profile of the TIM is valid up to the melting temperature of the actuator material as long as there exists the same confidence in the actuator's material properties. Although the most recently reported data available for the material properties of polysilicon are only measured to approximately 600 C, experimental tests in this thesis with the ability to predict melting (at 1411 C) came as close as 1.5 percent. The model allows for critical parameters to be included as a function of temperature for more accurate modeling of physical phenomena. These parameters include thermal conductivity of polysilicon, resistivity of polysilicon, thermal conductivity of air, and specific heat of polysilicon.

2. Building on the first contribution, the models in this thesis can predict the actuator's resulting displacement and force characteristics from the thermal expansion of the TIM's legs in response to an input current. A safe input current is defined to be current magnitudes below a critical threshold, where the resulting

Ohmic heating would affect material properties to the point where they are no longer predictable.

3. Motivated by understanding the power demands of the actuator, the following performance criteria have been identified: 1) the total energy required to achieve a specific no-load deflection, 2) the steady-state power required to hold steady position, and 3) the microactuator's response time, or speed to steady-state. These performance criteria have been measured for numerous TIM devices. The criteria serve as guidelines for the design process.

4. Attempts to reduce the total power requirements of the TIM have led to its study in vacuum ambients. The transient heating performance and the power savings available when actuated in this environment have been characterized and quantified by this research. This is a valuable metric for power-strapped applications, but requires the ability to package the device in a vacuum.

5. Early work with the TIM has been the result of prototypes with surface micromachining technology using the Multi-User MEMS Process (MUMPs) [32]. The models presented in this thesis are not process limited, and can model dynamics of devices fabricated with other micromachining processes such as LIGA, Sandia's SUMMiT, or even wet etching in patterned silicon wafers. This will offer a savings in cost over otherwise evaluating designs using trial-and-error attempts with each new available process.

6. Along with the electrothermal response of the TIM, a model is presented for the mechanical dynamics of the microactuator. Building on prior research [39], the first modal frequency of the TIM has been identified. An equation is given in terms of design parameters that will predict this natural frequency. Because the electrothermal bandwidth is well below the mechanical resonant frequency of a TIM, the TIM device cannot be driven to resonance by electrothermo impulses.

1.5 READER'S GUIDE

This chapter has discussed the motivation for an in depth study of electro-thermo-mechanical issues related to a specific surface micromachined microactuator, called a Thermomechanical In-plane Microactuator or TIM. The next chapter reviews the operation of the TIM, the surface micromachining fabrication process, and addresses the required knowledge of material properties necessary for thermal modeling. Chapter 3 presents the models used to study the TIM's behavior. Chapter 4 compares experimental results with model predictions. Finally, Chapter 5 contains conclusions and recommendations for further research.

Chapter 2

BACKGROUND

This chapter reviews the operation of the TIM and how the test actuators of this thesis were fabricated. The physical parameters important to the TIM's performance are also described and published values from a recent literature survey are given. Much of the work applicable to the study of electrothermomechanical microactuators was initially developed for the electrothermal modeling of polysilicon microbridges used with sensor applications. This collection of work is surveyed and other models for actuators similar in performance to the TIM are examined.

2.1 REVIEW OF THE TIM

The TIM is a microactuator that uses thermal energy (heat) to induce thermal expansion of its members and create motion. This strategy for actuation at the micro scale is not uncommon [8,12,26,27,34,58]. In a brief review, Cragun has offered an assessment of various microvalves, micropumps, and microactuators that use thermal energy [10] to create motion. As previously discussed in Chapter 1, the basic TIM design consists of a moveable shuttle connected to electrical contact pads on the substrate by slender thermal expansion legs. Figure 1.1 of Chapter 1 shows a labeled micrograph. As a voltage difference is applied across the contact pads, current flows through the legs and the center shuttle. The high current density in the legs causes ohmic heating and thermal expansion, resulting in linear motion of the shuttle in a direction that is determined by the slight inclination angle at which the legs are attached.

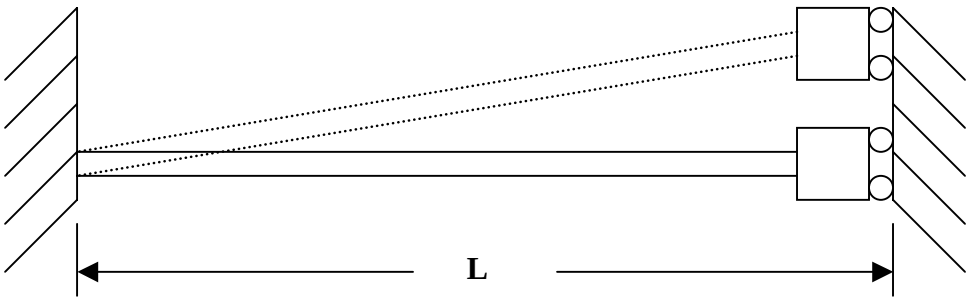

Figure 2.1 - Geometric constraint and amplification example

An important concept in many electrothermal actuators is the use of geometric constraints to amplify the work of thermal expansion. This idea is inherent in operation of the TIM. The shuttle serves as a geometric constraint, helps to amplify the linear motion, and localizes the output force. Figure 2.1 shows a simple mechanism that will be used to demonstrate this point. Assume the length L, originally set at 250 μm, is increased by thermal expansion a small amount ΔL. If ΔL is 0.5 μm, and we assume no loss in displacement from the bending of the beam's shape, the resulting deflection d, found from Pythagoras' theorem, will be 15.8 μm. This simple example shows how a small increase in length from thermal expansion results in a motion over 30 times larger by the placement of geometric constraints. Of course, the actual displacement will be slightly less than the 15.8 μm predicted here (14.5 μm predicted by finite-element-analysis) when the bending in the beam is accounted for.

2.2 FABRICATION

The TIM is an extremely simple design that can be fabricated in any MEMS process which consists of at least one releasable, current carrying layer. This includes processes such as LIGA, Analog Device's *i*MEMS, or Sandia's SUMMiT. All devices simulated and tested in this thesis were the result of using the Multi-User MEMS Processes or MUMPs.

2.2.1 Surface micromachining

In surface micromachining, thin films of material are deposited by a variety of methods that can include: epitaxy, oxidation, sputtering, evaporation, chemical vapor deposition (CVD), or low-pressure chemical vapor deposition (LPCVD). With polysilicon, a thin film is deposited with an alternating layer of sacrificial silicon oxide. A layer of photoresist is then applied and covered by a photomask that patterns the device features for that layer. The masked photoresist is exposed to light and developed, revealing the unwanted layer material to be etched away with methods such as: plasma etching, reactive ion etching (RIE), deep reactive ion etching (DRIE), or wet etching (isotropic or anisotropic). The photolithography process is repeated for each layer of sacrificial and structural material until a complete device is formed. A typical stack contains a total of four or five layers, but may be more complex. After all layers are completed, a final release etch is performed which removes the sacrificial material from within and around the device so that the remaining structural material is free to move and perform mechanical functions. Figure 2.2 shows the basic steps of surface micromachining technology. If desired, the first five steps can be repeated to create additional layers. Step six represents the final etch of sacrificial oxide that frees the structure. This cycle of process steps has been illustrated previously by Maluf and used to explain the creation of a suspended beam [43].

MUMPs is a surface-micromachining process that utilizes three structural layers of polysilicon. The first polysilicon layer is 0.5 μm thick and cannot be released from the substrate. This layer is commonly used for address electrodes and local wiring. The second and third polysilicon layers are both releasable and are 2.0 μm and 1.5 μm thick, respectively. These layers are released to form mechanical structures. Following the deposition of each polysilicon layer, a high temperature anneal is used to alleviate residual stresses in the deposited polysilicon. An oxide layer of 2.0 μm is deposited between the first and second polysilicon layers, while an oxide layer of 0.75 μm is deposited between the second and third polysilicon layers. Finally, a 0.5 μm thick layer of gold can be deposited on the third polysilicon layer. These active layers are built up

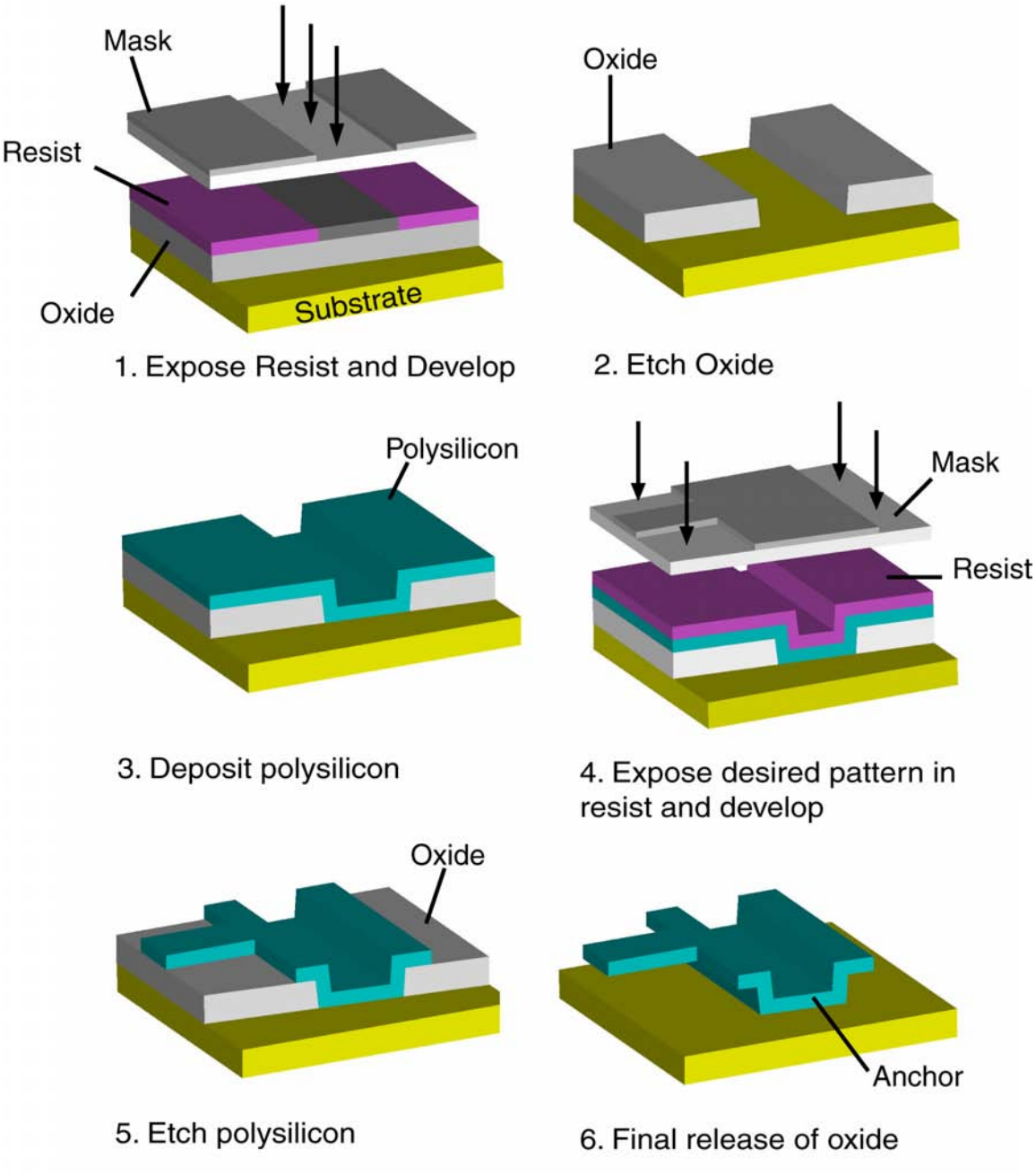

Figure 2.2 – Cycle of steps that occur in a basic surface micromachining process. Adapted from [43].

over a silicon nitride layer, which insulates them from the conductive silicon substrate. For reference and clarity, all of the steps performed in a MUMPs run are enumerated below.

1. A 100 mm diameter silicon wafer is heavily doped with phosphorous in a standard diffusion furnace using $POCl_3$ as the dopant source.
2. A 600 nm silicon nitride layer is deposited by low-pressure chemical vapor deposition (LPCVD).
3. A 500 nm polysilicon layer (Poly0) is deposited by LPCVD and patterned by photolithography.
4. Poly0 is etched by reactive ion etching (RIE).
5. The first oxide layer (Oxide1), 2.0 μm thick phosphosilicate glass (PSG), is deposited by LPCVD.
6. The dimple layer is patterned into Oxide1 and etched by RIE.
7. The first anchor etch (Anchor1) is patterned and etched by RIE.
8. Poly1 is deposited at a thickness of 2.0 μm, covered with a thin layer of PSG, and annealed at 1050 C.
9. Poly1 is lithographically patterned and etched by RIE.
10. Any remaining PSG from step 8 is removed by RIE.
11. Second oxide layer (Oxide2) is deposited 0.75 μm thick and patterned twice: (1) for VIA etch that will connect Poly2 to Poly1 and (2) for Anchor2 etch. Both are etched by RIE.
12. Poly2 is deposited at a thickness of 1.5 μm, covered with a thin layer of PSG, and annealed at 1050 C.
13. Poly2 is lithographically patterned and etched by RIE.
14. Any remaining PSG from step 12 is removed by RIE.
15. A final layer of metal (gold) is deposited 0.5 μm thick and patterned using lift-off.
16. A protective layer of photoresist is applied and the wafer is diced for shipment.

Figure 2.3 is an illustration of a simple structure fabricated with the MUMPs surface-micromachined technology. The device being shown is a representation of an

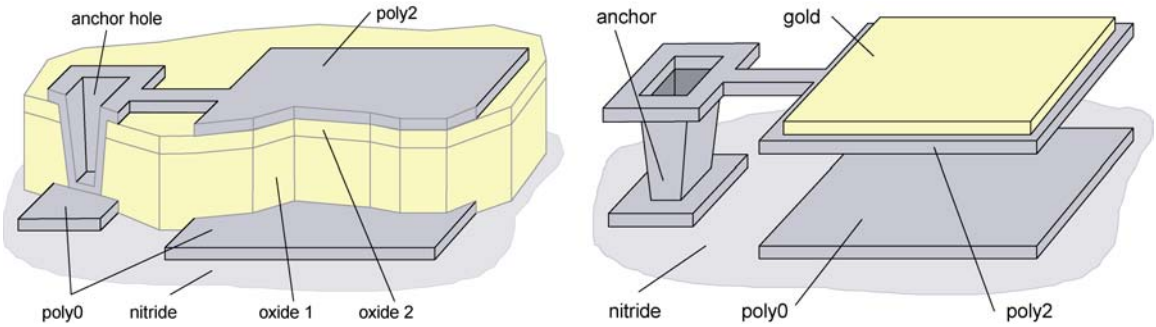

(a) cross-section prior to metal layer (b) released device

Figure 2.3 - 3D illustration of a surface-micromachined process like MUMPs [7]

electrostatically actuated micromirror device fabricated, originally produced by Comtois, et al. [7]. Note that this design uses only the first polysilicon layer (poly0) and third polysilicon layer (poly2). Also, not shown in Figure 2.3 is the topology induced in the poly2 layer by the underlying poly0. Thin film layers conform closely to the topology of the previously deposited layers, so they are not necessarily planar. This is sometimes a cause for device failure but was not a problem with the fabricated TIMs.

2.2.2 Release process

The release of micromechanisms from the oxide that binds them is as much an art form as it is a science. This is because in a standard drying release, the skill and experience of the technician contributes greatly towards device yield. In a standard release, the wafers or cut die are immersed in diluted or buffered solutions of hydrofluoric acid, which etch the oxide and free the structural material. The acid is rinsed in de-ionized water and the final liquid is allowed to evaporate at room temperature. During the final rinse or upon exposure to air, a layer of oxide is formed on the surface of the silicon that is extremely hydrophilic [40]. Capillary forces then pull the micromechanisms down to the substrate, which causes them to stick. This is commonly called *stiction* and it can be permanent. In addition to the strong adhesion force caused by capillary action, electrostatic, van der Waals, and chemical forces have also been identified as contributing causes of stiction.

Further understanding of this phenomenon has been the focused study of many researchers and, thanks to their efforts, many potential problems can be now controlled. A comprehensive review on the state of knowledge of surface phenomena behind adhesion in surface micromechanical structures can be found in the work of Maboudian and Howe [40]. This study focused its attention on polysilicon as a microstructural material. Although not the first to do so, their review identifies self-assembled monolayers, or SAM coatings, as a good approach to surface passivation and preventing stiction. The most extensively studied SAM coatings deposited on silicon are octadecyltrichlorosilane (OTS) precursor molecules having a chemical formula of $C_{18}H_{37}SiCl_3$ [55]. When these precursor molecules are placed into a suitable solvent such as a 4:1 hexadecane:carbon tetrachloride mixture, and an oxidized silicon surface is inserted, the result is a hydrophobic surface effective at preventing stiction. These films have shown long-term stability in various ambients and appear to be a good option for antistiction coatings in microstructures. OTS SAM coatings were used with the release of all TIMs following the standard HF etch described above.

2.2.3 Design limitations

The MUMPs foundry service is designed for general-purpose proof-of-concept surface micromachining fabrication. For this reason, the layer thickness and line widths are not optimized for the TIM (or any other specific device). A general rule of thumb with MUMPs is to make all minimum geometries greater than or equal to 5 μm. This is primarily due to alignment issues between masks and the resolution of the lithography system used. Because the TIM's legs can be etched with one mask, alignment is not a concern for the actuator, and most legs were created with a width of the nominal recommended minimum geometry size of 3 μm [6]. With the defined heights of poly1 and poly2 above, this means the maximum height achievable is a single stack of 3.5 μm polysilicon film. A height of 3.5 μm and a width of 3 μm result in an aspect ratio that helps the motion of the actuator to remain in the plane parallel to the substrate, although a greater aspect ratio would be preferred.

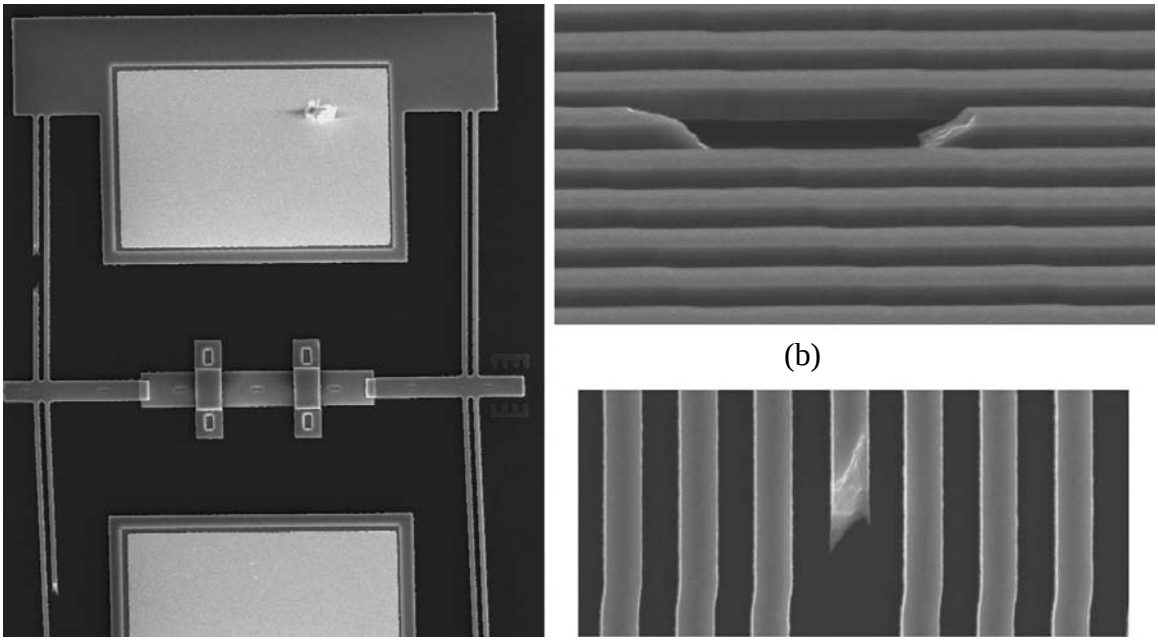

(a) (b) (c)

Figure 2.4 – Common fracture problem seen in slender legs (a) top view of a TIM has fractures in the legs on the left (b) zoomed side view of slender legs with dimensions the same as the TIM and (c) top view of the same row of legs.

The step in the layout used to put poly2 on poly1 is not a guaranteed process from the MUMPs service. The process relies on the fact that overetching of the poly2 is sufficient to completely etch an underlying layer of poly1. In testing TIM devices with this geometry, problems occasionally arise. The most commonly seen problem is a jagged fracture of the slender stacked beams seen in Figure 2.4. Correspondence with the MUMPs foundry suggests that these fractures are the result of the final ultrasonic liftoff procedure used for the final gold metal layer. The fracturing may be the result of the isolated 3.5 μm high beams not being able to hold up consistently during the liftoff step – the result being the development of cracks in the beams. The torn and jagged nature of the break does not suggest that this is a problem with the HF release. This hypothesis, however, has not been conclusively resolved.

2.3 REVIEW OF IMPORTANT MATERIAL PROPERTIES

In setting up the electrothermal model to characterize the performance of a TIM, certain key temperature-dependent material properties were identified early in the modeling process. In Chapter 3, a finite-difference approach to the modeling of the TIM is described that allows for updates of the material properties to occur as time advances and the simulated temperatures change in response to an applied current. This permits a more complete and accurate model of the TIM's response so long as the there exists a good knowledge of the material's characteristics with respect to temperature variations. This section will review the present understanding of parameters important to the modeling of a TIM.

2.3.1 Thermal conductivity of polysilicon

In the modern view of materials, a solid may be comprised of free electrons and of atoms bound in a periodic arrangement called the lattice [52]. Accordingly, the transport of thermal energy is due to two effects: the movement of free electrons, and vibrational waves of the lattice [24]. These two effects are additive so that the total thermal conductivity k of a material is the sum of the electrical component k_e and the component from the lattice k_l. With crystalline (well-ordered) materials, the regularity of the lattice arrangement results in higher thermal conductivities than amorphous materials like glass [24]. Moreover, the effects of temperature on crystalline materials can be significant. The thermal conductivity of crystalline silicon has been consistently reported to drop from approximately 150 to 22 W/m/K between room temperature (298 K) and the melting point of silicon (1685 K) [54]. The variation in thin-film polysilicon, however, has been reported with less consistency. This is most likely due to variations in impurity concentration and grain size from different fabrication processes [51].

The thermal conductivity of polysilicon films produced in CMOS IC technology has been measured in the temperature range from 80 to 400 K. Electronic and lattice thermal conductivity were determined using electrical and galvanomagnetic data obtained from

the same film [46]. This study found little variation with temperature above room temperature and reported 29 W/m/K for the thermal conductivity with an electronic content, k_e, of less than three percent. The n-type dopant concentration of this CMOS polysilicon was not explicitly stated. In another study of heavily phosphorous doped (10^{20} atoms/cm^3) low-pressure chemical vapor deposited polysilicon (LPCVD) a film, the thermal conductivity was measured in a range from 29 to 34 W/m/K, with an average of 32 W/m/K [53]. However, this study did not report measurements beyond 150 C. In a final study of polysilicon that may be of interest, the thermal conductivity of Sandia's large grained, laminated polysilicon was fit to data that was measured from room temperature to 800 K [41]. This silicon was also heavily doped on the order of 10^{20} atoms/cm^3. The full dependency on temperature in degrees Celcius from this last study is

$$k_p(T) = \left[\left(-2.2\times10^{-11}\right)\cdot T^3 + \left(9.0\times10^{-8}\right)\cdot T^2 + \left(-1.0\times10^{-5}\right)\cdot T + 0.014\right]^{-1}. \quad (2.1)$$

The grain size, impurity concentration, and method of deposition for the MUMPs process are most consistent with the work of Tai, et al. [53]. This suggests that an average value of 32 W/m/K is appropriate to use. In fact, a constant thermal conductivity between 29 and 34 W/m/K is frequently selected for use with other electrothermal studies [5,8,22,36]. For the models in this thesis that assume a constant thermal conductivity, a value of 32 W/m/K is used. Because of a limited knowledge of polysilicon's thermal conductivity variations with higher temperatures, the validity of Equation 2.1 will also be examined. The results from the model should help indicate if a constant value is appropriate for the study of the TIM or if more research into its dependence on temperature is warranted.

2.3.2 Resistivity of polysilicon

The resistivity of polysilicon is much greater than that of similarly doped, single-crystal, epitaxial silicon [28]. Resistivity changes slowly at low dopant concentrations, but decreases rapidly at intermediate dopant concentrations. At high dopant concentrations (10^{20} atoms/cm^3), it approaches the resistivity of single-crystal silicon for similar dopant

levels, suggesting a resistivity-limiting point at the solid solubility of the particular dopant in silicon [28]. Fortunately, for electrothermal actuators in polysilicon, setting room temperature resistivity by controlling doping levels is an issue that is well studied; the doping process is used extensively in the IC industry and allows the actuator to operate at voltages and currents compatible with standard integrated circuitry (CMOS). However, at high temperatures (beyond 750 to 800 C) the resistivity is less predictable and not well understood because of self-annealing and irreversible changes in the polysilicon structure that occur.

The resistivity of polysilicon, ρ, is usually related to temperature with a linear relationship controlled by a temperature coefficient of resistance, ξ. A relationship for the resistivity that is linear with temperature is

$$\rho(T) = \rho_0[1 + \xi(T - T_o)] \tag{2.2}$$

where T is the operating temperature, T_o is the reference temperature, and ρ_o defines the resistivity at the reference temperature. This expression has been used by many to model the temperature dependence of resistivity in sensor applications and microactuators with polysilicon [5,22,36,45]. Still, it is not expected to be accurate with polysilicon beyond the extreme temperatures noted above. Values of ξ in polysilicon for processes similar to MUMPs have been reported to range from 1.1 x 10^{-3} K^{-1} to 1.3 x 10^{-3} K^{-1} [5,22,45]. Consequently, a value of 1.25 x 10^{-3} K^{-1} was used for the models in this thesis.

At higher operating temperatures, polysilicon exhibits secondary-breakdown resulting in a decrease in resistivity [13]. This phenomenon occurs when a high current and self-heating cause local melting of boundary layers between crystal grains in the polysilicon. The resistance decrease is explained in terms of the local melting by a self-annealing and a segregation of impurity atoms in the subsequent solidification process [1,29]. Interestingly, the work of Kato and Ono reports that the resistance drop due to a large passing current can be restored to a higher value by passing a current slightly lower than

the previous one but still greater than the initial threshold current needed to cause melting at the boundary layer [29]. Because of the resistance drop, the applied second current will merely cause a heating up of the boundary layer resulting in a thermal diffusion of the concentrated impurity. Thus the resistance will be restored, albeit slowly, since the thermal diffusion in solids is a slow process. Unfortunately, there exists no straightforward modification to Equation 2.2 that can accurately reflect the secondary-breakdown.

2.3.2.1 Microprobe Contact and Resistivity Measurements

When testing a TIM device, microprobes touch a pair of bond pads located on each side of the microactuator. Figure 2.4a is a picture of the bond pads in view and Section 3.1 discusses the path of the applied current flow in more depth. The contact resistance between the microprobe tip and the gold bond pad of a TIM represents a resistance in series with a TIM device. To measure the value of this contact resistance as well as the resistivity of laminate (stacked poly1 and poly2) polysilicon from MUMPs, a "ladder" of resistors was fabricated. Three polysilicon microbridges of 55, 240, and 430 μm lengths were used. In this setup, the total resistance R of three lengths of resistors (a "ladder" of resistors), each on the same die and same cross-sectional area A_x, are measured. The values of the resistances are then plotted as a function of length. A straight line fit to the data intersects the axis representing resistance at the point of zero length. The intercept is assumed to be the contact resistance R_c. The ladder tests on two different MUMPs die found the average contact resistance to be 47.8 Ω. The resistance in the bridge R_b is then

$$R_b = R - R_c \tag{2.3}$$

Once the bridge resistance was known, a resistivity for each length of the microbridges is calculated with the formula

$$\rho = \frac{R_b A_x}{L} \tag{2.4}$$

where L is the length of the microbridge. An applied current value of 0.5 mA kept Joule heating effects negligible. From these tests, a value of $3.4\times10^{-5}\,\Omega\,\mathrm{m}$ is used for room temperature resistivity $\rho_0(T)$ for the laminate poly1 and poly2 beams from MUMPs.

2.3.3 Specific Heat

The specific heat of the material is an important parameter for the electrothermal analysis of the TIM. Maginell looked at isolated measurements of both polysilicon and single-crystal silicon and came to the conclusion that a practical error bound of 5 percent on the use of silicon's specific heat for polysilicon is acceptable [41]. Equations, curve fit to available data for the specific heat of silicon, are repeated here [3].

Between 292 K and 700 K:

$$c = (1.976362\times10^{-6})T^3 - (3.766786\times10^{-3})T^2 + (2.622954)T + 2.149586\times10^{2}$$

and Between 701 K to 1685 K:

$$c = -(3.377784\times10^{-5})T^2 + (2.388945\times10^{-1})T + 7.324063\times10^{2} \qquad (2.5)$$

The specific heat c is in units of J/kg/K. When a constant value of specific heat was assumed, a value of 705 J/kg/K is used.

2.3.4 Thermal conductivity of air

The thermal conductivity of air and its dependence on temperature is well known and is published in tables within most heat transfer texts [14,24]. This parameter has a large effect on the modeling results because the thermal conductivity of a gas is a strong function of temperature. Nevertheless, in most published analytical expressions, a constant value near room temperature (0.026 W/m/C) has been used.

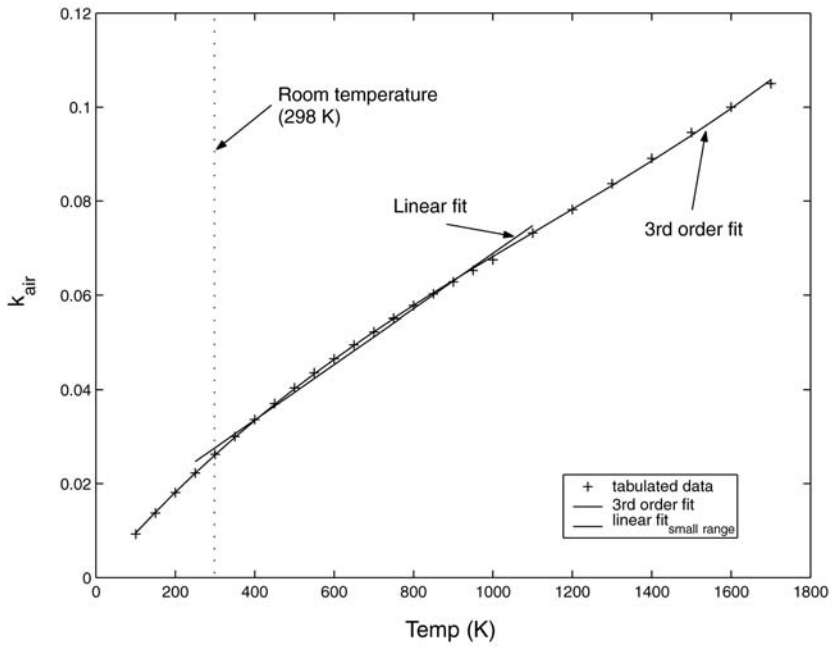

Figure 2.5 – Published data and curve fits to thermal conductivity of air

Using the tabulated values from Holman [14], a linear expression offers a good fit to the data up to 1100 K. The thermal actuators should rarely be taken beyond this temperature due to irreversible changes caused by self annealing and localized melting at grain boundaries. Therefore, a linear fit to data from room temperature up to 1100 K should be useful. A best fit to the published values results in the equation:

$$k_{air} = 9.97 \times 10^{-3} + 5.89 \times 10^{-5} T \qquad (2.6)$$

When desired, a third-order polynomial expression is easily fit to the same values in Holman, offering a closer fit to data for air over a broader range. This data is valid out to temperatures much higher then the melting point of silicon (1411 C). The polynomial best fit for air is

$$k_{air} = 3.9539\times10^{-4} + (9.886\times10^{-5})T - (4.367\times10^{-8})T^2 + (1.301\times10^{-11})T^3 \quad (2.7)$$

where T is the absolute temperature and the thermal conductivity is in W/m/K.

2.3.5 Thermal expansion coefficient

The temperature dependence of the thermal expansion coefficient for silicon has been measured and fit to empirically gathered data [46]. The expression is

$$\alpha(T) = \left(3.725\left\{1 - \exp\left(-5.88\times10^{-3}(T-125)\right)\right\} + 5.548\times10^{-4}T\right)\times10^{-6} \quad (2.8)$$

where T is the absolute temperature ranging from 120 to 1500 K. Although this data was measured with high-purity silicon, Equation 2.8 has been applied by others to model the growth of polysilicon [5,6].

To compute deflections at steady temperatures, this expression is only needed after an electrothermal model has been used to predict the final temperature response profile. Therefore, it is fairly easy to apply Equation 2.8 by using the computed nodal temperatures on each discretized element from the finite-difference process. To get transient deflections, Equation 2.8 must be used with each transient temperature profile to compute the corresponding thermal expansion. When the full expression was not used, a typical constant value of 2.7×10^{-6} (K^{-1}) (appropriate near room temperature (20 C)) has been employed [22].

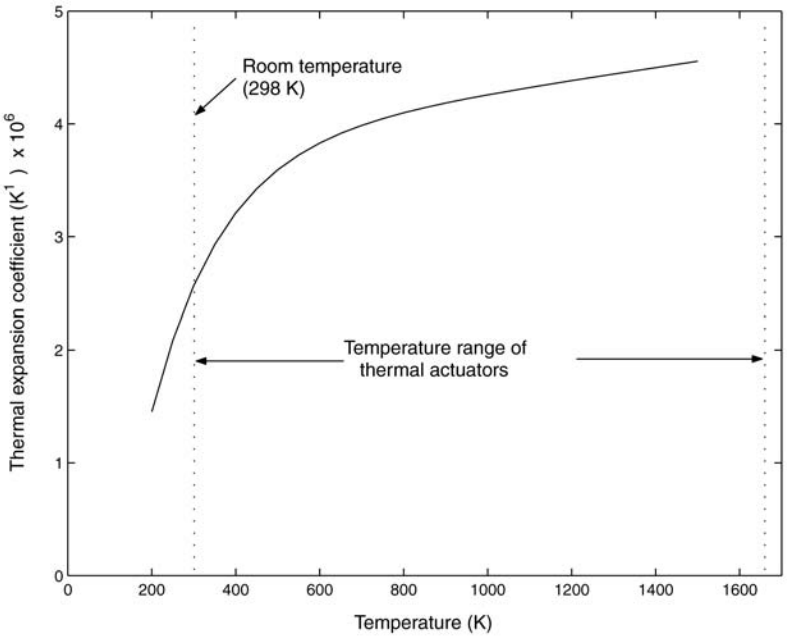

Figure 2.6 – Variation of thermal expansion coefficient with temperature

2.4 RECENT ELECTROTHERMAL MODELS

Much of the early progress towards the analysis of electrothermal responses in polysilicon is the result of studying the thermal applications of electrically-heated microbridges. Microbridges have been used in the MEMS sensor arena for applications such as calorimetric gas detection, flow sensors, pressure sensors, and incandescent light sources [41,45]. These studies created an electrothermal model based on the balance of heat dissipation and heat losses to determine temperature profiles of microbridge sensors. The models in both studies were implemented in SPICE, an electrical circuit simulator. Although the sensors are not designed for high-temperature use (the exception being the incandescent light source) it was noted in both studies that losses caused by radiation to the environment and free convection were negligible compared with conduction axially along the beam and down to the substrate.

Most electrothermal actuator research to date has addressed designs that can be characterized best as pseudo-bimorphs (see Figure 2.7). These actuators use the differing

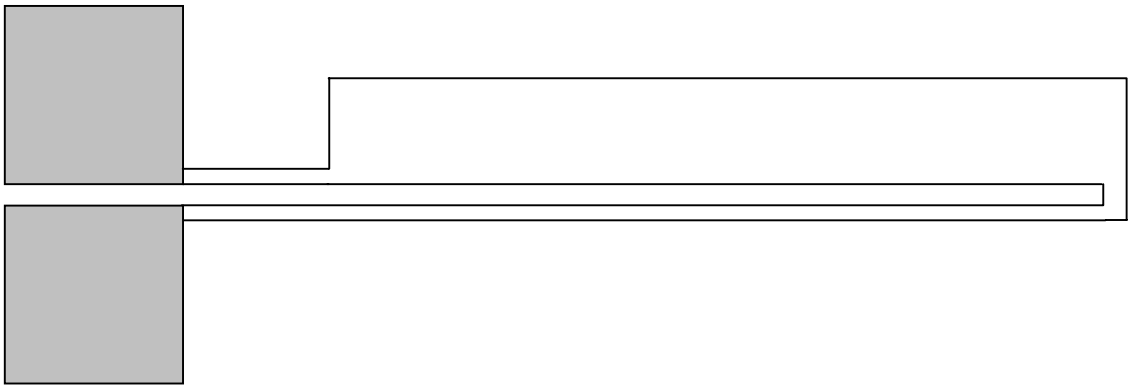

Figure 2.7 - U-shaped pseudo-bimorph electrothermal microactuator

expansion of two adjacent polysilicon beams of different widths to mimic a bimorph[1]. This type of actuator was first introduced by Comtois [8] and later analyzed in similar and slightly modified configurations [5,6,9,22,33,48,58]. Most of these studies also use SPICE or commercial finite-element code to study electrothermal behavior. The one exception is the effort by Huang and Lee [22]. In this reference, the authors use constant parameters and the linear expression for resistivity to develop the following second-order differential equation for heat transfer:

$$k_s \cdot \frac{d^2T(x)}{dx^2} + J^2\rho - \frac{G \cdot (T - T_s)}{h \cdot R_T} = 0 . \qquad (2.9)$$

This equation provides an analytical reference solution to the finite-difference model approach in the next chapter and is discussed in more depth at that point. The solution to Equation 2.9 yields temperature data as a function of length and is of the form:

$$T(x) = T_\infty + \frac{J^2\rho}{k_s m^2} + c_1 \cdot e^{mx} + c_2 \cdot e^{-mx} \ . \qquad (2.10)$$

This expression describes the temperature distribution for any silicon beam suspended in air and undergoing resistive heating from an applied current. Equation 2.10 represents

[1] A bimorph is a laminate of a layer of piezoelectric material and a passive layer. When a voltage is applied across the piezoelectric layer, it expands laterally, causing the structure to bend in the same way that a bimetallic strip bends.

the steady-state solution and can be solved utilizing linear algebra to obtain the constants of integration with appropriate boundary conditions.

2.5 RECENT THERMOELASTIC MODELS

Thermoelastic models in microactuators are more specific to the unique geometric configuration of the device than their coupled electrothermal counterparts. This is because the locus of motion for a particular actuator is dependent on its own layout and geometric constraints. Again, finite-element models have been previously used with mechanical beam elements and temperatures applied as body-force loads to predict displacement [33,35,44,48]. Empirically curve fitting the displacement data to the input current has also been used [8,33]. More recently, an approach utilizing the force method and virtual work for statically indeterminate structures common in structural engineering has been employed [22,23,30,42]. In this thesis, a simpler approach that is derived from the pseudo-rigid-body model for fixed-guided beams is used. This method is applied specifically to the layout of the TIM in Chapter 3.

Chapter 3

MODEL DEVELOPMENT

This chapter discusses the development and application of the models used for the TIM. The dynamic model of the TIM has two main parts: (1) the electrothermal model, which accounts for the joule heating of the TIM by an electrical current, and (2) the thermomechanical model, which models the displacement and force provided from thermal expansion.

3.1 FUNDAMENTAL BEAM MODEL

A TIM is typically composed of several pairs of legs. TIM devices have been fabricated with as few as two pair of legs and as many as 16 pair for the research in this thesis. Instead of separately modeling the entire actuator for each particular leg configuration, a model is developed for a single leg-pair of a TIM. Because one leg-pair captures the basic functionality of a multiple leg-pair device, it is called the fundamental beam design. This fundamental beam design is shown below in Figure 3.1. This component of the actuator contains all of the design parameters necessary for the simulation of a complete TIM. These parameters may be changed to create new designs. Figure 3.2 labels these parameters on a schematic drawing of the fundamental beam. When more than one fundamental beam shares the same bond pad, each single leg-pair is effectively wired in parallel.

Figure 3.1 - Fundamental beam design (single leg-pair) for a TIM

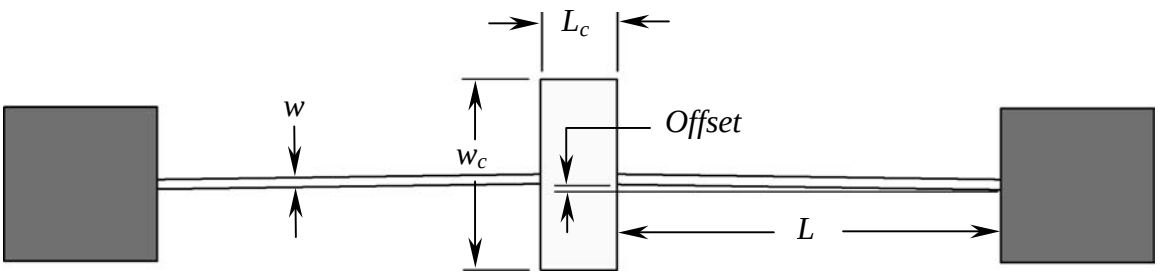

Figure 3.2 – Geometric design parameters on the fundamental beam of a TIM

The fundamental beam operates in the same manner as the full TIM. An applied voltage difference, as shown in Figure 3.1, is applied to the bond pads. The high current density in the legs causes ohmic heating and thermal expansion. The legs are connected to the shuttle at a slight angle, defined as an offset in Figure 3.2, so that their expansion is biased to cause a linear motion of the shuttle in the desired direction. For testing, the bond pads should be a size that allows quick and repeated access with probe tips. Larger bond pads are more useful when using the wire bonder. For reference, a gold contact area on the bond pads greater than 200 μm square is convenient.

As mentioned in Chapter 2, all of the TIMs simulated and tested were the result of using the fabrication steps from the Multi-User MEMS Processes or MUMPs [6]. As a result of this, the TIMs were designed to conform to recommended procedures regarding line widths and spacing as discussed in Section 2.2.3. This affects the fundamental beam design in two ways. First, because of the MUMPs design rules, the width *w* of the slender legs on the fundamental beam was kept at the nominal minimum feature size of 3 μm. Also, each TIM design utilized the VIA etch (step 11 on page 13) in order to create a single laminate beam of poly2 and poly1 that would be 3.5 μm thick. Having the width less than the thickness helps ensure that motion stays in the plane of the substrate and that force applied to the TIM will not cause the device to snap out-of-plane, or normal to the substrate.

The size of the shuttle is not limited directly by the MUMPs technology. For the fundamental beam design studied here, dimensions for both the shuttle's length and width

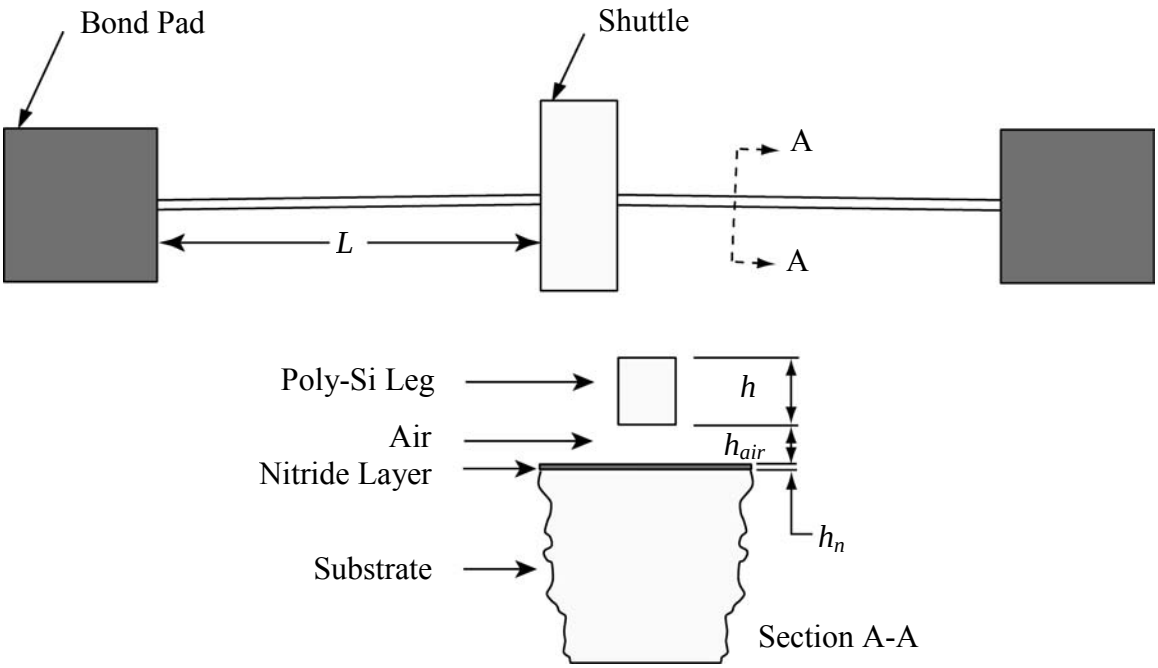

Figure 3.3 – Schematic of modeled TIM device and cross-section

(L_c and w_c) were chosen from the first working prototypes of the actuator. Unless otherwise stated, L_c will be 50 μm and w_c will be 30 μm. These values are used in the models for simulation of a single leg-pair.

3.2 ELECTROTHERMAL MODELS

In the electrothermal analysis, the steady-state temperature distribution along the legs of the actuator and center shuttle are found by solving the heat equation from a differential analysis and boundary conditions. Figure 3.3 is a schematic of the model used. The figure also illustrates the fundamental beam's cross-section, air gap beneath the cross-section, and substrate. In this section, an analytical expression for steady-state temperature is derived from a differential element. This effort borrows from the work of Huang and Lee [22] and extends it to the TIM. The limits of validity of the analytical solution are discussed. Also in this section, an alternative numerical approach is developed and its advantages explored. The numerical approach follows an explicit

finite-difference approach. Although subject to stability requirements, the explicit formulation was chosen over an implicit approach because of the desire for a fine resolution in the time step with the purpose of studying transient heating; this choice eliminates the need for repeated matrix inversion and back-substitution and allows easy updates of material properties that change with time [14].

3.2.1 Analytical Model

In modeling the heat flow from the microactuator, a one-dimensional treatment for heat conduction in the legs is used since the length dimension is much larger than any dimension of the cross-section. Following common practice, a conduction shape factor that accounts for conduction from the sides of the legs to the substrate and environment is included for more accurate modeling [38,45]. The factor represents the ratio of total heat flux (heat losses found by FEA) from the perimeter of a cross-section to expected heat loss from the bottom of the beam only. The beam differential element for thermal analysis is shown in Figure 3.4 and illustrates the paths of heat flow modeled for an element of width w, thickness h, and length dx. These paths include conduction in the beam, internal heat generation, and conduction to the substrate that is combined with the shape conduction factor.

Under steady-state conditions, heat conduction out of the differential element is equal to the resistive heating in the element. Using Figure 3.4 to guide the model development results in

$$-k_p A \left.\frac{dT}{dx}\right|_x + \dot{q}A dx = -k_p A \left.\frac{dT}{dx}\right|_{x+dx} + Sw\frac{T - T_s}{G_u} dx \qquad (3.1)$$

where k_p is the thermal conductivity for polysilicon, A is the beam's cross-sectional area, T is the operating temperature, T_s is the substrate temperature, S is the shape factor, and G_u represents the thermal resistance underneath the element. The expression for $\dot{q}$ is the

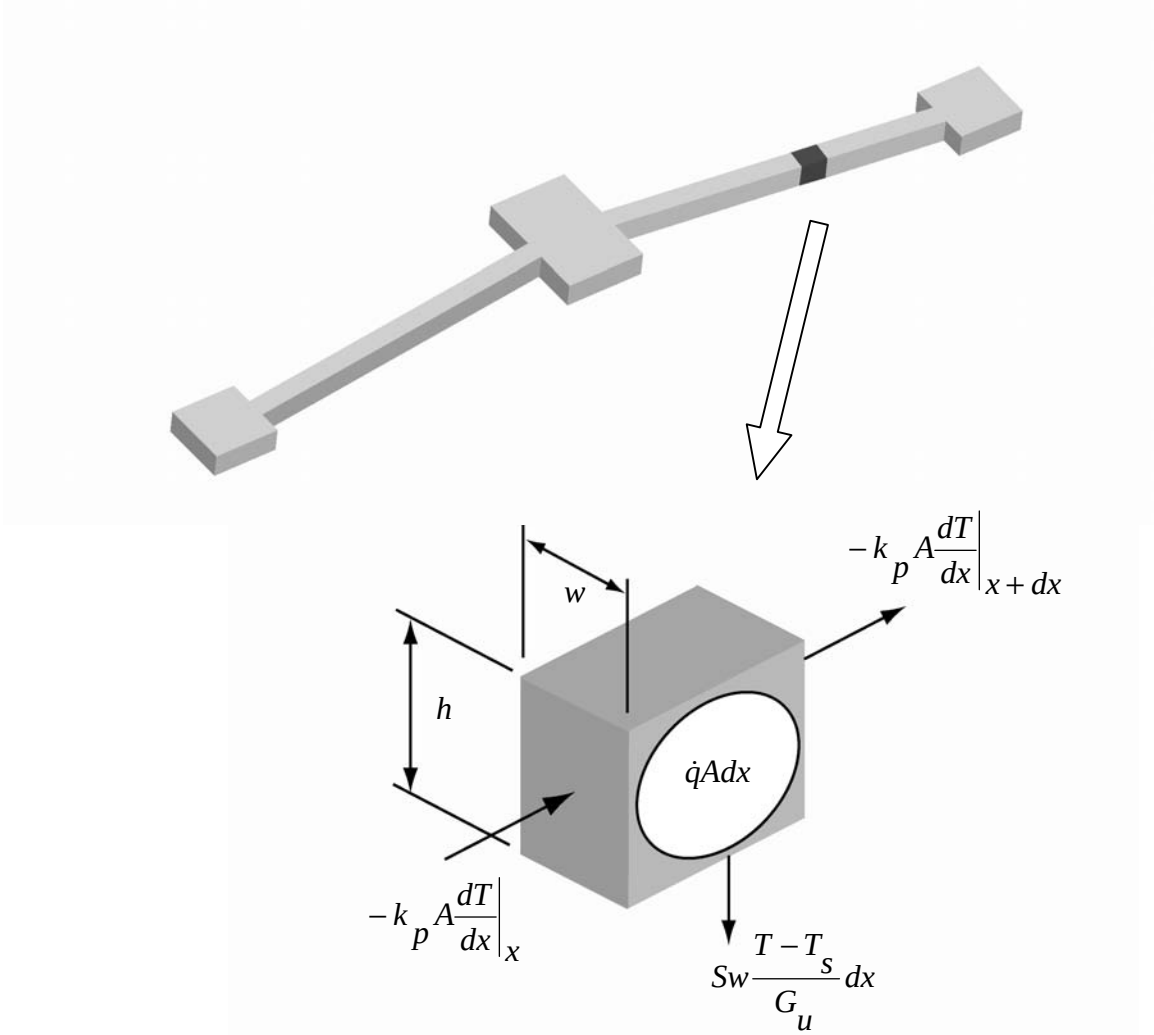

Figure 3.4 – Differential element for thermal analysis

rate of energy per unit volume generated within the element found from the current density *J* and the resistivity $\rho(T)$. It is expressed as

$$\dot{q} = J^2 \rho(T). \tag{3.2}$$

Equation 2.2 is used to describe the resistivity with temperature. It is restated here for convenience:

$$\rho(T) = \rho_0 [1 + \xi(T - T_s)] \tag{3.3}$$

For a beam-shape microbridge the shape factor, *S*, can be expressed as [36]

$$S = \frac{h}{w}\left(\frac{2h_{air}}{h} + 1\right) + 1 \tag{3.4}$$

where h is the height of the element, w is the width, and h_{air} is the height of the air gap between the leg and the substrate. From Figure 3.3 it is evident that the heat path to the substrate is through the air and an electrically insulating layer of silicon nitride into a silicon substrate. These layers act as three thermal paths in series, allowing G_u to be defined as

$$G_u = \frac{h_{air}}{k_{air}} + \frac{h_n}{k_n} + \frac{h_s}{k_s} \tag{3.5}$$

where h_n is the height of the Si_3Ni_4 layer, h_s is a representative height for the substrate, and k_{air}, k_n, and k_s are the thermal conductivities for the respective layers.

Dividing Equation 3.1 by A and k_p and taking the limit as $dx \rightarrow 0$ allows the governing equation for heat transfer to be written as

$$\frac{d^2T}{dx^2} + \frac{\dot{q}}{k_p} - S\frac{(T - T_s)}{k_p G_u h} = 0 \tag{3.6}$$

Performing a change of variables with Equation 3.6 and utilizing Equations 3.2 and 3.3 as substitutions produces

$$\frac{d^2\theta(x)}{dx^2} - m^2\theta(x) = 0 \tag{3.7}$$

where the following variables have been added:

$$m^2 = \frac{S}{k_p G_u h} - \frac{J^2 \rho_0 \xi}{k_p}$$

$$\theta(x) = T(x) - T_s - \frac{J^2 \rho_0}{k_p m^2}$$

The solution to the second-order differential expression of Equation 3.7 is

$$T(x) = T_s + \frac{J^2 \rho_0}{k_p m^2} + c_1 e^{mx} + c_2 e^{-mx} \tag{3.8}$$

Equation 3.8 describes the temperature distribution for any single leg-pair suspended in air and undergoing ohmic heating from an applied current. With three segments in the fundamental beam (left leg - 1, shuttle - 2, and right leg – 3), there exist three solutions of Equation 3.8, each with two constants of integration. Using boundary conditions that require the continuity of both temperature and the rate of heat conduction across the junction points of the slender leg and shuttle, linear algebra can be used to solve the resulting equations for the constants of integration. The boundary conditions can be expressed as

$$T_1(x)\big|_0 = T_3(x)\big|_{2L+Lc} = T_s \tag{3.9}$$

$$T_1(x)\big|_L = T_2(x)\big|_L \tag{3.10}$$

$$T_2(x)\big|_{L+Lc} = T_3(x)\big|_{L+Lc} \tag{3.11}$$

$$w \frac{dT_1(x)}{dx}\bigg|_L = w_c \frac{dT_2(x)}{dx}\bigg|_L \tag{3.12}$$

$$w_c \frac{dT_2(x)}{dx}\bigg|_{L+Lc} = w \frac{dT_3(x)}{dx}\bigg|_{L+Lc} \tag{3.13}$$

where the parameters L, L_c, w, and w_c are defined in Figure 3.2. This completes the setup of the analytical model. While concise in its formulation, it is limited in several ways. First, to make the differential equation represented by Equation 3.7 tractable, thermal

conductivity values of polysilicon and air are assumed to be constant and independent of temperature. A numerical approach has the ability to include the full temperature dependence of all thermal parameters. Second, Equation 3.9 imposes a set of "hard" boundary conditions that are required for a closed-form analytical solution. This boundary condition fixes the temperature at the beam-ends. For very short microbridges (40 μm in length) this assumption has been shown to be invalid [11]. A numerical simulation has the capacity to easily impose other boundary conditions. Third, while radiation can be assumed to be negligible at low temperatures [37,41], for the high temperatures and vacuum environments considered for the TIM, it can have an effect. A numerical approach can remedy this issue by including the effects of radiation in the model. Lastly, the dynamic response cannot be simulated with the steady-state analytical solution. To study the energy consumption and the actuator response time during a transient, a numerical study is helpful.

3.2.2 Finite-difference Model

To set up the finite-difference model, the device in Figure 3.3 was divided into discrete volume elements. By applying an energy balance to a control volume around each element, a state equation is formulated for each. When solved, the set of equations for all elements produces the nodal temperatures throughout the body. Based on an energy balance, the following state equation is obtained for the i^{th} element

$$q_i + q_{cond} + q_{rad} + q_{cond,i-1} + q_{cond,i+1} = q_{st}\,, \tag{3.14}$$

where q_i is the rate of energy generated in element i by ohmic heating, q_{cond} models conduction to the substrate, and q_{rad} models radiation to the surroundings. The conduction to element i from adjoining elements is modeled by the $q_{cond,i-1}$ and $q_{cond,i+1}$ terms. The net rate of change of the internal energy storage within the element is modeled by q_{st}. Because the contribution of free convection has been found to be small, it is not included in the energy balance [36,37].

Each of these energy terms can be determined from straightforward physical relationships. Ohmic heating can be calculated from the input current and material resistivity, $\rho(T)$, as

$$q_i = J^2 \rho(T) \Delta V_i \tag{3.15}$$

where J is again the current density input to the system and ΔV_i is the element volume. Conduction to the substrate is modeled by the expression

$$q_{cond} = \frac{SA_u}{G_u}[T_s - T_i(k)] \tag{3.16}$$

where T_s is the temperature of the substrate (assumed constant) and $T_i(k)$ is the temperature of the i^{th} node at the k^{th} time increment. A_u represents the area of the element's surface that faces the substrate, S is the same shape factor defined in Equation 3.4, and G_u is defined in Equation 3.5. Over the bond pads, the layer representing the air gap is removed and h_{air} is set to zero in Equation 3.5.

Radiation to the surroundings is negligible at low temperatures. However, for the high temperatures expected in vacuum environments its effect is included. The energy radiated to the surroundings can be expressed as

$$q_{rad} = \varepsilon \sigma A_s [T_{sur}^4 - T_i^4(k)] \tag{3.17}$$

where A_s is the area of the exposed surface of the element and T_{sur} is the surrounding ambient temperature.

Conduction of heat between elements, such as elements $i-1$ and i, is modeled by the expression

$$q_{cond,i-1} = \frac{k_p A_x}{\Delta x}\left[T_{i-1}(k) - T_i(k)\right] \tag{3.18}$$

where A_x is the cross-sectional area of the element, Δx is the length of the element in the direction of heat transfer and k_p is the thermal conductivity of polysilicon. Finally, storage of thermal energy within each element is calculated as

$$q_{st} = \frac{\rho_d c \Delta V}{\Delta t}\left[T_i(k+1) - T_i(k)\right] \tag{3.19}$$

where ρ_d and c are the density and specific heat of polysilicon and Δt is the time increment.

By substituting Equations 3.15 through 3.19 into Equation 3.14, an explicit expression for the temperature at subsequent time k+1 $\left(T_i(k+1)\right)$ in terms of temperatures at the current time k $\left(T_i(k), T_{i-1}(k), T_{i+1}(k)\right)$, the input $\left(J(k)\right)$, and the boundary conditions (T_{sur} and T_s) can be formed. The resulting expression can be written as

$$\begin{aligned} T_i(k+1) = \frac{\Delta t}{\rho c \Delta V}\Bigg[& J^2 \rho_r(T)\Delta V_i + \frac{SA_u}{G_u}\left(T_{sub} - T_i(k)\right) + \varepsilon\sigma A_s\left(T_{sur}^4 - T_i^4(k)\right) \\ & + \frac{k_p A_x}{\Delta x}\left(T_{i-1}(k) - T_i(k)\right) + \frac{k_p A_x}{\Delta x}\left(T_{i+1}(k) - T_i(k)\right)\Bigg] \end{aligned} \tag{3.20}$$

By solving the system of difference equations from all of the elements over a series of time increments, a profile of temperatures throughout the device as a function of time can be produced.

When discretizing the leg-pair, element sizes less than 10 μm did not significantly improve the spatial resolution on the temperature profile across the TIM. Therefore, a length of 10 μm is used for the size of each discrete element. However, because the

explicit finite-difference method has requirements for stability, the choice of the element size controls the time step needed to guarantee convergence. Stability ensures that solutions at successive time increments will satisfy the second law of thermodynamics and that $T_i(k)$ will not become negative. Based on well-established criterion for stability [14] and an element length of 10 μm, a constant time step of 1×10^{-6} seconds (1 μs) was used. Appendix A contains the code used to develop the finite-difference model and simulate the TIM. It is written for MATLAB [21] and contains detailed comments. Chapter 4 discusses the results from the finite-difference electrothermal model in depth.

In order to include the material properties that change with temperature, the i^{th} nodal temperature from the previous time increment $(T_i(k-1))$ is used to determine the value for the property at the k^{th} time increment. With small time steps and temperature changes, this results in an accurate accounting of the temperature dependencies. The material properties that change with temperature include: thermal conductivity for polysilicon (k_p), thermal conductivity for air (k_{air}), and the electrical resistivity for polysilicon (ρ). Expressions for each of these material properties as a function of temperature were discussed in Chapter 2.

3.3 THERMOMECHANICAL MODELS

The thermomechanical models in this thesis rely on temperature profile results from the electrothermal model, presented in Section 3.2, to calculate deflection and force. Deflection was calculated in two ways: (1) a pseudo-rigid-body model approximation that was derived from compliant mechanism theory for fixed-guided beams, and (2) a commercial finite-element program capable of nonlinear analysis (ANSYS) was also employed. When the pseudo-rigid-body model is coupled to the finite-difference approach, transient deflections can be modeled.

Both methods calculate thermal expansion in each of the discretized elements (once the temperature distribution along the length of the actuator is known) from the equation

$$\begin{aligned}\Delta L_i &= \int_{L_i} \alpha\left(T_i(x)\right)\cdot\left[T_i(x) - T_s\right]dx \\ &\approx \alpha\left(\overline{T_i}\right)L_i\left(\overline{T_i} - T_s\right)\end{aligned} \tag{3.21}$$

where $\overline{T_i}$ is simply the i^{th} nodal temperature from the discretized thermal model solution. The total growth in a single leg (ΔL) of a TIM is the sum of all the discrete ΔL_i that occur in the leg. The expression for $\alpha(T)$ was given in Equation 2.8 and is repeated here for convenience:

$$\alpha(T) = \left(3.725\left\{1 - \exp\left(-5.88\times10^{-3}\left(T - 124\right)\right)\right\} + 5.548\times10^{-4}T\right)\times10^{-6} \tag{3.22}$$

The growth that happens in a single leg of the fundamental beam (only one side of a leg-pair) is sufficient to determine the actuator's motion. The other side of a single leg-pair provides the symmetry needed for a geometric constraint (see Section 2.1) and provides stability and support to the shuttle. The growth in a single beam as a result of ohmic heating and thermal expansion can be expressed as

$$\Delta L = \sum_i \Delta L_i \tag{3.23}$$

3.3.1 Pseudo-rigid-body Approximation

The pseudo-rigid-body model (PRBM) allows an engineer to develop relatively simple and accurate approximations to large deflections in compliant members. The validity of this modeling technique has been established [16,17,50]. The model uses rigid links and torsional springs to represent force-deflection characteristics in compliant mechanisms. Because the rigid-link systems can be analyzed with traditional mechanism theory, the

model connects commonplace mechanism analysis tools and geometries with compliant mechanism theory. With respect to a TIM, this section outlines how the PRBM can be adapted to model the displacement of the shuttle as a result of thermal expansion in the legs.

Early in the development of the PRBM it was realized that the deflection path of a cantilever beam with arbitrary end forces is similar to an arc centered at one-sixth the beam's length from the fixed end and circumscribing a deflection path of five-sixths radius [4]. Howell and Midha modeled this deflection using two rigid links joined by a pivot [17]. A nonlinear spring placed at the pivot models the resistance to deflection. The pivot is called the "characteristic pivot" and the length of the pseudo-rigid-body link is defined by the product γl, called the "characteristic radius", where γ is the characteristic radius factor. The value for γ is different for changing end-loading conditions. In Figure 3.5, variable end-loading conditions are designated *P* and *Pn*, where *P* is an arbitrary vertical load and the variable *n* represents the ratio of the axial load to the transverse load. In the case of the TIM, the loading is expected to have a large value of *n* due to the force resulting from thermal expansion.

In this thesis, a constant value for γ is used to approximate the TIM's deflection for simplicity. For all simulations, a value of 0.82 is selected. This choice is in agreement with the equations presented by Howell and Midha [17] for loading conditions with a large component for *n*. An equation for γ corresponding to the expected values of *n* that occur with a TIM is

$$\gamma = 0.841655 - 0.0067807n + 0.000438n^2; \quad 0.5 < n < 10.0 \qquad (3.24)$$

In Equation 3.24, when *n* is equal to 10.0, γ equals 0.818. The value of 0.82 is also between the values of $\gamma = 0.8517$ for a pure vertical end load ($n = 0$) and pure end moment loading of $\gamma = 0.74$ as expected since the actual load is a combination of these two conditions [50].

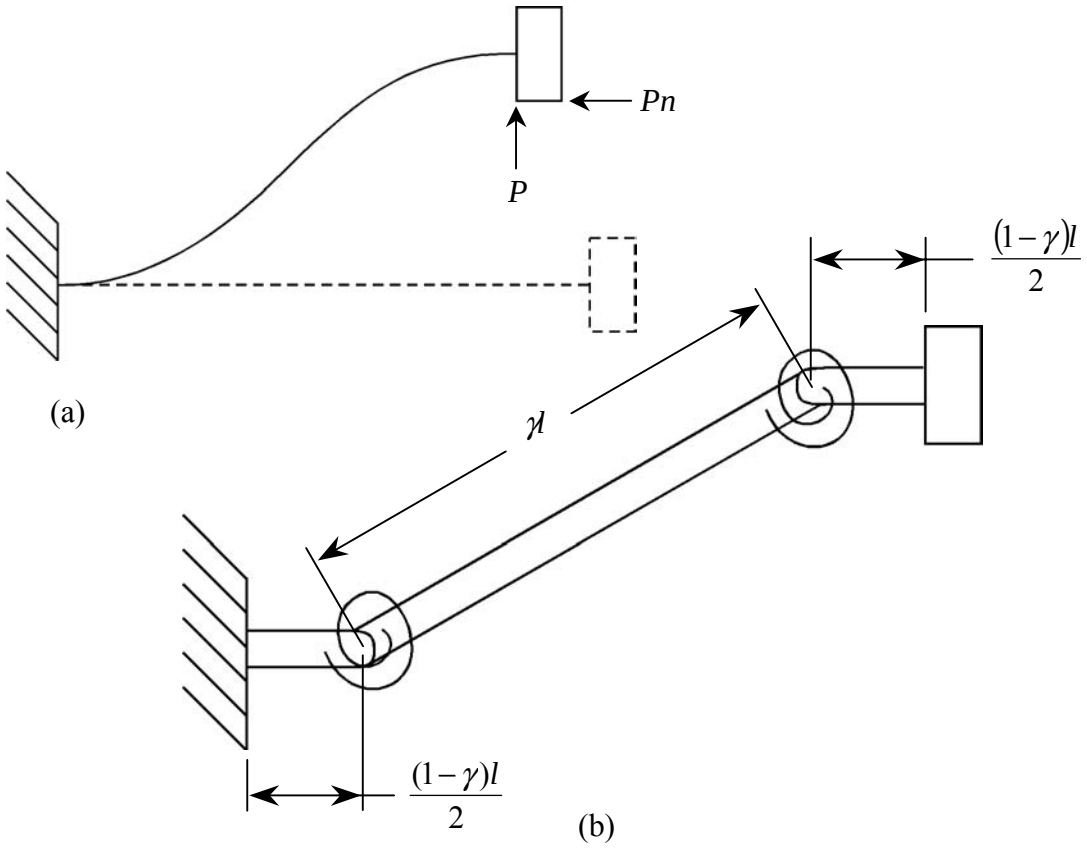

Figure 3.5 – Fixed-guided compliant segment (a) flexible beam with constant end angle (b) pseudo-rigid-body model

Within the scope of the PRBM, there are many standard design configurations to help model compliant members with rigid-body kinematics. It is not within the objectives of this thesis to review all of the standard models; however, one is appropriate. For a complete study refer to Howell [15]. The model represented here is referred to as a fixed-guided segment. A fixed-guided segment is one where a beam is fixed at one end, and the other end goes through a deflection such that the angular deflection at the end remains constant. The beam shape is antisymmetric about the center. A representation of this segment and its motion is illustrated in Figure 3.5. The standard segment for a single fixed-guided beam has the ability to represent the motion of the TIM that results from thermal expansion after pseudo-rigid-body approximations are made. The legs are fixed to both the bond pads and shuttle. The shuttle follows a guided path during its motion as a result of the symmetry in the device.

In order to develop the equations from PRBM approximations that account for the displacement of the shuttle, a few illustrations are discussed. These progressive illustrations create a model for the displacement of a TIM. The first illustration, seen in Figure 3.6a, demonstrates the expected motion for a compliant fixed-guided segment under an arbitrary load *F*. In a TIM, the load *F* is the force that results after ohmic heating and thermal expansion. A TIM, however, behaves differently then the cantilevered fixed-guided segment in Figure 3.6a; a TIM will move as shown in Figure 3.6b. The symmetry provided by a single leg-pair is what dictates the path of this motion after thermal expansion occurs. The line of symmetry creates a boundary condition and vertical motion is constrained to be along this line.

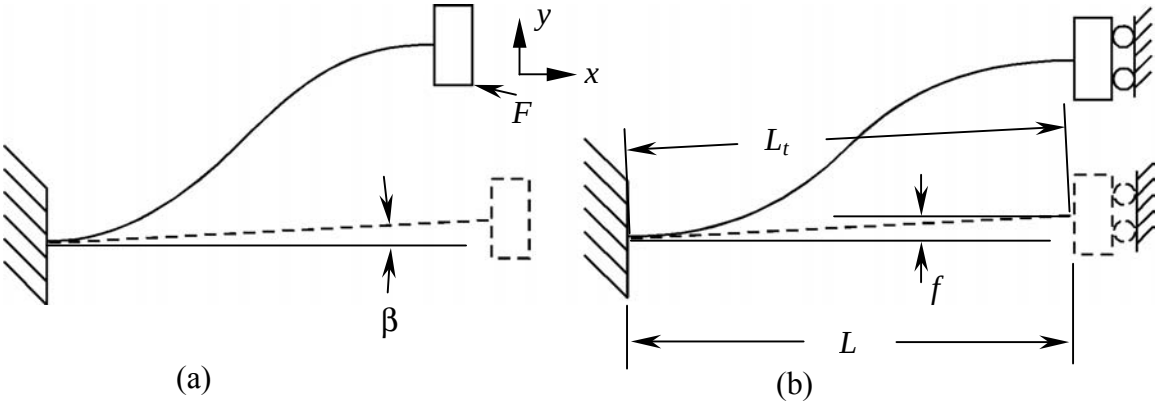

Figure 3.6 – (a) Usual fixed-guided motion, and (b) fixed-guided motion with thermal expansion.

In Figure 3.6, L_t is the total length of the beam as defined by the offset *f*, and the horizontal length *L*. The inclination angle β of the leg is equal to

$$\beta = \tan^{-1}\left(\frac{f}{L}\right) \tag{3.25}$$

As discussed previously, the offset *f* causes the TIM to move in the desired direction.

A coordinate transformation is helpful during development of the model for displacement. The transformation is simply a clockwise rotation of the leg through the

angle β. This rotation makes the PRBM approximations easier. However, the line of symmetry is no longer vertical in the new coordinate frame. With respect to the new coordinates, shown in Figure 3.7 as $\{x', y'\}$, the line of symmetry is

$$y' = \frac{L}{f}x' - \frac{LL_t}{f} \tag{3.26}$$

where the origin is the fixed end that represents the location where the leg connects to the bond pad. Equation 3.26 is not a function of the thermal expansion but rather is dependent only on the TIM's initial fabrication lengths. Therefore, the symmetry line is constrained and will not move when the leg expands. In Figure 3.7a, the actual displacement of the TIM is defined as y_1. To help find this displacement, PRBM approximations to the leg are used as shown in Figure 3.7b. The PRBM includes the growth in a leg from thermal expansion and calculates the new characteristic radius. The variable L_n is the new total length of the beam after thermal expansion and is equal to $L_n = L_t + \Delta L$.

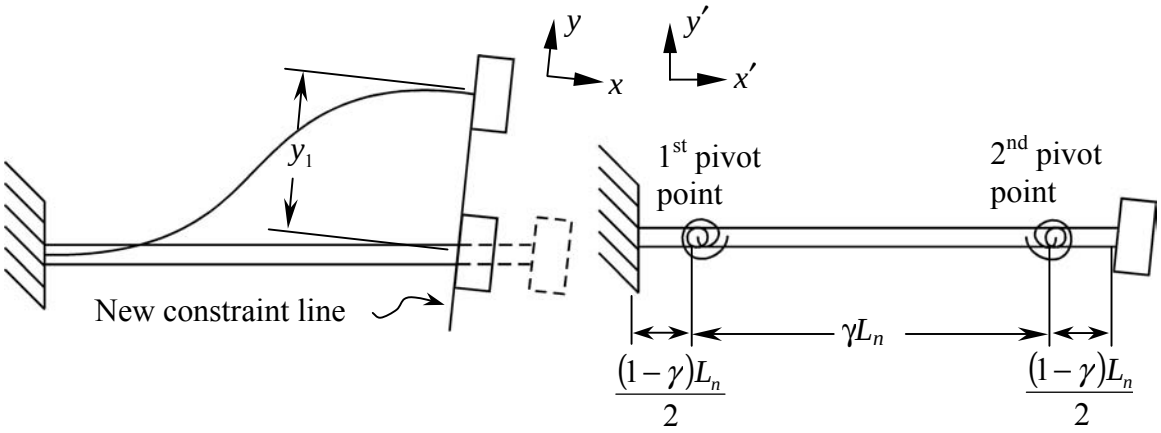

Figure 3.7 – (a) Coordinate transformation of a TIM leg, and (b) the PRBM approximation that accounts for thermal expansion

Because the PRBM is being used to predict the vertical displacement y_1' in the new coordinate frame, only the arc circumscribed by the new characteristic radius γL_n

contributes to this distance. When the arc meets the constraint line represented by Equation 3.26, the displacement from thermal expansion is calculated. Equation 3.27 is an expression for the arc from PRBM approximations:

$$y' = \sqrt{(L_n\gamma)^2 - (x' - L_n(1-\gamma))^2} \tag{3.27}$$

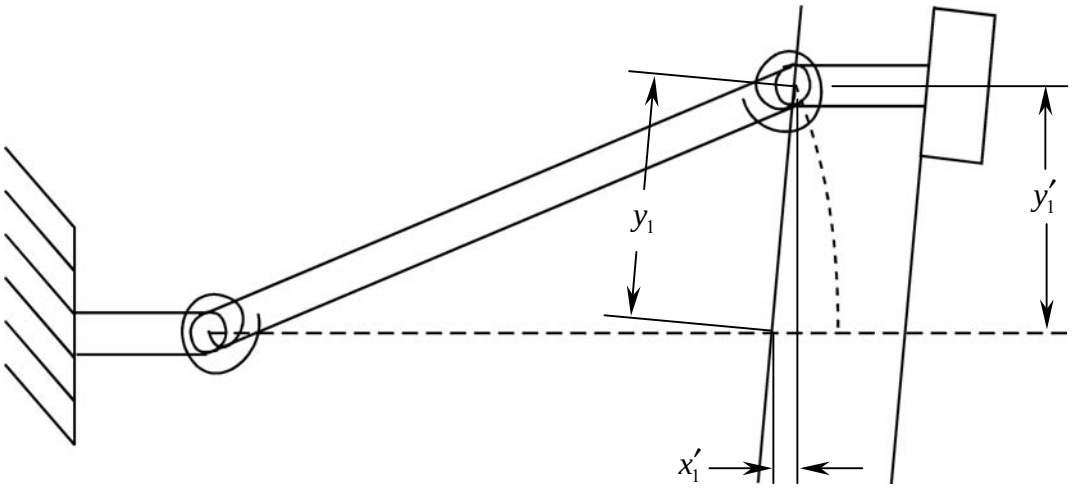

Figure 3.8 – The arc circumscribed by PRMB approximations and new characteristic radius used to find displacement of shuttle.

This arc is centered at a distance $(1-\gamma)L_n$ in the positive x' direction to account for the ends that remain straight during the motion of a fixed-guided segment. When Equation 3.26 is substituted into Equation 3.27 the result is a quadratic equation in y'. The positive root of the quadratic equation is the displacement of the TIM in the correct direction. The final result of the displacement y_1' after all substitutions is

$$y_1' = \frac{-2cd + \sqrt{4c^2d^2 - 4(1+c^2)((d^2 - a^2)}}{2+2c^2} \tag{3.28}$$

where

$$a = L_n\gamma$$
$$b = L_n(1-\gamma)$$
$$c = \frac{f}{L}$$
$$d = L_t - b$$

The complete expression for y_1' in terms of the original full length of one leg L_t and the growth from thermal expansion ΔL can be expressed as

$$y_1' = \frac{fL\Delta L - LL_t f\gamma - fL\Delta L\gamma + L\sqrt{f^2\left(L_t{}^2\gamma^2 + 2L_t\gamma^2\Delta L + \Delta L^2\gamma^2\right) + L^2\left(2\Delta LL_t\gamma - \Delta L^2 + 2\Delta L^2\gamma\right)}}{L^2 + f^2} \quad (3.29)$$

The actual displacement of the shuttle after thermal expansion in the leg can then be found in the original coordinate frame from the expression

$$y_1 = \frac{y_1'}{\cos\beta} \quad (3.30)$$

Predictions of the shuttle displacement with Equation 3.30 match very well with models solved using FEA.

3.3.2 Finite-element Approximation

Commercial finite-element software is also used in this thesis. ANSYS [18] was selected because of its ability to handle nonlinear deflections. While possible to obtain the same information as both the electrothermal finite-difference and pseudo-rigid-body models with finite-element analysis (FEA), the capabilities for the study of both the electrothermal energy domain and the thermoelastic energy domain with a single beam element are currently limited in this software package. The following explains two methods for performing both the electrothermal model and thermomechanical model within ANSYS. The names of the elements are particular to the ANSYS software.

The first method, called the sequential method, applies the solution from the first domain (electrothermal) as body force loads onto the second domain (thermoelastic). In ANSYS, LINK68 and BEAM3 can be used for this purpose. LINK68 solves for the nodal temperatures due to ohmic heating. BEAM3 takes the temperatures as loads and finds the displacement that results from thermal expansion.

A deficiency in this method is that beam elements are not capable of supporting surface loading such as heat flux due to conduction to the substrate. This makes modeling the TIM in air difficult to do with beam elements alone. To remedy this situation, ANSYS provides SOLID5, a three-dimensional (3D) solid element with the appropriate degrees of freedom to handle coupled-field analysis. This is the second approach and is referred to as the direct method. However, in version 5.5, this element does not yet support nonlinear analysis in the mechanical domain. Enhancements to future versions of ANSYS are expected to more fully support the multiphysics demands relative to MEMS [19]. It is still possible to use elements other than LINK68 and BEAM3 and apply the solution from the first element as body force loads to the second element. For example, three-dimensional elements that would support the sequential method for the TIM in air are SOLID69 and SOLID45. However, in order to study the transient behavior with the same time scale as the finite-difference model (1×10^{-6} seconds) the sequential method is unwieldy.

One benefit of FEA is the capability to predict the maximum force available from the TIM under steady-state temperature profiles. In this thesis, BEAM3 is used to mesh a model of the fundamental beam in ANSYS. To find the maximum force available through the TIM's range of motion, the steady-state nodal temperatures from the finite-difference solution are applied as body force loads to nodes from the mesh. The maximum force at a specific distance is assumed to be the reaction force on the shuttle as shown in Figure 3.9. The total force from a TIM scales linearly with the number of single leg-pairs. The results of these simulations are given in Chapter 4. Appendix B is an example batch file for ANSYS with detailed comments.

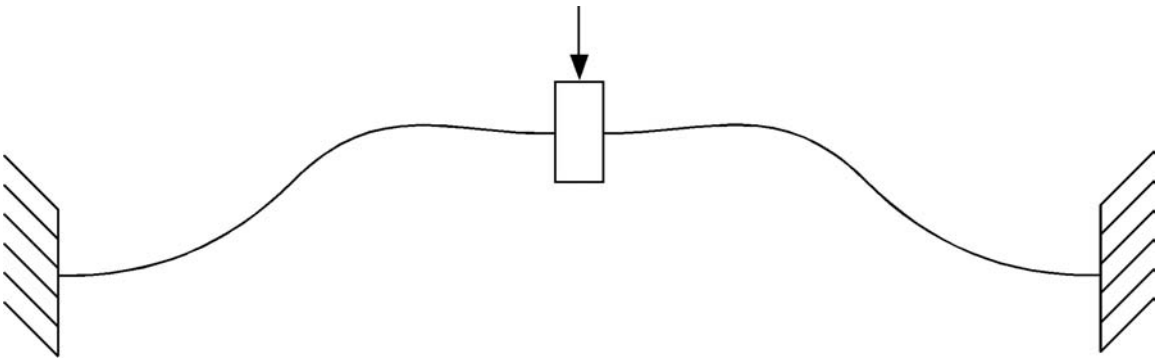

Figure 3.9 – Illustration of the maximum force tests performed with FEA.

3.4 MODELING THE FIRST MODAL FREQUENCY

The natural frequency of any actuator is an important characteristic. For high-bandwidth response, it is often desirable to have the first natural frequency of the actuator be much faster than a commanding input signal. At other times, it may be desirable to use resonance to amplify motion. In this section, an expression is developed to predict a TIM's first modal frequency. When this frequency is compared to the thermal transient response for temperature decay in a TIM, it is shown that thermally driving an uncoupled TIM to resonate is not possible.

It is noted that uncontrolled thermal systems cannot have resonance or overshoot by themselves because there is no thermal inductive element. In other words, there is no inductive element that can store kinetic energy from which resonance with the thermal capacitance (mass times specific heat) or potential energy can occur. The hope of driving a TIM to resonate lies in attempting to match the thermal response with the mechanical-elastic response of the actuator. In the mechanical domain, resonance can occur for systems having both compliance and inertia. The analysis will show that electrical drive signals will not cause mechanical resonance.

In 1997, Lyon et al. used the pseudo-rigid-body model to derive dynamic equations for compliant parallel-guiding mechanisms. Figure 3.10 illustrates the parallel-guiding mechanism studied that behaves similar to the TIM. An actual TIM has two of these devices (or two fundamental beams) working in parallel because of symmetry. The PRBM for the device is also shown. Using Lagrange's method applied to the PRBM for each of five different parallel-guiding mechanism configurations, test results found the modeling error was less than nine percent when predicting the natural frequency [39]. It is also interesting to note that the difference between classical beam theory and PRBM predictions for the mechanism most like the TIM were within 1.9 percent.

The natural frequency obtained using the PRBM for any configuration of a compliant parallel guiding mechanism is given by [39]

$$\varpi_n = \sqrt{\frac{K_1 + K_2 + K_3 + K_4}{\left(M_3 + \frac{M_2 + M_4}{4}\right) r_2^2 + I_2 + I_4}} \text{ (rad/sec)} \qquad (3.31)$$

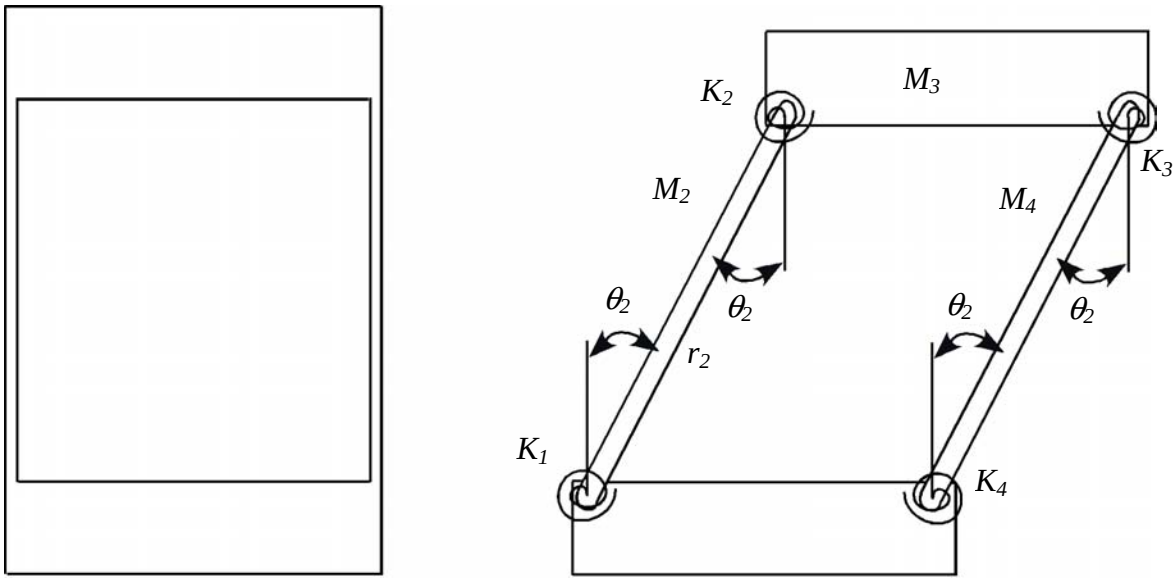

Figure 3.10 – Compliant parallel-guiding mechanism and its PRBM.

where M_i is the mass of the link i, I_i is the mass moment of inertia of link i, and K_i is the nonlinear spring constant as shown in Figure 3.10. The length r_2 is the characteristic radius defined by $r_2 = \gamma l$. Because the sizes of the TIM's legs are equal, the spring constants are all the same. For a fixed-guided segment, this allows

$$K = K_1 = K_2 = K_3 = K_4 = 2\gamma K_\theta \frac{EI}{l} \tag{3.32}$$

where l is the length of the compliant leg, I is the area moment of inertia for the leg, E is Young's modulus of elasticity (assumed 160 GPa), and K_θ is the stiffness coefficient [15] defined here to be equal to 2.61. The characteristic radius factor, γ, will remain equal to 0.82, as discussed in 3.3.1.

To modify Equation 3.31 so that it can represent a TIM, a coefficient for the number of leg pairs, n_l, is multiplied to the sum of spring constants under the square root. Because the spring constants are all equal (see Equation 3.32) and each leg moves the same distance upon thermal expansion (like springs in parallel), the coefficient n_l simply accounts for all of the springs added with each new leg pair. Also, for a TIM the mass of the slender legs is very small in comparison to the mass of the shuttle, and is assumed negligible (M_2 and $M_4 = 0$). Then, if Equation 3.31 is adjusted to give the natural frequency in Hertz (Hz) the simplified result is

$$f_n = \frac{\gamma}{\pi r_2}\sqrt{\frac{2n_l K_\theta EI}{M_3 r_2}} \text{ (Hz)} \tag{3.33}$$

Tests with the TIM are commonly designed with eight or more legs. On the first working prototypes, the shuttle dimensions were 300 μm by 50 μm by 3.5 μm. Since polysilicon has a density of 2330 kg/m^3 this gives a shuttle mass of 1.223×10^{-7} grams. For the parameters defined above, a TIM with eight leg-pairs has an undamped natural frequency of 58.3 kHz. As the modeling of Chapter 4 will show, the bandwidth of the

electrothermal actuation is approximately 200 Hz. This is almost 300 times slower than the resonant frequency of the mechanical portion of the TIM. Therefore, excitation of mechanical resonance is not possible through thermal expansion. Simulation and validation of the models in this chapter (including predictions of the thermal time constant of a TIM) are the focus of Chapter 4.

Chapter 4

MODEL VALIDATION

This chapter uses the models developed in Chapter 3 to provide simulations of a TIM. Results from the simulations are compared to experimental data gathered from tests with several microactuators. Experiments confirm that the models can be used to obtain information on the TIM's temperatures, power requirements, energy consumption, transient response, displacement, and force. The models are then used to develop suggestions for how the TIM might be used in novel ways to increase efficiency with specific applications. Section 4.1 describes the experimental setup used to measure the TIM's deflection, force, and response time. Section 4.2 discusses the finite-difference solution and selection of material property relationships that best match experimental tests. In Section 4.3, the results from dynamic simulations are examined and Section 4.4 expands the initial model to look at short-duration high-current pulses with specific applications. Finally, Section 4.5 compares predictions of the output force from a TIM to experimental results.

4.1 EXPERIMENTAL SETUP

This section discusses the experimental setups used to obtain data from a TIM for deflection, force, and transient response. Experimental tests to measure maximum force and the transient response were performed in air while deflection tests are performed in both air and vacuum.

4.1.1 Displacement Measurements

Tests on the TIM took place in air or under the high vacuum ($1\times10^{-5}\,torr$) required by the scanning-electron microscope (SEM) upon release of the devices. Testing in open-air ambients occurred with microprobes while viewing the TIM under an optical microscope. The microprobes were placed on the TIM's bond pads and connected to a HP 4145a Semiconductor Parameter Analyzer. The 4145a provided a constant current input to the TIM and measured the resulting voltage. For tests in the SEM's vacuum chamber, 0.0015-inch diameter aluminum wire was bonded to the TIM's pads and attached to a printed circuit board that was fabricated with copper traces on one side. The printed circuit board was mounted in the SEM vacuum chamber and allowed a maximum of 19 connections to be made between the MUMPs die and the outside of the vacuum chamber. Electrical connections in and out of the vacuum chamber are made possible by a vacuum tight feed-through tube attached to the chamber. The feed-through tube connects to a panel with space for the corresponding 19 connections by means of standard BNC fittings. The 4145a provided constant current inputs for both in-air tests and for tests in a vacuum.

Tests in both air and vacuum were used to validate the finite-difference model by indirect means. Because of the difficulty in obtaining a direct temperature measurement from the thin (3 μm) legs of the TIM, the final displacement of the shuttle was recorded and compared with the model predictions. The difficulty in obtaining temperature measurements of a TIM leg is a consequence of the device's feature size. One common approach is to use an infrared microscope. By measuring the self-emitted radiance of an object and correcting for emissivity of the surface, infrared temperature measurements can be obtained. However, as an example, the current state-of-the-art EDO Barnes infrared microscope, known as the Infrascope, has a maximum feature resolution size of 5 μm [20,41]. This is too large for the TIM's feature size. Therefore, the final displacement of the TIM's shuttle from ohmic heating and thermal expansion was the primary method used to verify the accuracy of the models.

A second validation approach for the finite-difference model involved photographing the TIM at specific current inputs and looking for two things: the onset and location of visible radiation or the beginning of a small glow, and the charring or destruction of the legs at the melting temperature. In the vacuum chamber of the SEM, visible radiation is not easily detectible on the microscope's monitor. However, the method of examining the location of visible radiation is a useful guide for in-air tests.

All tests for both air and vacuum were recorded with videotape and data for displacement was extracted with motion analysis software (OPTIMAS) [47]. The software traces a

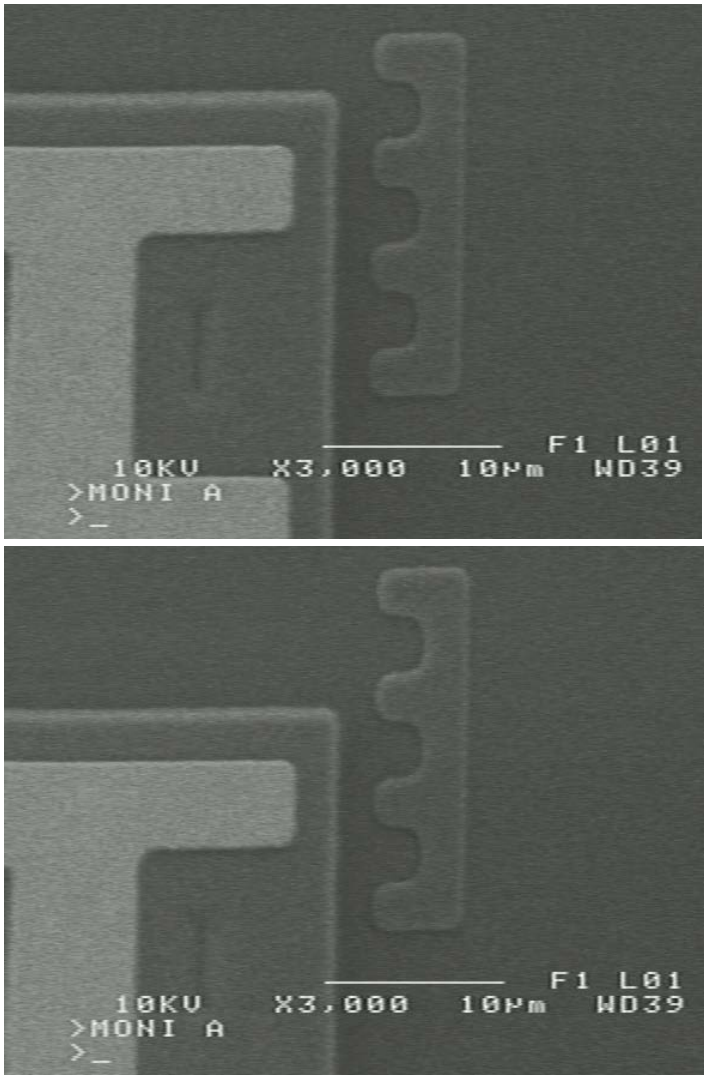

Figure 4.1 – Successive frames from videotape taken in vacuum: (Top) starting location of TIM and (Bottom) final displaced position.

point between frames and calculates the resulting deflections. The traced point is chosen by selecting a pixel in one frame, and then selecting the pixel again after displacement occurs. Therefore, the error from tracing a single point changes with the size of the pixel. The size of a pixel is determined by the magnification on the microscope. Cragun found the pixel width at 25x magnification to be 0.797 μm and at 50x to be 0.389 μm for the test setup used [10]. Since the in-air tests to measure displacement were all recorded at 100x and vacuum data with a SEM were recorded beyond 1000x, the pixel error is small. Figure 4.1 shows individual frames from videotape taken from the vacuum experiments. The scale on the right is for reference only and motion analysis software calculated the final displacement.

4.1.2 Force Measurements

To measure the maximum force available, micromachined force gauges have been developed [57]. These force gauges offer an improvement over previous methods that rely on the deflection of a single cantilever beam to measure the force from thermal microactuators [49]. The largest improvement from these gauges results from their ability to extract a range of force measurements as opposed to the single force measurement from the deflection of one cantilever beam. This feature allows the force displacement characteristics for a single TIM to be approximated throughout its range of motion. The operation of these new micromachined force gauges is discussed briefly below.

Figure 4.2 is a micrograph of a force gauge designed for MUMPs. The entire force gauge will slide in the direction of the vertical arrows on the side of Figure 4.2. A microprobe is used to manipulate the force gauge into contact with the TIM. The center beams deflect and the distance of the gap shown in Figure 4.2 will close. Changes in the distance of the gap *d* are measured and provide an estimate of the applied force. From the work of Wittwer et al. [57], an explicit equation for force in terms of *d* is given by

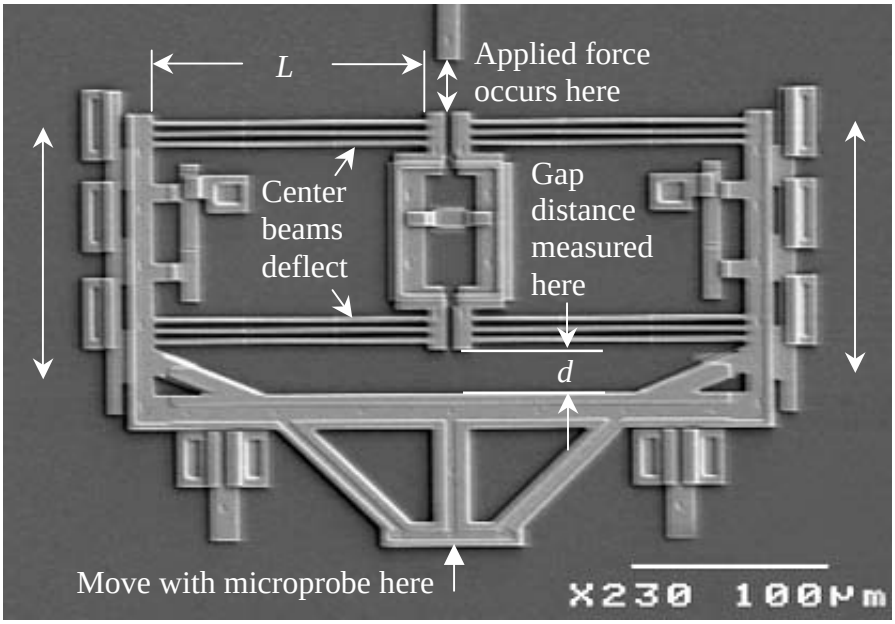

Figure 4.2 – Surface micromachined force gauge

$$F = \frac{N_p}{4N_s}\frac{Ewh^3 d}{l^3}\frac{1}{1+\varepsilon_p} \tag{4.1}$$

where

$$\varepsilon_p = 0.0040\left(\frac{\delta}{l}\right) - 1.0760\left(\frac{\delta}{l}\right)^2 + 0.1697\left(\frac{\delta}{l}\right)^3 - 0.3390\left(\frac{\delta}{l}\right)^4$$

and

$$\delta = \frac{d}{2N_s}$$

Because Equation 4.1 is adaptable to many configurations, N_p is the number of beams in parallel and N_s is the number of sets of parallel beams in series on each side of the gauge. In Figure 4.2, N_p equals six and N_s equals one. E is Young's modulus, w is the out-of-plane thickness of the beam, h is the in-plane width of the beam, and l is equal to the length of the beam L divided by two ($l = L/2$). The length L is shown in Figure 4.2. The correction equation ε_p is found by comparing linear equations for beam deflection

to the closed-form elliptic integral equations and curve-fitting ε_p to the error. For a complete derivation refer to Wittwer et al. [57].

4.1.3 Transient Measurements

The electrothermal finite-difference model presented in Chapter 3 is setup to solve explicitly for nodal temperatures. Examining the nodal temperatures at each time step allows the transient shape of the temperature distribution along a single leg-pair to be studied. This is important because the amount of energy consumed and power necessary to achieve an average temperature rise, along with the resulting displacement, can be recorded. When the energy consumption during transient heating and the steady-state power necessary to maintain a constant temperature profile is known, TIMs can be selected for complete microsystems that may have power constraints or limited energy to supply. This is certainly the case with recent micro autonomous system developments [31].

Previous experimental measurements of a TIM used a high-speed camera with a 1 kHz frame rate to record motion. In response to step inputs in current the TIM would reach its final deflection within two frames. In this thesis, contacts were placed so a connection could be measured after a TIM had traveled 3, 5, 7, 9, and 11 μm. Because the TIM used for the transient measurements is capable of steady-state displacement beyond the 11 μm contact, these tests provide five intermediate points to verify the transient location and speed of the actuator.

A two channel digital oscilloscope from Tektronix (TDS 340A) capable of a high sampling rate (500 MS/s) was used to record the input signal from the HP 4145a on channel one and record the voltage jump as the contacts closed on the second channel. The vertical cursors for each channel on the oscilloscope measured the time difference between the voltage rise on channel one with channel two. In this way, the time for a TIM to travel a known distance was measured and compared to simulations with the

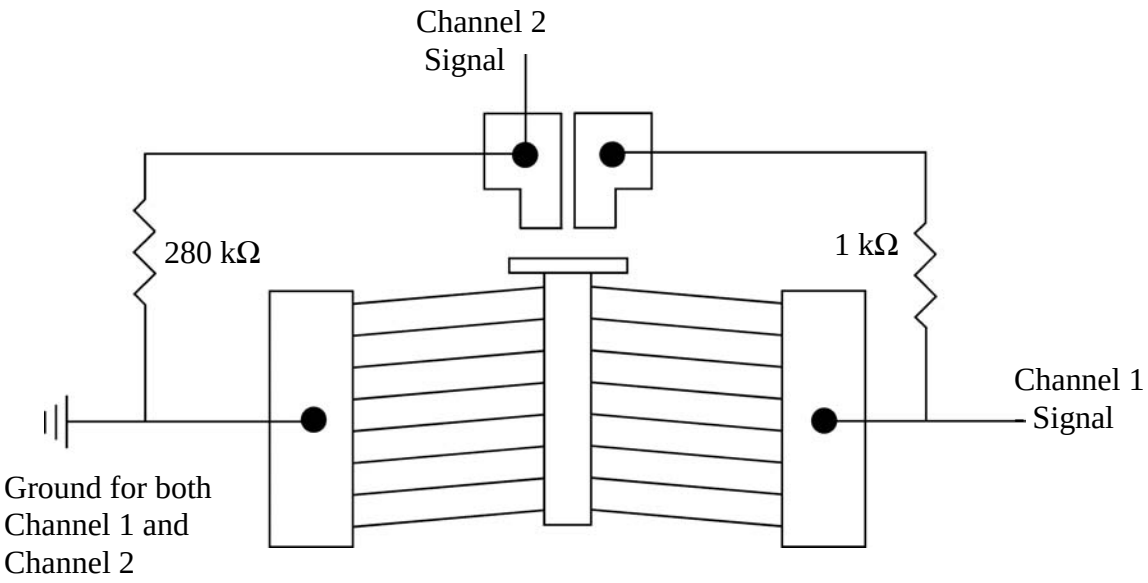

Figure 4.3 – Illustration of the setup used to measure the transient of a TIM.

model. Figure 4.3 is an illustration of the connections used to make the transient measurements.

4.2 ELECTROTHERMAL SIMULATIONS

Simulations were based on a typical TIM design having a leg length L of 250 μm and shuttle dimensions of 50 μm by 30 μm for L_c and w_c respectively. Laminate beams from MUMPs poly1 and poly2 are used to create beams 3 μm wide and 3.5 μm tall. The laminate beams have the advantage of being more stiff out-of-plane, or normal to the substrate, helping prevent out-of-plane buckling from an applied force. The boundary conditions applied to the TIM model assume that the temperatures below the anchored bond pads, T_{sub}, and the surrounding temperature T_{sur} remain constant at 20 C. For leg lengths of this size, this approximation is good; however, for legs with very short lengths, significant end heating at the bond pads will occur and should be accounted for [11]. End heating in the finite-difference model is simulated by creating bond pads that were 100 μm long by 30 μm wide at the ends of a single leg-pair. The pads are only heated by

axial conduction; the heat generation term from Equation 3.15 is not included for bond-pad elements. As mentioned in Chapter 3, the spatial resolution used is 10 μm. Therefore, each leg is divided into 25 elements of equal length.

As discussed in Chapter 2 and emphasized in Chapter 3, the material properties of a TIM are dependent on temperature. Using the finite-difference model, variations with temperature for these parameters can be included in a sequential manner and their relative importance examined. In this research, results are presented for three different cases. The first case assumes a constant k_p and constant k_{air} while allowing the effects from radiation to be included in the model. Therefore, the first case should approximate the analytical solution well since the effects of radiation are not large. The first case is referred to as the "state-invariant" model because of its similarities with the analytical solution and the use of physical parameters that are not dependent on temperature. The second case examined will use Equation 2.5 as a varying expression for k_{air} while k_p remains constant. This combination emphasizes the importance of including a k_{air} parameter that is dependent on temperature, and departs further from the analytical solution. Case two is referred to as the "constant-k_p" model. The last case includes the temperature dependent expression for k_p available from Manginell [41] (see Equation 2.1 on page 18). This expression varies over the range for which it was measured (293 K to 800 K) from 72 W/m/K to 32 W/m/K. Case three, referred to as the "state-dependent" model, also includes Equation 2.5 for a varying k_{air} parameter.

With polysilicon, the scattering mechanisms that lead to a temperature dependence of thermal conductivity include grain-size and dopant concentration, which depend on the deposition method. Smaller grain-sizes and higher dopant concentrations are expected to flatten the temperature-dependent curve for k_p [41]. Manginell's data is examined as a possibility because of the importance of polysilicon's grain size in contributing to the scattering mechanisms that lead to the temperature dependence and to aid in characterizing MUMPs polysilicon. The constant value of 32 W/m/K [53] has been used previously with MUMPs polysilicon [5]. A constant value is reasonable with smaller grain-sizes and high dopant concentrations (10^{20} atoms/cm^3), and may still account for

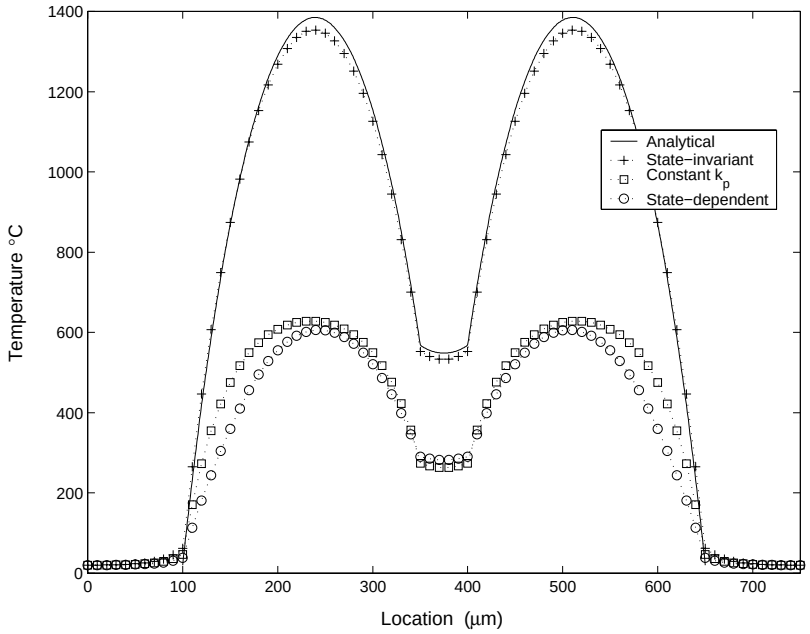

Figure 4.4 - Steady-state profile in air at 5.0 mA

temperature dependencies in a broad temperature range with the appropriate type of polysilicon.

4.2.1 Temperature Profiles

Figure 4.4 shows the steady-state temperature profiles obtained for a two-leg TIM in air with a constant 5.0 mA input. From the profiles, it is clear that the analytical solution from Equation 3.7 and the state-invariant solution (constant k_p and k_{air}) are in good agreement as expected. Since the state-invariant finite-difference model includes radiation to the surroundings, its temperature profile is slightly lower (2.3 percent at the peak temperatures). Because heat is conducted efficiently through the air from the shuttle to the substrate, the shuttle temperature is significantly lower than that of the legs.

In the constant-k_p and state-dependent models, the effect of the differences in thermal conductivity is not strongly apparent. The lower steady-state temperatures near the bond pads, however, are the result of the difference in room temperature values of 72 W/m/K versus 32 W/m/K. At higher temperatures, they are nearly the same.

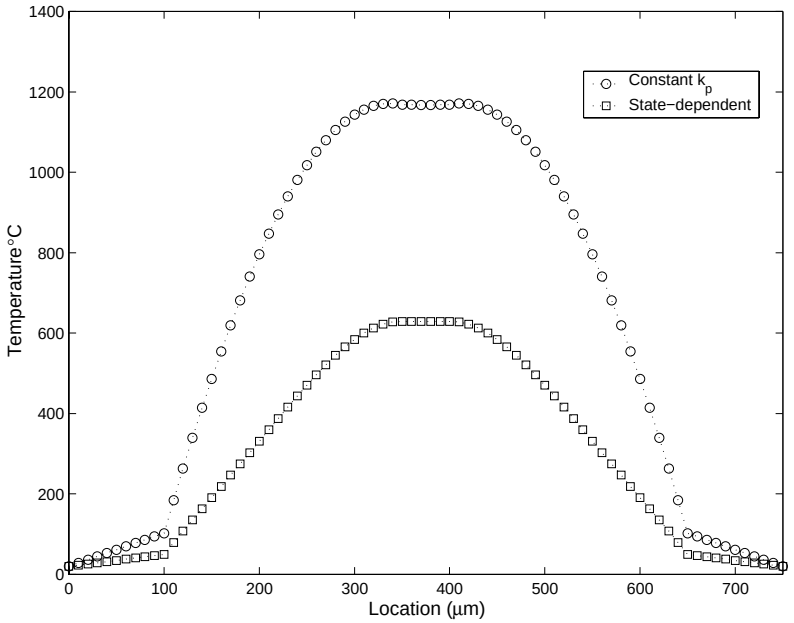

Figure 4.5 - Steady-state profile in vacuum at 1.4 mA

The largest effect that any one parameter has is the thermal conductivity of air, as evidenced from the results from the constant-k_p and the state-dependent models in Figure 4.4. The thermal conductivity of gases is strongly dependent on temperature and because k_{air} increases with temperature, there is more heat transferred to a cooler substrate. This keeps the TIM cool and will limit deflection. Based on a peak temperature drop of 46 percent from the state-invariant model, the results from Figure 4.4 suggest that modeling conduction through the air to the substrate using a temperature-dependent coefficient can significantly alter the simulated temperature profile in the TIM.

In a vacuum, the resulting temperature profiles are noticeably different as Figure 4.5 shows. Because no heat is conducted to the substrate in a vacuum (which is the primary heat transfer method in air), the shuttle temperature rises and eventually becomes the highest temperature in the actuator. Tests in a vacuum take advantage of the insulation provided by removing the medium (air) for heat transfer. The insulation removes the paths for heat flow by means of conduction to the substrate and allows smaller input

currents to reach the same higher temperatures achievable in open air. This reduces the overall power requirements to maintain a steady displacement.

To simulate the vacuum environment, the q_{cond} term in Equation 3.13, which represents heat conduction down to the substrate, was eliminated from the model. This has the effect of insulating the TIM, leaving conduction through the legs to the bond pads and radiation of heat to the surroundings as the only paths for heat flow. With this insulating effect, the TIM in the vacuum reaches steady-state peak temperatures greater than 600 C with a much lower input current. Comparing the state-dependent results from Figures 4.4 and 4.5 shows that in a vacuum, an input current of 1.4 mA causes a peak temperature the same as 5.0 mA in air. Since actuator displacement increases with leg temperature, this indicates that TIM devices can be operated with much lower steady-state power in a vacuum.

For the 1.4 mA vacuum results shown in Figure 4.5, the difference between the constant-k_p model and the state-dependent model is more pronounced than in air at 5.0 mA. For slightly higher currents, this difference in temperature profiles decreases significantly as the legs become hotter and the difference in the k_p values between the two models is much smaller. For example, at 1.5 mA, the peak temperatures between the two models differ only by 22 percent.

A difference between the temperature profiles in air and vacuum can also be seen at the bond pads. In air, the temperature in the pads remains reasonably constant. This supports the assumption that the temperatures at the ends of the actuator are equal to the ambient during the heating process. In a vacuum, there is an increase in temperature at the point where the leg meets the contact pad. In Figure 4.5 the temperature rise is 30 °C at this location for the state-dependent model. This increase in temperature is small enough to support using the assumption of a constant temperature boundary condition without modeling pad heating for sufficiently long actuator legs.

4.2.2 Steady-State Model Validation

Because of the difficulty in measuring temperatures directly from a TIM device, indirect approaches were used to validate the model. The first approach involved using the nodal temperatures from the model as inputs to a commercial finite-element code (ANSYS) to predict the steady-state shuttle deflection and then comparing this with the shuttle deflection measured experimentally under the same conditions. A second validation approach involved photographing the TIM at specific current inputs and looking for two things: the onset and location of visible radiation or the beginning of a small glow, and the charring or destruction of the legs at the melting temperature. The model with the

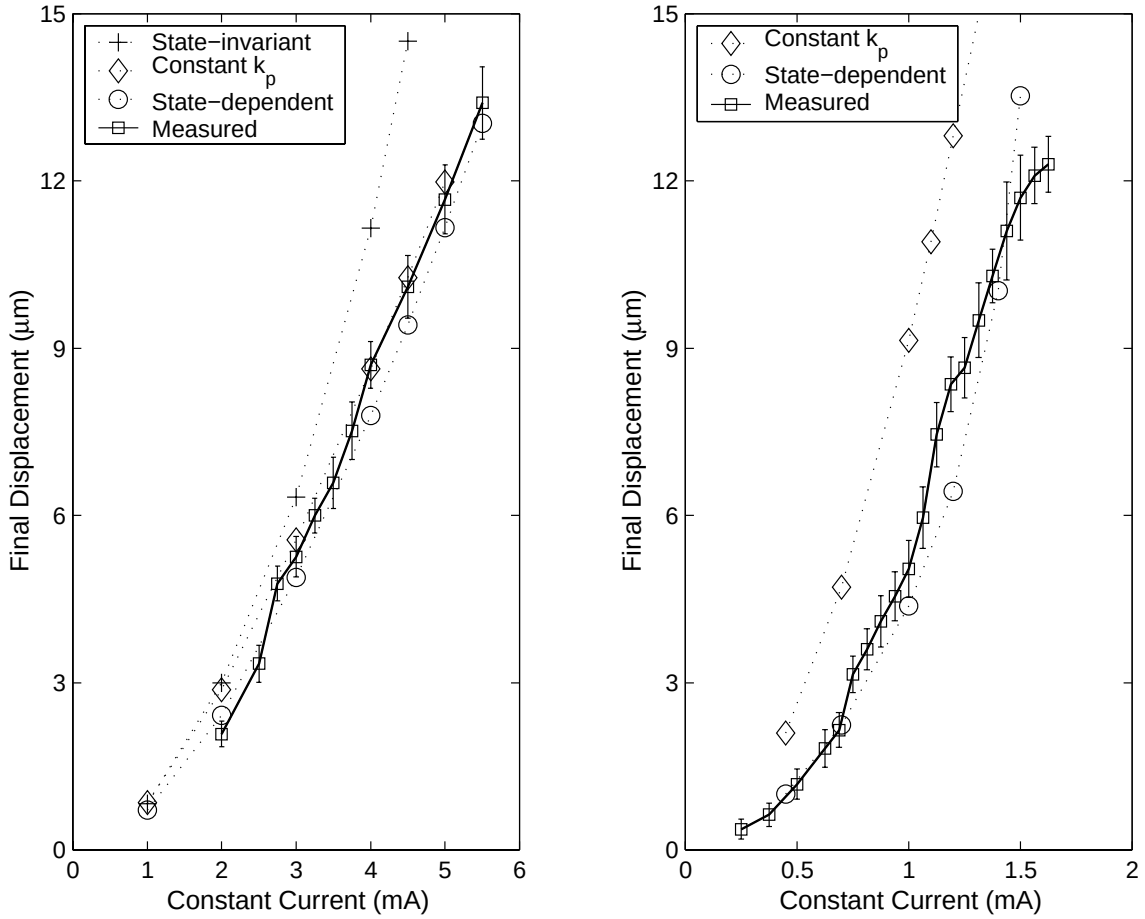

Figure 4.6 – (a) Shuttle displacement versus current in air and (b) displacement versus current in vacuum.

best validation at steady-state is used to further validate predictions of the transient response and force/displacement performance from a TIM.

Figure 4.6 shows how experimental measurements of deflection match the predicted results. Figure 4.6a represents the average of four tests on five different actuators in air; Figure 4.6b is the average of four tests on two different actuators in a high vacuum ($1\times10^{-5} torr$). Error bars represent one standard deviation. Model predictions were made with each of the cases discussed above. In this manner, the importance of temperature dependencies for significant parameters is examined.

As Figure 4.6a shows, a good fit to the data from in-air tests is obtained by using a k_p and k_{air} that is dependent on temperature. This result is also seen for the vacuum results in Figure 4.6b. In a vacuum, the deviation of the model at higher current and deflections is believed to be the result of self-annealing and localized melting at the grain boundaries. At these deflections, temperatures are sufficient to cause secondary-breakdown in the polysilicon [13]. The secondary-breakdown causes a resistance decrease that can be explained in terms of a segregation of impurity atoms in the subsequent solidification process [29]. This deviation was also observed for in-air tests beyond the applied current values plotted in Figure 4.6a.

Figure 4.6a also demonstrates the importance of included a varying k_{air} parameter. At higher temperatures and displacements, the temperature dependence on the thermal conductivity for air is strong, and must be included for accurate model predictions. In Figure 4.6b, where air is not a factor, the model suggests that a constant value for the thermal conductivity of laminate MUMPs polysilicon leads to inaccuracies for temperature and displacement predictions. In air, however, the inaccuracy is masked by the more dominant effect of including a varying k_{air} parameter.

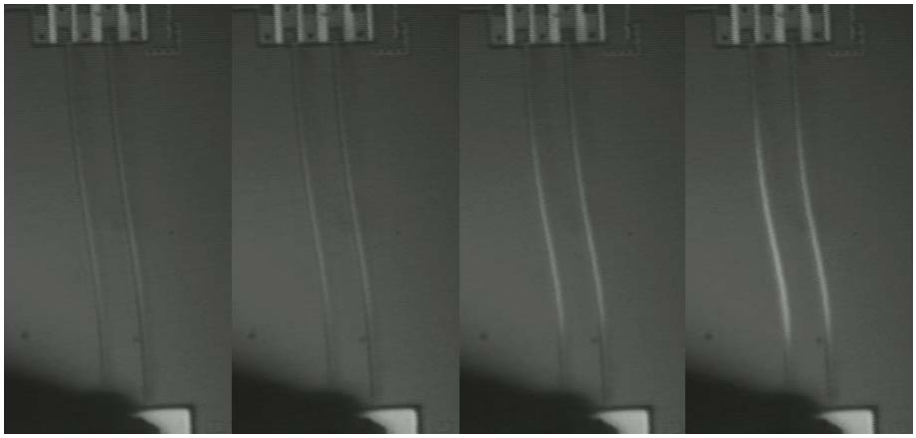

Figure 4.7 - Array of increasing current applied to TIM. From left to right the applied current per leg is 5.75 mA, 6 mA, 6.5 mA, and 7 mA.

Figure 4.7 is an array of video frames captured with slightly increasing current loads. Only half of the TIM is shown due to symmetry. From left to right the current increases across each leg of the TIM at 5.75 mA, 6 mA, 6.5 mA, and 7 mA successively. It is clear from each frame that the position of high-temperature regions observed experimentally are consistent with those obtained from the model (see Figure 4.4). The first frame offers support for the use of a temperature-dependent k_{air} model. The model predicts the small glow seen at 5.75 mA has a peak temperature of 864 C while the constant-k_{air} model predicts peak temperatures beyond the melting temperature (1411 C). This supports including a temperature-dependent k_{air} term along with a temperature-dependent k_p expression for more accurate modeling. In the last frame at 7 mA, the predicted temperature is beyond the melting point at 1431 C with the state-dependent model. This temperature is not expected to be exact because of changes in the resistance of polysilicon at high temperatures. Upon increasing the current in the legs to 7.25 mA, the legs melted.

4.3 DYNAMIC SIMULATIONS

The different paths available for heat transfer between air and vacuum also affect the temperature response time of the TIM. Because the state-dependent model fit the

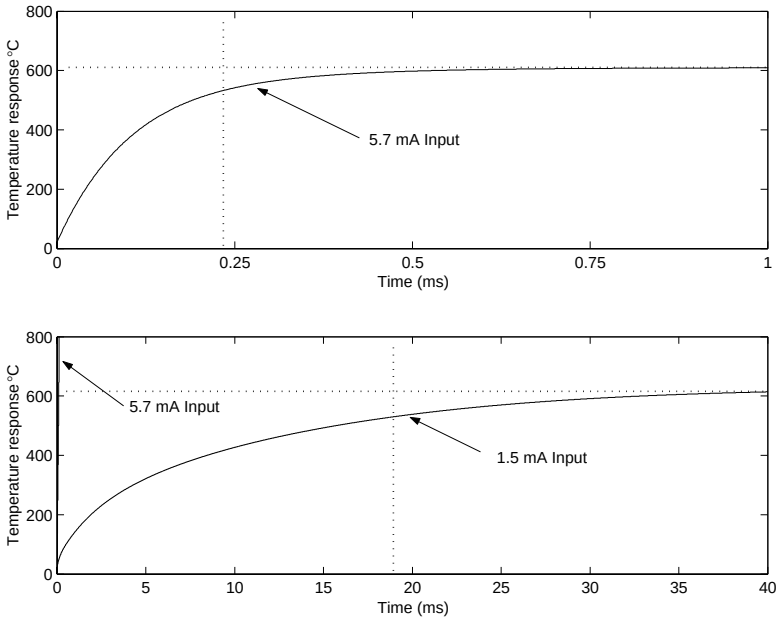

Figure 4.8 - (Top) Temperature response of legs in air, and (Bottom) response of legs in a high vacuum.

experimental tests the best, only results from this model's simulations are discussed. The model results of Figure 4.8 show that the average leg temperature in a vacuum rises much faster than in air with the same current (5.7 mA). However, this magnitude of current input will not allow steady-state temperatures to be reached before melting occurs. When the current is reduced to allow the same average temperature to be obtained at steady-state, the transient in a vacuum is approximately 40 times slower than in air. When a steady-state temperature profile is desired, simulation studies show this difference in the response time is maintained regardless of the magnitude of the current input in each environment. With a steady-current input, the temperature profiles in air shown in Figure 4.4 are achieved in less than 2 msec. In a vacuum, the temperature transient response is slower for two reasons: (1) the smaller input current necessary in vacuum environments to prevent melting does not provide the same level of internal joule heating when compared to air, and (2) the vacuum environment acts as a resistance that impedes the flow of heat by conduction to the substrate. Because the system behaves as a first order system, the electrothermal system is controlled by a time constant equal to the product of thermal resistance and the thermal capacitance. The vacuum environment increases the thermal resistance and therefore increases the system time constant. Note also that

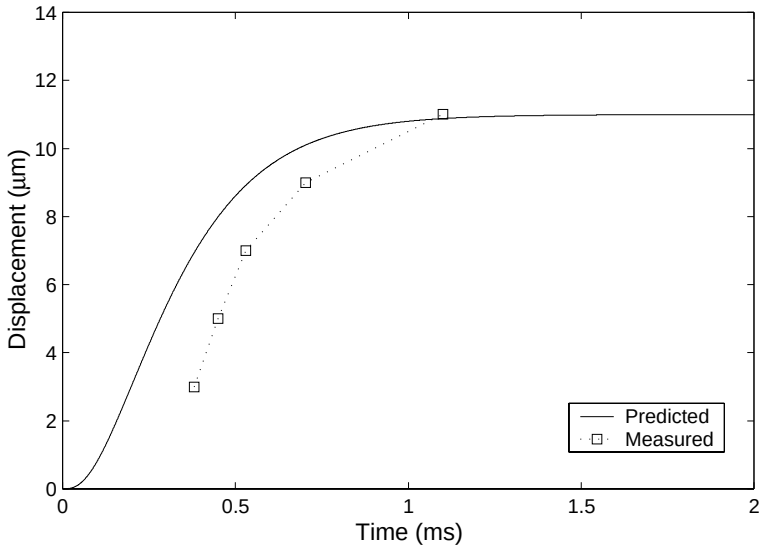

Figure 4.9 – Transient response predictions from model compared to measured data

smaller shuttles would decrease the system thermal capacitance and improve transient response.

4.3.1 Dynamic Tests

To measure the response time of a TIM to current inputs, the time constant from the HP 4145a was first characterized. Although the amplifier is programmed to give current step inputs to the TIM, the internal dynamics of the amplifier prevent the steps from occurring instantaneously. While the time constant of the amplifier is small, it is significant given the high-speed response of the TIM. The measurement of the amplifier time constant was performed by connecting different values of resistance across the microprobes that would be used to actuate the TIM. The values of resistance ranged from 100 Ω to 26.9 kΩ. The HP 4145a was then used to supply a constant current input that ranged from 550 μA to 10 mA and a digital oscilloscope recorded the voltage across the resistor. Because the resistance is assumed constant (the voltage was repeatable within 4 mV for each resistor and applied current value), the oscilloscope trace is an accurate representation of the current input from the HP 4145a. A time constant of 0.190 ms was measured regardless of the value of resistance or input current.

The current input to the finite-difference model was modified from an abrupt step to a first-order step response having the same time constant as the HP 4145a. Figure 4.9 shows the simulation results compared to the measured data using the setup of Section 4.1.3. The steady-state value of the current used in the simulation was the same value provided to the TIM for each leg-pair. Figure 4.9 demonstrates that the predicted shape of the transient from the model is in good agreement with measured data. It is also evident that steady-state displacement is achieved shortly after 1 ms. However, there is a noticeable shift in the measured data to values that occur later in time. This shift is approximately 250 μs for the data at smaller displacements (3 and 5 μm).

It is believed that the shift in time observed with the measured data can be attributed to stick-slip friction. This type of friction would cause the TIM to delay its motion for a short period until a critical force is reached. When enough force is present from thermal expansion to surpass the critical force, slip will occur and movement is observed. This type of behavior is characterized by a higher coefficient for static friction at zero velocity until a certain threshold in an applied force causes the device to break free (slip) with a new kinetic friction coefficient. The kinetic friction coefficient during slip is less than the static friction coefficient.

Stick-slip friction has been observed experimentally. When applying smaller input currents (capable of achieving detectable submicron deflection), a result that will sometimes occur is that a gradual movement is not observed, but rather no motion is visible until the current is increased to the point where a deflection is suddenly detectable at larger deflections. These observations are within the resolution of the level of magnification used and not the result of pixel error (see Section 4.1.1). It is also noted that after a release that is noticeably plagued with stiction effects across the die, TIM devices can often be freed from the substrate with successive pulses of an applied current. In a TIM at rest, friction is possibly caused by dimples on the bottom of the shuttle coming into contact with the substrate. This contact could occur during the release process if capillary forces pull the shuttle down and the dimples touch the substrate (the

air gap under a dimple is nominally 1.25 μm). Although the SAM coatings, discussed in Section 2.2.2, are intended to prevent stiction effects, releases that use the SAM coatings still vary in the amount of stiction observed across the die. It is reasonable, therefore, to assume that a small amount of stick-slip friction is affecting the transient response of the TIM.

4.3.2 Steady-State Power and Energy Consumption

The power demands at steady-state, and the energy required to change the average temperature in the actuator are important performance criteria for thermal actuators. In this research, the energy required during the transient response is calculated by integrating the instantaneous power provided to the TIM when given a step input in current. The integration is carried out from the time the step input is applied until the time when the transient is 90 percent complete. The dotted vertical line in Figure 4.8 represents the amount of time elapsed to reach 90 percent of the final average temperature. This rise time is 0.22 ms for air and 18.5 ms under vacuum. Figure 4.10 shows the power required and energy used to achieve the steady-state temperature responses of Figure 4.8. A significantly lower steady-state power is needed in a vacuum to obtain the same average temperature rise in the expansion legs because of the smaller input current. This difference is 87.8 mW in air versus 6.4 mW in a high vacuum. However, over five times the amount of total energy is consumed to reach a steady temperature profile in a vacuum under these conditions than during the temperature transient in air (15.4 μJ versus 85.4 μJ).

The trend in the power requirements and energy usage evident in Figure 4.10 is more pronounced as the average leg temperature increases. Figure 4.11a shows the model predictions for the steady-state power necessary to maintain average temperatures in both air and vacuum. To achieve common displacements (8 to 12 μm) from a TIM device, average temperatures in a leg are between 300 C and 500 C. Figure 4.11b indicates that when the energy consumed is compared in the two environments, the energy needed to reach this range of higher temperatures in a vacuum is always larger than in open air.

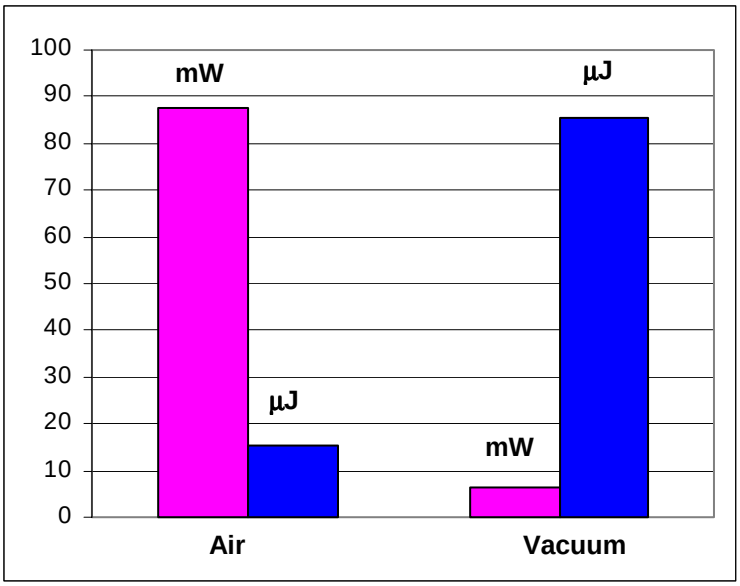

Figure 4.10 - Power and energy used for steady-state temperature responses in Figure 4.8.

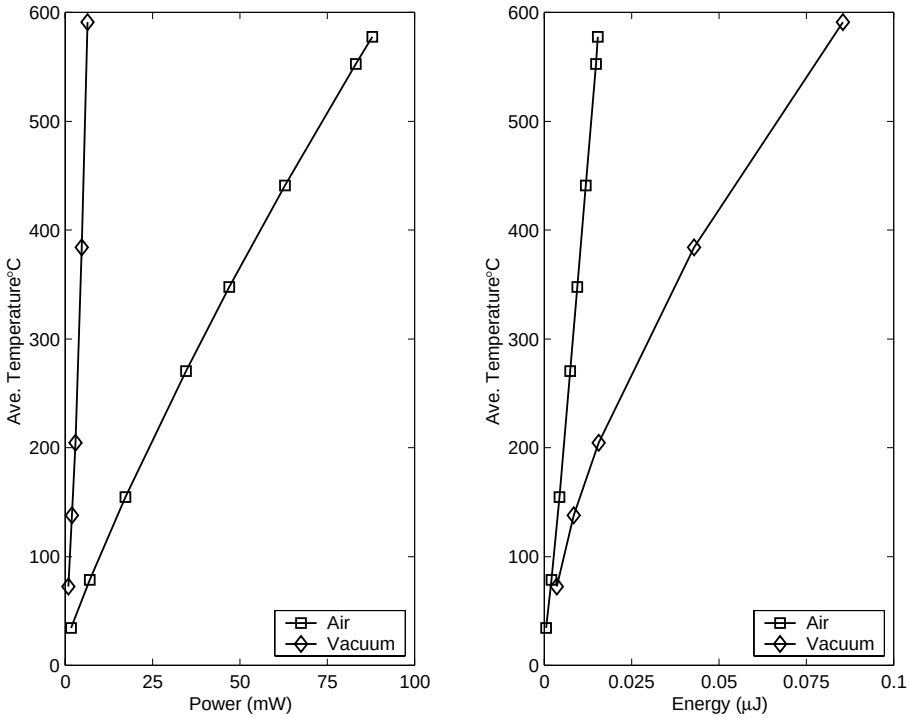

(a) (b)

Figure 4.11 – (a) Steady-state leg temperature versus power input and (b) steady-state leg temperature versus energy consumed.

This is a direct result of the slower transient response between the air and vacuum ambients caused by the smaller input current in a vacuum.

4.4 PULSE SIMULATIONS

To this point, all simulations have used a constant current that was safe for each ambient condition (the constant current would not burn out the device). By providing short duration current pulses to the device in a vacuum, improved transient response and energy efficiency can be achieved. This is also suggested by the much faster rise time of the average leg temperature when the same input current is used in both air and vacuum (Figure 4.8). To test this assertion, the model was adjusted to give high current pulses to the TIM to study the result on energy consumed. In the model, the q_i term was activated for 0.25 msec with a current input of 4.0 mA. A steady application of this level of current in a vacuum would normally heat the TIM past its melting temperature, but for this duration it brings the TIM to a peak temperature of 913 C. Figure 4.12 shows the result of this simulation. Notice the shuttle does not have sufficient time to climb to a high temperature and that the highest temperatures occur in the more useful area of the legs, where thermal expansion is desired. This increases the average temperature in the

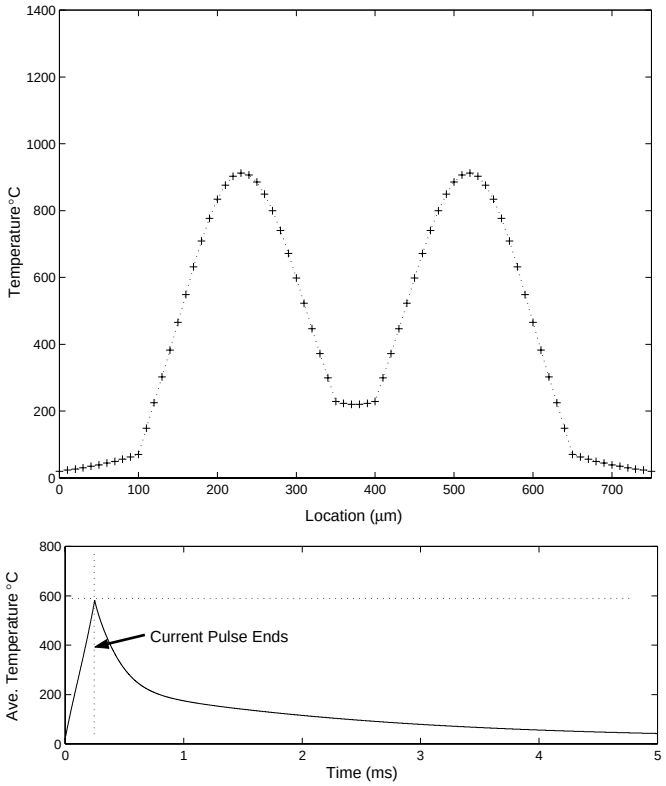

Figure 4.12 - (Top) Temperature profile and (Bottom) Transient heating of a TIM pulsed in a vacuum.

legs and will result in slightly more deflection at this peak temperature than the same high temperature would achieve with a stable current. Also evident in Figure 4.12, the average temperature in the legs follows the current impulse well. This suggests the actuator would work well in vacuum for switching tasks where a fast rise time is important provided that short, high-current pulses are used. Since the applied current must be removed before melting temperatures are reached, the TIM does not reach a steady temperature profile. This simulation required only 8.7 μJ of energy to go through the same average temperature as Figure 4.8. This is an energy saving of almost 90 percent to reach the same displacement and average temperature simulated in air.

4.5 FORCE SIMULATIONS

As mentioned in Chapter 3, the available force from a TIM is simulated with finite-element software. The steady-state temperatures from the state-dependent finite-difference model are applied as loads to mechanical beam elements and the resulting leg growth is computed with the coefficient for thermal expansion from Equation 3.22. In this manner, the steady-state deflection from a TIM is solved for. After the final displacement of the TIM has been found with FEA, the available force from zero deflection through the entire travel of the TIM is found by recording the reaction forces on the TIM shuttle at intermediate displacements. Figure 4.13 demonstrates the above procedure with FEA software. The colors on the beam show the temperature profile with respect the legend in the figure. The top graphic is the TIM at full displacement. There is no reaction force on the shuttle at full travel and therefore, no available output force. The middle graphic shows the TIM at 75 percent of full travel while the white arrow represents the reaction force. Fixing the displacement of the shuttle at the distance where the magnitude of the force is desired creates the reaction force. In ANSYS, the force is found after summing the nodal reaction forces on the TIM's shuttle. The bottom graphic of the TIM is at 50 percent of the full steady-state displacement. This simulation shows how the TIM has buckled to a slightly different shape. This buckled shape results in a reaction force that is smaller in magnitude than before buckling occurs. While TIMs with

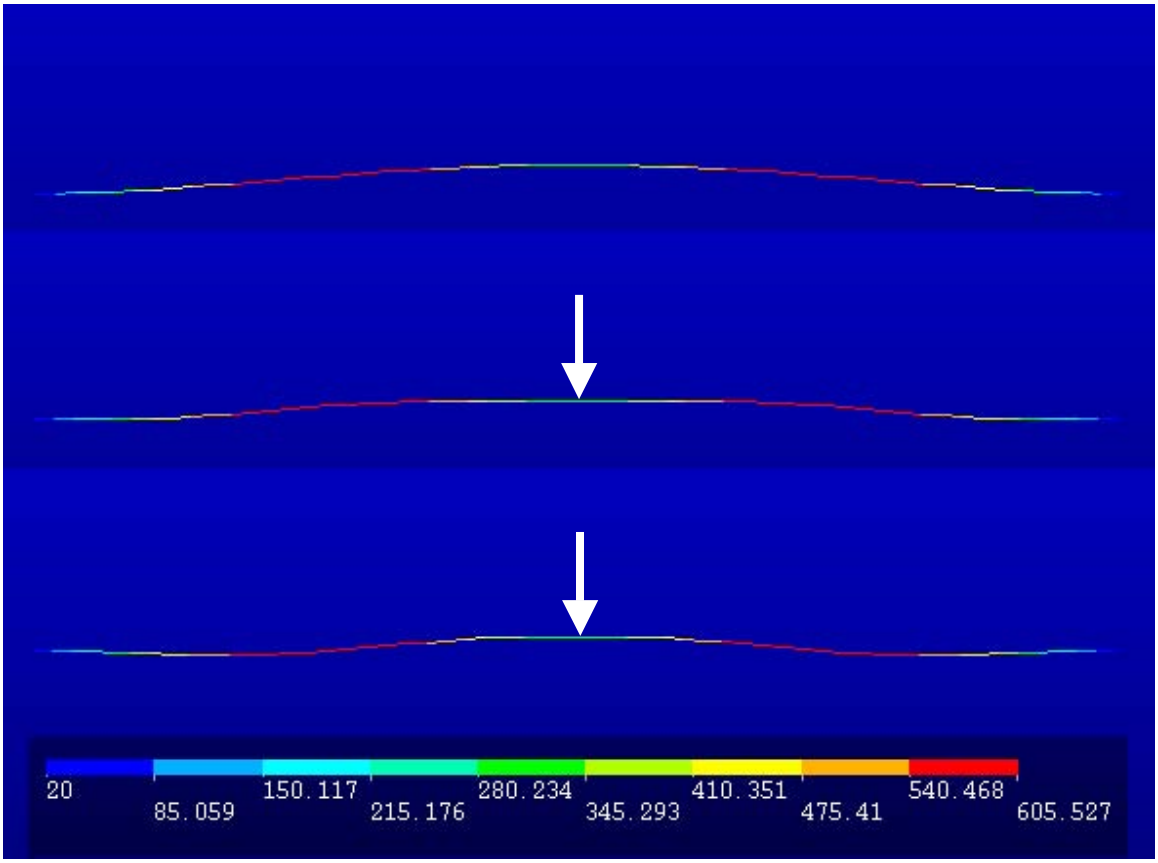

Figure 4.13 – FEA simulations to determine the maximum force versus displacement from a TIM.

longer legs can achieve larger displacements under no load, their tendency to buckle increases [10]. Part of the motivation of this thesis to study leg lengths equal to 250 μm is that this length provides a good balance between large displacements with fewer tendencies to buckle for many applications.

4.5.1 Force Tests

In order to test the model predictions for the maximum force output through the range of the actuator's travel, a test was conducted with the micromachined force gauges discussed in Section 4.1.2. The results of this test for an eight leg-pair TIM with length *L* equal to 250 μm and offset *f* equal to 3 μm is shown in Figure 4.14. The current through all eight leg-pairs was 34 mA. The uncertainties in the force and position measurements are also shown in Figure 4.14. The uncertainty in the force takes into account the

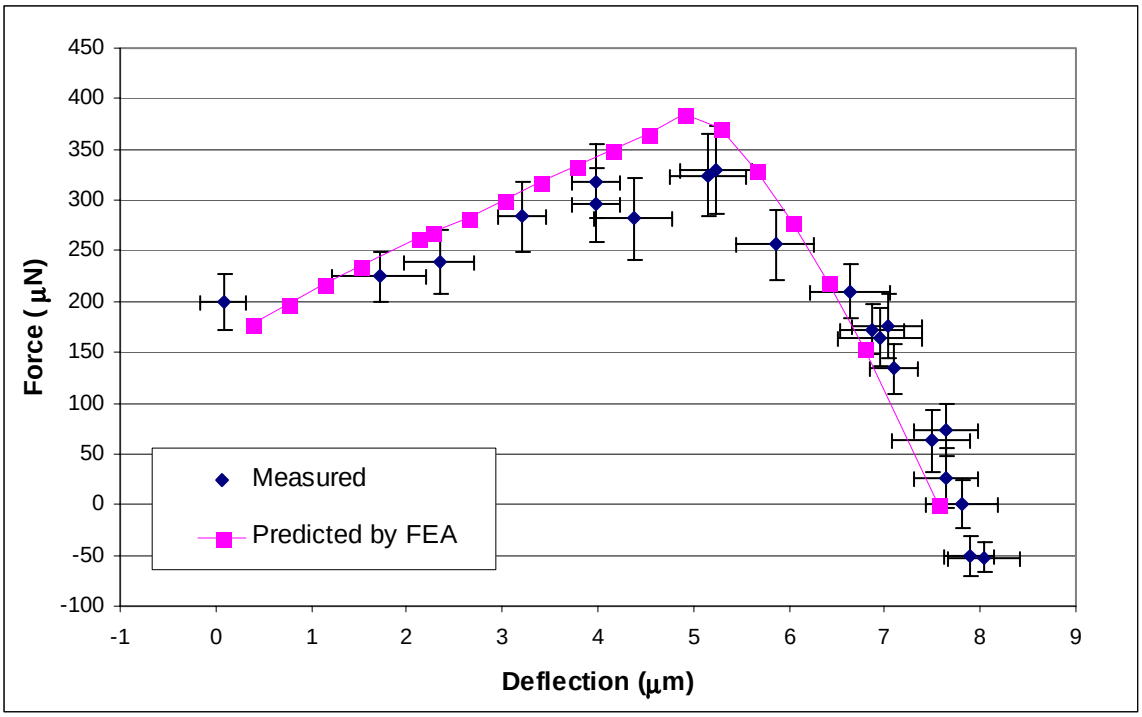

Figure 4.14 – Force versus displacement data for a TIM comparing measured results to FEA predictions.

uncertainty in each of the variables within the force equation (Equation 4.1). For a compete derivation of the uncertainty in the force measurements, refer to Wittwer et al. [57]. From Figure 4.14, it is evident that FEA results are in good agreement with measured data. The peak force, which occurs at approximately 5 µm of displacement, correlates well with the experimental results. Additionally, the lower forces at the smaller displacements match the experimental results and agree with the predictions that buckling decreases the amount of available force.

Chapter 5

CONCLUSIONS

This chapter includes three sections. The first section reviews the problem description from Chapter 1 and discusses the solution approach taken by this research. The second section reviews the results from the models developed herein. The last section contains recommendations for future work and subsequent use of the models developed by this thesis.

5.1 PROBLEM DESCRIPTION AND SOLUTION APPROACH

Ideally, actuators would have low power consumption, high force output, reliable and repeatable operation, design flexibility, and simple drive circuitry all in the smallest package possible. In the micro-world, polysilicon electrothermal microactuators have distinguished themselves with many of these positive characteristics. Specifically, these positive traits include large displacements and output forces with the ability to be driven at CMOS compatible voltages and currents. The Thermomechanical In-plane Microactuator or TIM, the subject of this thesis, is a unique microactuator in this category because it also simple to construct (requiring only a single releasable layer), extremely flexible in design, and can operate with simple drive and control circuitry. When compared to the widely-used electrostatic micromachined strategies, these positive traits demand that consideration be given to electrothermal actuation for the integration into complete micro-systems.

However, electrothermal actuation has some negative traits as well. In general, thermal actuators operate by tailoring specific parts of a device's geometry to heat up and expand upon external heating or an applied current. The required heat generated for thermal expansion consumes considerably more power than electrostatic or piezoelectric actuation counterparts. The amount of power necessary for thermal expansion should be characterized at the design stage and may be the limiting factor for this type of actuation strategy in many applications.

The problem, as proposed in this thesis, is to develop a comprehensive electro-thermo-mechanical simulation of a TIM device. This thesis takes a finite-difference approach to create a model that predicts temperatures, power requirements, and energy consumed by a TIM. Because the speed of response, total displacement, and force are also important specifications, models have been developed to utilize the electrothermal finite-difference solutions to characterize these factors as well. This includes the use of finite-element software.

5.2 SUMMARY OF RESULTS AND CONCLUSIONS

After comparing the experimental results to the simulations presented in this thesis, the following conclusions can be made:

1. Simulation results from the finite-difference model accurately predict the temperature profile across the fundamental beam when given a current input. This was verified indirectly by measuring the steady-state displacement that resulted from thermal expansion and comparing the experimental data to solutions from nonlinear finite-element commercial software and pseudo-rigid-body approximations. Knowledge of temperature dependencies for the resistivity and thermal conductivity of polysilicon is critical for accurate predictions. At high temperatures experienced by a TIM, the temperature dependency for the

thermal conductivity of air (in open-air environments) must be accounted for to achieve good results.

2. An explicit equation from a pseudo-rigid-body approximation is developed that predicts the displacement of a TIM after the amount of thermal expansion is calculated from joule heating. When this equation is coupled to the finite-difference model at each time step, transient deflections of the TIM can be modeled.

3. The power required to maintain steady-state position and the energy consumed during the transient are available from the simulation results. Simulations with the model also indicate that substantial gains in the required power are available in vacuum ambients. Additionally, pulsing the TIM in a vacuum with high-current short-duration pulses will improve both the transient response and energy consumption characteristics. This is beneficial when the TIM can function as an actuator for single-pulse switching applications, but requires the ability to package the device in a vacuum.

4. Results from the electrothermal model were able to accurately predict the available force from a TIM throughout its range of motion. A novel micromachined force gauge was used to gather experimental data to compare with the model. The force from a TIM is not a maximum at zero displacement but is smaller in magnitude because of buckling.

In summary, using the models in this thesis will be a valuable tool in improving and optimizing the TIM for specific applications.

5.3 RECOMMENDATIONS FOR FUTURE WORK

The TIM is an extremely flexible design that can be used in numerous applications. The development of the models for this thesis has led to ideas for continuing study. This section discusses a few of the foreseeable research opportunities.

First, one of the important physical parameters that affects the performance and ability to characterize the TIM accurately is the thermal conductivity of polysilicon. The thermal conductivity is highly dependent on the method of deposition. Because the thermal conductivity of MUMPs polysilicon is not known, its study is recommended as a noteworthy pursuit. One method that appears promising would use the method suggested by Manginell [41]. In his thesis, the resistance decay (or cooling) of a microbridge allows the thermal diffusivity to be ascertained after the cooling time constant has been found. After the thermal diffusivity is known, the thermal conductivity is found using the relationship that thermal conductivity is equal to the product of the specific heat times the thermal diffusivity. Manginell used the known temperature dependence for the specific heat of crystalline silicon to calculate his results for the thermal conductivity of polysilicon.

A recommended use for the models would be to link the finite-difference model to optimization software. The optimization could be run with objectives to maximize displacement and minimize the steady-state power while keeping the nodal temperatures below a safe limit. To be compatible with the discrete elements of the finite-difference approximation, optimization routines that can employ discrete design variables must be used. A further extension could link the results from the finite-difference model to finite-element code to maximize the force over a desired range of displacement.

Simulations with the model investigated the possibility of high-current pulses in a vacuum to improve the transient response and energy used to reach a desired deflection. Experiments should be performed to test this assertion. Equipment is currently available to perform these experiments with the exception of the control circuitry that could

provide pulse durations less than 250 μs. With such control or timing circuitry in hand, these tests could be performed using devices already available and the test setup discussed in Section 4.1.3. Also, the level of vacuum needed to obtain the significant power improvements observed within the high vacuum from the SEM chamber may be overly excessive and unnecessary. Similar improvements with power reduction may be observed at lower vacuum levels. A variable vacuum chamber could be used to perform tests where the level of vacuum can be controlled. A vacuum level to power correlation could then be obtained that would provide valuable information on the package requirements. Again, these tests could be performed with the currently fabricated devices.

Recent attempts to improve the power requirements in air have lead to a consideration for moving the legs of a TIM closer together. This provides an insulation barrier between the legs and the resulting heat flow by conduction to the substrate is reduced. The finite-difference model can account for this by modifying the shape factor. A suggested method would involve the creation of an insulation factor that would be a function of the distance between legs. The insulation factor could be found in the same way the shape factor was initially determined by using finite-element analysis to calculate the ratio of total heat flux from a volume element of unit depth to the expected heat flux out the bottom surface as a function of the distance between legs.

Finally, closed-loop position control of a TIM should be attempted. The models developed by this research will play an integral role in interpreting device behavior. To complete the loop, a parallel-plate capacitance sensor, with the shuttle acting as one electrode and the substrate as the other, could provide an error signal for position. This method has been used similarly to control electrostatic microactuators. However, the capacitance change is quite small and requires advanced circuitry to be fabricated on-chip to help avoid stray and parasitic capacitance. Instead, one can control the resistance of a TIM and measure the power needed to maintain that resistance value. Interpretation of the result then requires careful correlation between resistance, temperature, and displacement.

REFERENCES

[1] Amemiya, Y., Ono, T., and Kato, K., 1979, "Electrical Trimming of Heavily Doped Polycrystalline Silicon Resistors," IEEE Transaction on Electron Devices, Vol. 26 No. 11, pp. 1738-1742.

[2] Baker, M.S., Lyon, S.M., and Howell, L.L., 2000, "A Linear Displacement Bistable Micromechanism," Proceedings of the 2000 ASME Design Technical Conferences, DETC00/MECH-14117.

[3] Barin, I., 1993, "Thermochemical Data of Pure Substances," VCH, Weinheim.

[4] Burns, R.H., and Crossley, F.R.E., 1968, "Kinetostatic Synthesis of Flexible Link Mechanisms," ASME Paper No. 68-MECH-36.

[5] Butler, J.T., and Bright, V.M., 1998, "Electrothermal and Fabrication Modeling of Polysilicon Thermal Actuators," ASME DSC-MEMS - Vol. 66, pp. 571-576.

[6] Butler, J.T., Bright, V.M, and Cowan, W.D., 1999, "Average Power Control and Positioning of Polysilicon Thermal Actuators," Sensors and Actuators A, Vol. 72, pp. 88-97.

[7] Comtois, J., Bright, V., Gustafson, S. and Michalicek, M., 1995, "Implementation of Hexagonal Micromirror Arrays as Phase-mostly Spatial Light Modulators," Proc. SPIE Microelectronic Structures and Microelectromechanical Devices for Optical Processing and Multimedia Applications, Vol. 2641, pp. 76-87.

[8] Comtois, J.H., Bright, V.M., and Phipps, M.W., 1995, "Thermal microactuators for surface-micromachining processes." SPIE, Vol. 2642, pp. 10-21.

[9] Conant, R. A., and Muller, R.S., 1998, "Cyclic Fatigue Testing of Surface-micromachined Thermal Actuators," ASME DSC-MEMS – Vol. 66, pp.273-277.

[10] Cragun, Rebecca, 1999, "Thermal Microactuators For Microelectromechanical Systems (MEMS)," MS Thesis, Brigham Young University.

[11] Fedder, G.K., and Howe, R.T., 1991, “Thermal Assembly of Polysilicon Microstructures,” Proceedings of the IEEE Micro Electro Mechanical System Workshop, pp. 63-68.

[12] Ghaddar, C.K., Kuijk, J., Gilbert, J.R., Cowan, W.D., Butler, J.T., and Bright, V.M., 1998, “Simulation and Design of Electro-Thermally Actuated MEMS Devices,” ASME Mechanical Systems (MEMS) 1998, pp. 293-298.

[13] Greve, D.W., 1982, “Programming Mechanism of Polysilicon Resistor Fuses,” IEEE Transaction on Electron Devices, Vol. 29, No. 4, pp. 719-724.

[14] Holman, J.P., 1997, “Heat Transfer,” 8th Ed., McGraw-Hill.

[15] Howell, L.L., 2001, “Compliant Mechanisms,” Wiley, New York, New York.

[16] Howell, L.L., and Leonard, J.N., 1997, “Optimal Loading Conditions for Non-Linear Deflections,” International Journal of Non-Linear Mechanics, Vol. 32, No. 3, pp. 505-514.

[17] Howell, L.L., and Midha, A., 1995, “Parametric Deflection Approximations for End-Loaded, Large-Deflection Beams in Compliant Mechanisms,” Journal of Mechanical Design, Vol. 117, March, pp. 156-165.

[18] http://www.ansys.com/

[19] http://www.ansys.com/action/MEMSinitiative/

[20] http://www.edocorp.com/

[21] http://www.mathworks.com/

[22] Huang, Q.A., and Lee, N.K.S., 1999, “Analysis and Design of Polysilicon Thermal Flexure Actuator,” Journal of Micromechanics and Microengineering, Vol. 9, pp.64-70.

[23] Huang, Q.A., and Lee, N.K.S., 1999, “Analytical Modeling and Optimization for a Laterally-driven Polysilicon Thermal Actuator,” Microsystem Technologies, Vol. 5, pp. 133-137.

[24] Incropera, F.P., and DeWitt, D.P., 1996, "Introduction to Heat Transfer," 3rd Ed., John Wiley, New York.

[25] Jensen, B.D., Howell, L.L., and Salmon, L.G., 1998, "Design of Two-Link, In-Plane, Bistable Compliant Micromechanisms," Proceedings of the 1998 ASME Design Technical Conferences, DETC98/MECH-5837.

[26] Jonsmann, J., Sigmund, O., and Bouwstra, S., 1999, "Compliant Electro-Thermal Microactuators," IEEE 1999, pp. 588-593.

[27] Judy, J.W., Tamagawa, T., and Polla, D.L., 1990, "Surface Micromachined Linear Thermal Microactuator," IEEE IEDM, pp. 629-632.

[28] Kamins, T., 1998, "Polycrystalline Silicon for Integrated Circuits and Displays," 2nd Ed., Kluwer, Boston.

[29] Kato, K., and Ono, T., 1982, "A Physical Mechanism of Current-Induced Resistance Decrease in Heavily Doped Polysilicon Resistors," IEEE Transaction on Electron Devices, Vol. 29, No. 8, pp. 1156-1160.

[30] Kennedy, J.B., and Madugula, M.K.S., 1990, "Elastic Analysis of Structures," Harper and Row, New York, Ch. 7 and 9.

[31] Kladitis, P.E., and Bright, V.M., 2000, "Prototype Microrobots for Micro-positioning and Micro-unmanned vehicles," Sensors and Actuators, Vol. 80, pp. 132-137.

[32] Koester, D.A., Mahadevan, R., Hardy, B., and Markus, K. W., 2000, "MUMPs Design Handbook: Rev. 5.0," Cronos Integrated Microsystems, 3021 Cornwallis Rd., Research Triangle Park, NC 27709.

[33] Kolesar, E.S., Allen, P.B., Howard, J.T., Wilken, J.M., and Boydston, N., 1999, "Thermally-actuated Cantilever Beam for Achieving Large In-plane Mechanical Deflections," Thin Solid Films, Vol. 355-356, pp. 295-302.

[34] Lee, J.Y., Kang, S.W., 1999, "A Characterization of the Thermal Parameters of Thermally Driven Polysilicon Microbridge Actuators Using Electrical Impedance Analysis," Sensors and Actuators, Vol. 75, pp. 86-92.

[35] Lerch, P., Slimane, C.K., Romanowicz, B., and Renaud, P., 1996, "Modelization and Characterization of Asymmetrical Thermal Micro-actuators," Journal of Micromechanics and Microengineering, Vol. 6, pp. 134-137.

[36] Lin, L., and Chiao, M., 1996, “Electrothermal Responses of Lineshape Microstructures,” Sensors and Actuators A, Vol. 55, pp. 35-41.

[37] Lin, L., and Pisano, A.P., 1991, “Bubble Forming on a Micro Line Heater,” ASME DSC-Vol. 32, Micromechanical Sensors, Actuators, and Systems, pp.147-163.

[38] Lin, L., Pisano, A.P., and Carey, V.P., 1998, “Thermal Bubble Formulation on Polysilicon Micro Resistors,” Journal of Heat Transfer, Vol. 120, pp. 735-742.

[39] Lyon, S.M., Erickson, P.A., Evans, M.S., and Howell, L.L., 1999, “Prediction of the First Modal Frequency of Compliant Mechanisms Using the Pseudo-Rigid-Body Model,” Journal of Mechanical Design, Vol. 121, pp. 309-313.

[40] Maboudian, R., and Howe, R.T., 1997, “Critical Review: Adhesion in Surface Micromachined Structures,” J. Vac. Sci. Technology. B Vol.15, No. 1, pp. 1-20.

[41] Maginell, R.P., 1997, “Polycrystalline-Silicon Microbridge Combustible Gas Sensor,” Ph.D. Dissertation, University of New Mexico.

[42] Maloney, J., DeVoe, D.L., and Schreiber, D.S., 2000, “Analysis and Design of Electrothermal Actuators Fabricated from Single Crystal Silicon,” ASME MEMS-Vol. 2, pp. 233-240.

[43] Maluf, N., 2000, “An Introduction to Microelectromechanical Systems,” Artech House, Boston.

[44] Mankame, N., and Ananthasuresh, G.K., 2000, “The Effect of Thermal Boundary Conditions and Scaling on Electro-Thermal-Compliant Micro Devices,” Proc. of MSM2000, pp. 609-612.

[45] Mastrangelo, C.H., 1991, “Thermal Applications of Microbridges,” Ph.D. Dissertation, University of California at Berkeley.

[46] Okada, Y., and Tokumaru, Y., 1984, “Precise Determination of Lattice Parameter and Thermal Expansion Coefficient of Silicon Between 300 and 1500 K,” Journal of Applied Physics, Vol. 56, No. 2, pp. 314-320.

[47] Optimas Corporation, 1996, "User Guide and Technical Reference," OPTIMAS 6, 8th Edition, Bothell, Washington.

[48] Pan, C.S. and Hsu, W., 1997, "An Electro-thermally and Laterally Driven Polysilicon Microactuator," Journal of Micromechanics and Microengineering, Vol. 7, pp. 7-13.

[49] Reid, J.R., Bright, V.M., and Comtois, J.H., 1996, "Force Measurements of Polysilicon Thermal Micro-Actuators," SPIE, Vol. 2882, pp. 296-306.

[50] Saxena, A., and Kramer, S.N., 1998, "A Simple and Accurate Method for Determining Large Deflections in Compliant Mechanisms Subjected to End Forces and Moments," Journal of Mechanical Design, Vol. 120, September, pp. 392-400.

[51] Slack, G.A., 1964, "Thermal Conductivity of Pure and Impure Silicon, Silicon Carbide, and Diamond," Journal of Applied Physics, Vol. 35, pp. 3460-3466.

[52] Smith, W.F., 1993, "Foundations of Materials Science and Engineering," 2nd Ed., McGraw-Hill, New York.

[53] Tai, Y.C., Mastrangelo, C.H., and Muller, R.S., 1988, "Thermal Conductivity of Heavily Doped Low-pressure Chemical Vapor Deposited Polycrystalline Silicon Films," Journal of Applied Physics, Vol. 63, No. 5, pp.1442-1447.

[54] Touloukian, Y.S., Powell, R. W., Ho, C.Y., and Klemens, P.G., 1970, "Thermophysical Properties of Matter," IFI/Plenum, New York.

[55] Ulman, A., 1991, "Introduction to Ultra-thin Organic Films: From Langmuir Blodgett to Self-Assembly," San Diego, Academic.

[56] Volkein, F., and Baltes, H., 1992, "A Microstructure for Measurement of Thermal Conductivity of Polysilicon Thin Films," Journal of Microelectromechanical Systems, Vol. 1, No. 4, pp. 193-196.

[57] Wittwer, J.W., Gomm, T., and Howell, L.L., Submitted for publication to Journal of Micromechanics and Microengineering, "Surface Micromachined Force Gauges: Uncertainty and Reliability."

[58] Yang, Y.J., Kim, C.J., Matoba, H., and Muller, R.S., 1994, "Thermal Analysis of a Bistable Microactuator," DSC-Vol. 55-2, Dynamic Systems and Control, pp. 687-693.

APPENDIX A

```
% CDL:  Performs ElectroThermal characterization
% Of a TIM using an implicit finite-difference method.
% Can be run in AIR or VACUUM with a flag.
% Steady-state and transient information is produced.

% Clear the workspace
clear;

% Set REFERENCE TEMPERATURE and offset to Kelvin
T_s = 20;                   % Celsius
Diff = 273.15;              % Offset
T_sK = T_s + Diff;          % Kelvin

% Set FINAL TIME for simulation and time step
% time step must be compatible with size of element
% defined by delta_x
time_final = .002;          %seconds
delta_t = 1e-6;
delta_x = 10e-6;
tf_ms = time_final*1000;

%%%%%%%%%%%%%%%%%%%%%%%%%%%%%%%%%%%%%%%%%%%%%%%%%%%%%%%%%%%%%%%%%%%%%%%
% FLAGS ARE HERE
% 1 - includes heat flow mechanism and 0 - disables heat flow mechanism
%%%%%%%%%%%%%%%%%%%%%%%%%%%%%%%%%%%%%%%%%%%%%%%%%%%%%%%%%%%%%%%%%%%%%%%
bottom_flag = 1;
convect_flag = 0;
radiate_flag = 1;

%%%%%%%%%%%%%%%%%%%%%%%%%%%%%%%%%%%%%%%%%%%%%%%%%%%%%%%%%%%%%%%%%%%%%%%
%       Parameters used in this analysis   %

p0 = 3.4e-5;                        %  Ohm*m
alpha_r = 1.25e-3;                  %  1 / deg C
E = 165e9;                          %  Young's modulus (GPa)
T_expan_polySi = 2.7e-6;            %  1 / deg C
absortivity_polySi = 0.6;           %
```

```
k_polySi = 32;                          %  W/ m / deg C
k_air = .026;                           %  W/ m / deg C
k_Si3Ni4 = 2.25;                        %  W/ m / deg C
k_SiO2 = 1.4;                           %  W/ m / deg C
therm_capacity = 705;                   %  J/ kg / deg C
density = 2330;                         %  kg / m^3
sigma = 5.669e-8;                       %  Stefan-Boltzmann constant
h_conv = 20;                            %  Free Convection coeff.
k_Si = 150;                             %  W/ m / deg C

h = 3.5e-6;                             % thickness of leg
wh = 3e-6;  wc = 30e-6;                 % widths - leg and shuttle
wp = 30e-6;                             % width of bond pad
tv = 2.0e-6;                            % air gap
tn = 0.6e-6;                            % thick N
t0 = 0.0;                               % there is no oxide layer here
tsub = 500e-6;                          % Estimate of substrate thickness

L = 250e-6;                             % Length of TIM leg
Lc = 50e-6;                             % Length of shuttle
offset = 3e-6;                          % Size of offset

%%%%%%%%%%%%%%%%%%%%%%%%%%%%%%%%%%%%%%%%%%%%%%%%%%%%%%%%%%%%%%%%%%%%%%%%%%%%

%%%%%%%%%%%%%%%%%%
%   INPUT                              %
%%%%%%%%%%%%%%%%%%
Current = .006;                         % AMPS

%%%%%%%%%%%%%%%%%%%%%%%%%%%%%%%%%%%%%%%%%%%%%%%%%%%%%%%%%%%%%%%%%%%%%%%%%%%%
%  CALCULATES OTHER GEOMETRY needed for TIM
%%%%%%%%%%%%%%%%%%%%%%%%%%%%%%%%%%%%%%%%%%%%%%%%%%%%%%%%%%%%%%%%%%%%%%%%%%%%
h_xsection = h*wh;
c_xsection = h*wc;
p_xsection = h*wp;

p_volume = h*wp*delta_x;
h_volume = h*wh*delta_x;
c_volume = h*wc*delta_x;

sa_hot = 2*(h*delta_x) + 2*(wh*delta_x);
sa_cold = 2*(h*delta_x) + 2*(wc*delta_x);
sa_pad = wp*delta_x;

sumt = 2*L+Lc;
sumt2 = 2*L + 2*Lc;
```

```
Leq = sqrt(L^2 + offset^2);
vac_node = ceil(L/delta_x);
air_node = floor((L/delta_x)*.5) + 2;

Ih = (h*wh^3/12);
If = Ih;
Ic = (h*wc^3/12);

I2 = Current^2;
Jh = Current/(h*wh);
Jh2 = Jh^2;
Jc = Current/(h*wc);
Jc2 = Jc^2;

%%%%%%%%%%%%%%%%%%%%%%%%%%%%%%%%%%%%%%%%%%%
%  Model path to substrate and include shape factor
%%%%%%%%%%%%%%%%%%%%%%%%%%%%%%%%%%%%%%%%%%%
Rt = (tv/k_air) + (tn/k_Si3Ni4) + (t0/k_SiO2) + (tsub/k_Si);          % Under leg
Rp = (tn/k_Si3Ni4) + (tsub/k_Si);                                     % Under bond pad

Sh = ((h/wh) * ( ((2*tv)/h) + 1 )) + 1;                               % Shape factors
Sc = ((h/Lc) * ( ((2*tv)/h) + 1 )) + 1;
Ss = ((h/Lc) * ( ((2*tv)/h) + 1 )) + 1;

h_sa_under = Sh*wh*delta_x;
c_sa_under = Sc*wc*delta_x;
p_sa_under = wp*delta_x;

%%%%%%%%%%%%%%%%%%%%%%%%%%%%%%%%%%%%%%%%%%%
%  Analytical solution work begins HERE
%%%%%%%%%%%%%%%%%%%%%%%%%%%%%%%%%%%%%%%%%%%
mh = sqrt( (Sh / (k_polySi*h*Rt)) - ((Jh2*p0*alpha_r) / k_polySi) );
mc = sqrt( (Sc / (k_polySi*h*Rt)) - ((Jc2*p0*alpha_r) / k_polySi) );

Th_theta = T_s + ((Jh^2*p0)/(k_polySi*mh^2));
Tc_theta = T_s + ((Jc^2*p0)/(k_polySi*mc^2));

lamda = wc*mc / (wh*mh);
BIG = [1 1 0 0 0 0;
   exp(mh*L) exp(-mh*L) -exp(mc*L) -exp(-mc*L) 0 0;
   exp(mh*L) -exp(-mh*L) -lamda*exp(mc*L) lamda*exp(-mc*L) 0 0;
   0 0 exp(mc*(L+Lc)) exp(-mc*(L+Lc)) -exp(mh*(L+Lc)) -exp(-mh*(L+Lc));
   0 0 lamda*exp(mc*(L+Lc)) -lamda*exp(-mc*(L+Lc)) -exp(mh*(L+Lc)) …
   exp(-mh*(L+Lc));
   0 0 0 0 exp(mh*(sumt)) exp(-mh*(sumt)) ];
```

```
TEMP = [T_s - Th_theta;
     Tc_theta - Th_theta;
     0;
     Th_theta - Tc_theta;
     0;
     T_s - Th_theta ];

C = inv(BIG)*TEMP;

loc = 0:1e-6:sumt;
for i = 1:(1e6*L)
  T(i) = Th_theta + C(1)*exp(mh*loc(i)) + C(2)*exp(-mh*loc(i));
  if i == (1e6*L)
    T = T';
  end
end
v1 = 1e6*L + 1;
v2 = v1 + 1e6*Lc;
for i = v1:v2
  Z(i) = Tc_theta + C(3)*exp(mc*loc(i)) + C(4)*exp(-mc*loc(i));
  T = [T ; Z(i)];
end
v3 = v2 + 1;
v4 = (1e6*sumt) + 1;
for i = v3:v4
  Z(i) = Th_theta + C(5)*exp(mh*loc(i)) + C(6)*exp(-mh*loc(i));
  T = [T; Z(i)];
end

Tave_h = Th_theta + (C(1)/(mh*L))*(exp(mh*L) - 1) ...
       - (C(2)/(mh*L))*(exp(-mh*L) - 1);
Tave_c = Tc_theta + (C(3)/(mc*Lc))*(exp(mc*(L+Lc)) - exp(mc*L)) ...
       - (C(4)/(mc*Lc))*(exp(-mc*(L+Lc)) - exp(-mc*L));
Tave_h2 = Th_theta + (C(5)/(mh*L))*(exp(mh*(sumt)) - exp(mh*(L+Lc))) ...
       - (C(6)/(mh*L))*(exp(-mh*(sumt)) - exp(-mh*(L+Lc)));

R = ((L*p0)/(wh*h))*(1 + alpha_r*(Tave_h - T_s)) ...
   + ((Lc*p0)/(wc*h))*(1 + alpha_r*(Tave_c - T_s)) ...
   + ((L*p0)/(wh*h))*(1 + alpha_r*(Tave_h2 - T_s));


%%%%%%%%%%%%%%%%%%%%%%%%%%%%%%%%%%%%%%%%%%%%%%%%%%%%%%%%%%%%%%%%%%%%%%%%%%%%
%                                                                             %
%   Finite Difference Solution Starts HERE                                    %
%                                                                             %
%%%%%%%%%%%%%%%%%%%%%%%%%%%%%%%%%%%%%%%%%%%%%%%%%%%%%%%%%%%%%%%%%%%%%%%%%%%%
```

```
% Find number of nodes so matrix sizes do not have to update dynamically in for loops
pad_inc = 20;                                          % Set size of bond pads
no_nodes = round((sumt/delta_x) + 1) + pad_inc;        % Find number of nodes
rows = round((time_final/delta_t) + 2);                % Find number of rows
k = 0;                                          % k is the row space holder for time

% Find Ci's and R's
T_c = zeros([rows no_nodes]);
Cap = zeros([rows no_nodes]);
Joule_heat = zeros([rows no_nodes]);
Sum_resistance_heat_loss = zeros([rows no_nodes]);
Left_cond_R = zeros([rows no_nodes]);
Right_cond_R = zeros([rows no_nodes]);
below_cond_R = zeros([rows no_nodes]);
below_cond_RR = zeros([rows 2]);
below_cond_RL = zeros([rows 2]);
below_cond_RRpad = zeros([rows 2]);
below_cond_RLpad = zeros([rows 2]);

% Initialize variables
P_total = 0;P_gen = 0;E_kept = 0;E_gen = 0;Rij = 0;Rsum = 0;Esum = 0;Loss = 0;
EffJ = [];EffP = [];Rz = [];EffJleg = [];E_in = []; P_in_step = [];
E_in_step = [];E_store_step = [];P_out_env = [];

for p = 0:delta_t:time_final
  k = k+1;
  E_kept = 0;E_gen = 0;Rsum = 0;              % Reset variables HERE with time step
  E_kept_leg = 0;E_gen_leg = 0;
  P_total = 0;P_gen = 0;Ploss_env = 0;
  for i = 1:no_nodes
    if p == 0;
      for z = 1:no_nodes
        T_c(1,z) = T_s;                       %Fill initial time slot with 20 degrees
      end
      k = 2;                        % Then step down a row
      p = p + delta_t;              % and advance time
    end

    if i == 1
      Cap(k,i) = density*(p_volume/2)*therm_capacity;
      Left_cond_R(k,i) = 0;
      Right_cond_R(k,i) = delta_x/(k_polySi*p_xsection);
      below_cond_R(k,i) = (Rp/(p_sa_under/2));
      Right_heat = ((T_c(k-1,i+1) - T_c(k-1,i))/Right_cond_R(k,i));
      T_c(k,i) = T_s;
```

```
elseif i == no_nodes                    % Last node at wall
  Cap(k,i) = density*(h_volume/2)*therm_capacity;
  Left_cond_R(k,i) = delta_x/(k_polySi*p_xsection);
  Right_cond_R(k,i) = 0;
  below_cond_R(k,i) = (Rp/(p_sa_under/2));
  Left_heat = ((T_c(k-1,i-1) - T_c(k-1,i))/Left_cond_R(k,i));
  T_c(k,i) = T_s;

elseif (i < round((pad_inc/2) + 1)) & (i ~= 1) % LeftPad
  Cap(k,i) = density*(p_volume)*therm_capacity;
  Left_cond_R(k,i) = delta_x/(k_polySi*p_xsection);
  Right_cond_R(k,i) = delta_x/(k_polySi*p_xsection);
  below_cond_R(k,i) = (Rp/(p_sa_under));
  Joule_heat(k,i) = 0;
  Left_heat = ((T_c(k-1,i-1) - T_c(k-1,i))/Left_cond_R(k,i));
  Right_heat = ((T_c(k-1,i+1) - T_c(k-1,i))/Right_cond_R(k,i));
  Radiation = (T_sK - (T_c(k-1,i)+Diff))...
    *(sa_hot*(absortivity_polySi*sigma*...
    ((T_c(k-1,i)+Diff) + T_sK)*(((T_c(k-1,i)+Diff))^2 + T_sK^2)));
  Convection = ((T_s - T_c(k-1,i))*sa_pad*h_conv);
  Below_heat = ((T_s - T_c(k-1,i))/below_cond_R(k,i));
  Sum_resistance_heat_loss(k,i) = Left_heat + Right_heat ...
    + (bottom_flag)*Below_heat + (radiate_flag)*Radiation ...
    + (convect_flag)*Convection;
  T_c(k,i) = delta_t/Cap(k,i) * (Joule_heat(k,i) …
    + Sum_resistance_heat_loss(k,i)) + T_c((k-1),i);

elseif (i > no_nodes - round((pad_inc/2))) & (i ~= no_nodes)          % RightPad
  Cap(k,i) = density*(p_volume)*therm_capacity;
  Left_cond_R(k,i) = delta_x/(k_polySi*p_xsection);
  Right_cond_R(k,i) = delta_x/(k_polySi*p_xsection);
  below_cond_R(k,i) = (Rp/(p_sa_under));
  Joule_heat(k,i) = 0;
  Left_heat = ((T_c(k-1,i-1) - T_c(k-1,i))/Left_cond_R(k,i));
  Right_heat = ((T_c(k-1,i+1) - T_c(k-1,i))/Right_cond_R(k,i));
  Radiation = (T_sK - (T_c(k-1,i)+Diff))...
    *(sa_hot*(absortivity_polySi*sigma...
    *((T_c(k-1,i)+Diff) + T_sK)*(((T_c(k-1,i)+Diff))^2 + T_sK^2)));
  Convection = ((T_s - T_c(k-1,i))*sa_pad*h_conv);
  Below_heat = ((T_s - T_c(k-1,i))/below_cond_R(k,i));
  Sum_resistance_heat_loss(k,i) = Left_heat + Right_heat ...
     + (bottom_flag)*Below_heat + (radiate_flag)*Radiation ...
    + (convect_flag)*Convection;
  T_c(k,i) = delta_t/Cap(k,i) * (Joule_heat(k,i) ...
    + Sum_resistance_heat_loss(k,i)) + T_c((k-1),i);
```

```
elseif i == round((pad_inc/2) + 1)                                  % Pad2Hot
  Cap(k,i) = density*(h_volume/2)*therm_capacity ...
  + (density*(p_volume/2)*therm_capacity);
  Right_cond_R(k,i) = delta_x/(k_polySi_get((T_c(k-1,i)+(T_c(k-1,i+1)))/2)...
    *h_xsection);
  Left_cond_R(k,i) = (delta_x/(k_polySi_get((T_c(k-1,i-1)+(T_c(k-1,i)))/2)...
    *p_xsection));
  below_cond_RLpad(k,1) = (Rp/(p_sa_under/2));
  below_cond_RRpad(k,1) = (Rt_temp(T_c(k-1,i)/2)/(h_sa_under/2));
  Right_heat = ((T_c(k-1,i+1) - T_c(k-1,i))/Right_cond_R(k,i));
  Left_heat = ((T_c(k-1,i-1) - T_c(k-1,i))/Left_cond_R(k,i));
  Joule_heat(k,i) = (Jh2*(p0*(1 + alpha_r*(T_c(k-1,i) - T_s)))...
    *(delta_x/2)*h_xsection);
  Radiation = (T_sK - (T_c(k-1,i)+Diff))...
    *(sa_hot*(absortivity_polySi*sigma*((T_c(k-1,i)+Diff) + T_sK)...
    *(((T_c(k-1,i)+Diff))^2 + T_sK^2)));
  Convection = ((T_s - T_c(k-1,i))*(sa_hot/2)*h_conv) ...
    + ((T_s - T_c(k-1,i))*(sa_cold/2)*h_conv);
  Below_heat = ((T_s - T_c(k-1,i))/below_cond_RLpad(k,1)) ...
    + ((T_s - T_c(k-1,i))/below_cond_RRpad(k,1));
  Sum_resistance_heat_loss(k,i) = Left_heat + Right_heat ...
    + (bottom_flag)*Below_heat + (radiate_flag)*Radiation ...
    + (convect_flag)*Convection;
  T_c(k,i) = delta_t/Cap(k,i) * (Joule_heat(k,i) ...
    + Sum_resistance_heat_loss(k,i)) + T_c((k-1),i);

elseif i == (no_nodes - round((pad_inc/2)))                         % Hot2Pad
  Cap(k,i) = density*(h_volume/2)*therm_capacity ...
    + (density*(p_volume/2)*therm_capacity);
  Left_cond_R(k,i) = delta_x/(k_polySi_get((T_c(k-1,i-1)+(T_c(k-1,i)))/2)...
    *h_xsection);
  Right_cond_R(k,i) = (delta_x/(k_polySi_get((T_c(k-1,i)+(T_c(k-1,i+1)))/2)...
    *p_xsection));
  below_cond_RRpad(k,2) = (Rp/(p_sa_under/2));
  below_cond_RLpad(k,2) = (Rt_temp(T_c(k-1,i)/2)/(h_sa_under/2));
  Left_heat = ((T_c(k-1,i-1) - T_c(k-1,i))/Left_cond_R(k,i));
  Right_heat = ((T_c(k-1,i+1) - T_c(k-1,i))/Right_cond_R(k,i));
  Joule_heat(k,i) = (Jh2*(p0*(1 + alpha_r*(T_c(k-1,i) - T_s)))...
    *(delta_x/2)*h_xsection);
  Radiation = (T_sK - (T_c(k-1,i)+Diff))...
    *(sa_hot*(absortivity_polySi*sigma*((T_c(k-1,i)+Diff) + T_sK)...
    *(((T_c(k-1,i)+Diff))^2 + T_sK^2)));
  Convection = ((T_s - T_c(k-1,i))*(sa_hot/2)*h_conv) ...
    + ((T_s - T_c(k-1,i))*(sa_cold/2)*h_conv);
  Below_heat = ((T_s - T_c(k-1,i))/below_cond_RLpad(k,2)) ...
```

```
    + ((T_s - T_c(k-1,i))/below_cond_RRpad(k,2));
  Sum_resistance_heat_loss(k,i) = Left_heat + Right_heat ...
    + (bottom_flag)*Below_heat + (radiate_flag)*Radiation ...
    + (convect_flag)*Convection;
  T_c(k,i) = delta_t/Cap(k,i) * (Joule_heat(k,i) ...
    + Sum_resistance_heat_loss(k,i)) + T_c((k-1),i);

elseif i == round(((L/delta_x) + 1)) + round(pad_inc/2)  % Hot2Cold node
  Cap(k,i) = (density*(h_volume/2)*therm_capacity) ...
    + (density*(c_volume/2)*therm_capacity);
  Left_cond_R(k,i) =  (delta_x/(k_polySi_get((T_c(k-1,i-1)+(T_c(k-1,i)))/2)...
    *h_xsection));
  Right_cond_R(k,i) = (delta_x/(k_polySi_get((T_c(k-1,i)+(T_c(k-1,i+1)))/2)...
    *c_xsection));
  below_cond_RL(k,1) = (Rt_temp(T_c(k-1,i)/2)/(h_sa_under/2));
  below_cond_RR(k,1) = (Rt_temp(T_c(k-1,i)/2)/(c_sa_under/2));
  Joule_heat(k,i) = (Jh2*(p0*(1 + alpha_r*(T_c(k-1,i) - T_s)))*(delta_x/2)...
    *h_xsection) + (Jc2*(p0*(1 + alpha_r*(T_c(k-1,i) - T_s)))...
    *(delta_x/2)*c_xsection);
  Left_heat = ((T_c(k-1,i-1) - T_c(k-1,i))/Left_cond_R(k,i));
  Right_heat = ((T_c(k-1,i+1) - T_c(k-1,i))/Right_cond_R(k,i));
  Radiation = (T_sK - (T_c(k-1,i)+Diff))…
    *(sa_hot*(absortivity_polySi*sigma*((T_c(k-1,i)+Diff) + T_sK)...
    *(((T_c(k-1,i)+Diff))^2 + T_sK^2)));
  Convection = ((T_s - T_c(k-1,i))*(sa_hot/2)*h_conv) ...
    + ((T_s - T_c(k-1,i))*(sa_cold/2)*h_conv);
  Below_heat = ((T_s - T_c(k-1,i))/below_cond_RL(k,1)) ...
    + ((T_s - T_c(k-1,i))/below_cond_RR(k,1));
  Sum_resistance_heat_loss(k,i) = Left_heat + Right_heat ...
    + (bottom_flag)*Below_heat + (radiate_flag)*Radiation ...
    + (convect_flag)*Convection;
  Ploss_env = Ploss_env + (bottom_flag)*Below_heat ...
    + (radiate_flag)*Radiation + (convect_flag)*Convection;
  T_c(k,i) = delta_t/Cap(k,i) * (Joule_heat(k,i) ...
    + Sum_resistance_heat_loss(k,i)) + T_c((k-1),i);

  P_add = therm_capacity*density*wh*h*(delta_x/2)*(T_c(k,i) - T_c(k-1,i))...
     /delta_t + therm_capacity*density*wc*h...
    *(delta_x/2)*(T_c(k,i) - T_c(k-1,i))/delta_t;
  P_comp = Joule_heat(k,i) + Sum_resistance_heat_loss(k,i);
  P_total = P_total + P_add;
  P_gen = P_gen + Joule_heat(k,i); % (W)
  Loss = Loss + Sum_resistance_heat_loss(k,i);
  Energy_in = Joule_heat(k,i)*delta_t;
  E_gen = E_gen + Energy_in;
  Energy_kept = therm_capacity*density*wh*h*(delta_x/2)...
```

```
    *(T_c(k,i) - T_c(k-1,i)) + therm_capacity*density*wc*h...
    *(delta_x/2)*(T_c(k,i) - T_c(k-1,i));
  E_kept = E_kept + Energy_kept;
  Rij = Left_cond_R(k,i) + Right_cond_R(k,i) + below_cond_RL(k,1) ...
    + below_cond_RR(k,1)+ ...
    (1/(sa_hot*(absortivity_polySi*sigma...
    *((T_c(k-1,i)+Diff) + T_sK)*(((T_c(k-1,i)+Diff))^2 + ...
    T_sK^2)))) + (1/((sa_hot/2)*h_conv)) + (1/((sa_cold/2)*h_conv));
  Rsum = Rsum + (1/Rij);

  if delta_t >= Cap(k,i)/(1/Rij)
    warning('Time step problem');
    pause
  end

elseif i == round((((L+Lc)/delta_x) + 1)) + round(pad_inc/2)     % Cold2hot node
  Cap(k,i) = (density*(h_volume/2)*therm_capacity) ...
    + (density*(c_volume/2)*therm_capacity);
  Left_cond_R(k,i) =  (delta_x/(k_polySi_get((T_c(k-1,i-1)+(T_c(k-1,i)))/2)...
    *c_xsection));
  Right_cond_R(k,i) = (delta_x/(k_polySi_get((T_c(k-1,i)+(T_c(k-1,i+1)))/2)...
    *h_xsection));
  below_cond_RR(k,2) = (Rt_temp(T_c(k-1,i)/2)/(h_sa_under/2));
  below_cond_RL(k,2) = (Rt_temp(T_c(k-1,i)/2)/(c_sa_under/2));
  Joule_heat(k,i) = (Jh2*(p0*(1 + alpha_r*(T_c(k-1,i) - T_s)))...
    *(delta_x/2)*h_xsection) + (Jc2*(p0*(1 + alpha_r*(T_c(k-1,i) - T_s)))...
    *(delta_x/2)*c_xsection);
  Left_heat = ((T_c(k-1,i-1) - T_c(k-1,i))/Left_cond_R(k,i));
  Right_heat = ((T_c(k-1,i+1) - T_c(k-1,i))/Right_cond_R(k,i));
  Radiation = (T_sK - (T_c(k-1,i)+Diff))...
    *(sa_hot*(absortivity_polySi*sigma*((T_c(k-1,i)+Diff) + T_sK)...
    *(((T_c(k-1,i)+Diff))^2 + T_sK^2)));
  Convection = ((T_s - T_c(k-1,i))*(sa_hot/2)*h_conv) ...
    + ((T_s - T_c(k-1,i))*(sa_cold)/2*h_conv);
  Below_heat = ((T_s - T_c(k-1,i))/below_cond_RR(k,2)) ...
    + ((T_s - T_c(k-1,i))/below_cond_RL(k,2));
  Sum_resistance_heat_loss(k,i) = Left_heat + Right_heat ...
    + (bottom_flag)*Below_heat ...
    + (radiate_flag)*Radiation + (convect_flag)*Convection;
  Ploss_env = Ploss_env + (bottom_flag)*Below_heat ...
    + (radiate_flag)*Radiation + (convect_flag)*Convection;
  T_c(k,i) = delta_t/Cap(k,i) * (Joule_heat(k,i) ...
    + Sum_resistance_heat_loss(k,i)) + T_c((k-1),i);

  P_add = therm_capacity*density*wh*h*(delta_x/2)*(T_c(k,i) - T_c(k-1,i))...
    /delta_t + therm_capacity*density*wc*h...
```

```
    *(delta_x/2)*(T_c(k,i) - T_c(k-1,i))/delta_t;
  Energy_in = Joule_heat(k,i)*delta_t;
  Energy_kept = therm_capacity*density*wh*h*(delta_x/2)...
    *(T_c(k,i) - T_c(k-1,i)) + therm_capacity*density*wc*h...
    *(delta_x/2)*(T_c(k,i) - T_c(k-1,i));
  P_comp = Joule_heat(k,i) + Sum_resistance_heat_loss(k,i);
  P_total = P_total + P_add;
  P_gen = P_gen + Joule_heat(k,i); % (W)
  Loss = Loss + Sum_resistance_heat_loss(k,i);
  E_gen = E_gen + Energy_in;
  E_kept = E_kept + Energy_kept;
  Rij = Left_cond_R(k,i) + Right_cond_R(k,i) + below_cond_RR(k,2) ...
    + below_cond_RL(k,2) + (1/(sa_hot*(absortivity_polySi*sigma...
    *((T_c(k-1,i)+Diff) + T_sK)*(((T_c(k-1,i)+Diff))^2 ...
    + T_sK^2)))) + (1/((sa_hot/2)*h_conv)) + (1/((sa_cold/2)*h_conv));
  Rsum = Rsum + (1/Rij);

     if delta_t >= Cap(k,i)/(1/Rij)
       warning('Time step problem');
       pause
     end

elseif (i > round(((L/delta_x) + 1))+round(pad_inc/2)) …
       & (i < round((((L+Lc)/delta_x)+1))+round(pad_inc/2) )
  Cap(k,i) = density*c_volume*therm_capacity;
  Left_cond_R(k,i) =  delta_x/(k_polySi_get((T_c(k-1,i-1)+(T_c(k-1,i)))/2)...
    *c_xsection);
  Right_cond_R(k,i) = delta_x/(k_polySi_get((T_c(k-1,i)+(T_c(k-1,i+1)))/2)...
    *c_xsection);
  below_cond_R(k,i) = (Rt_temp(T_c(k-1,i)/2)/(c_sa_under));
  Joule_heat(k,i) = (Jc2*(p0*(1 + alpha_r*(T_c(k-1,i) - T_s)))...
    *delta_x*c_xsection);
  Left_heat = ((T_c(k-1,i-1) - T_c(k-1,i))/Left_cond_R(k,i));
  Right_heat = ((T_c(k-1,i+1) - T_c(k-1,i))/Right_cond_R(k,i));
  Radiation = (T_sK - (T_c(k-1,i)+Diff))...
    *(sa_cold*(absortivity_polySi*sigma...
    *((T_c(k-1,i)+Diff) + T_sK)*(((T_c(k-1,i)+Diff))^2 + T_sK^2)));
  Convection = ((T_s - T_c(k-1,i))*sa_cold*h_conv);
  Below_heat = ((T_s - T_c(k-1,i))/below_cond_R(k,i));
  Sum_resistance_heat_loss(k,i) = Left_heat + Right_heat ...
    + (bottom_flag)*Below_heat + (radiate_flag)*Radiation ...
    + (convect_flag)*Convection;
  Ploss_env = Ploss_env + (bottom_flag)*Below_heat ...
    + (radiate_flag)*Radiation + (convect_flag)*Convection;
  T_c(k,i) = delta_t/Cap(k,i) * (Joule_heat(k,i) ...
    + Sum_resistance_heat_loss(k,i)) + T_c((k-1),i);
```

```
  P_comp = Joule_heat(k,i) + Sum_resistance_heat_loss(k,i); % (W)
  P_add = therm_capacity*density*wc*h*(delta_x)*(T_c(k,i) - T_c(k-1,i))...
    /delta_t; % (W)
  Energy_in = Joule_heat(k,i)*delta_t; % (J)
  Energy_kept = therm_capacity*density*wc*h...
    *(delta_x)*(T_c(k,i) - T_c(k-1,i)); % (J)

  P_total = P_total + P_add; % (W)
  Loss = Loss + Sum_resistance_heat_loss(k,i);
  P_gen = P_gen + Joule_heat(k,i); % (W)
  E_gen = E_gen + Energy_in; % (J)
  E_kept = E_kept + Energy_kept;
  Rij = Left_cond_R(k,i) + Right_cond_R(k,i) + below_cond_R(k,i) + ...
    (1/(sa_cold*(absortivity_polySi*sigma*((T_c(k-1,i)+Diff) + T_sK)...
    *(((T_c(k-1,i)+Diff))^2 + T_sK^2)))) + (1/(sa_cold*h_conv));
  Rsum = Rsum + (1/Rij);

     if delta_t >= Cap(k,i)/(1/Rij)
       warning('Time step problem');
       pause
     end

else                                                    %All HOT nodes
  Cap(k,i) = density*h_volume*therm_capacity;
  Left_cond_R(k,i) =  delta_x/(k_polySi_get((T_c(k-1,i-1)+(T_c(k-1,i)))/2)...
    *h_xsection);
  Right_cond_R(k,i) = delta_x/(k_polySi_get((T_c(k-1,i)+(T_c(k-1,i+1)))/2)...
    *h_xsection);
  below_cond_R(k,i) = (Rt_temp(T_c(k-1,i)/2)/h_sa_under);
  Joule_heat(k,i) = (Jh2*(p0*(1 + alpha_r*(T_c(k-1,i) - T_s)))...
    *delta_x*h_xsection);
  Left_heat = ((T_c(k-1,i-1) - T_c(k-1,i))/Left_cond_R(k,i));
  Right_heat = ((T_c(k-1,i+1) - T_c(k-1,i))/Right_cond_R(k,i));

  Radiation = (T_sK - (T_c(k-1,i)+Diff))...
    *(sa_hot*(absortivity_polySi*sigma*((T_c(k-1,i)+Diff) + T_sK)...
    *(((T_c(k-1,i)+Diff))^2 + T_sK^2)));
  Convection = ((T_s - T_c(k-1,i))*sa_hot*h_conv);
  Below_heat = ((T_s - T_c(k-1,i))/below_cond_R(k,i));
  Sum_resistance_heat_loss(k,i) = Left_heat + Right_heat ...
    + (bottom_flag)*Below_heat + (radiate_flag)*Radiation ...
    + (convect_flag)*Convection;
  Ploss_env = Ploss_env + (bottom_flag)*Below_heat ...
    + (radiate_flag)*Radiation + (convect_flag)*Convection;
  T_c(k,i) = delta_t/Cap(k,i) * (Joule_heat(k,i) ...
```

```
        + Sum_resistance_heat_loss(k,i)) + T_c((k-1),i);

      P_comp = Joule_heat(k,i) + Sum_resistance_heat_loss(k,i);  % Units are (W)
      P_add = therm_capacity*density*wh*h*(delta_x)...
        *(T_c(k,i) - T_c(k-1,i))/delta_t; % Units are (W)
      P_total = P_total + P_add; % (W)
      P_gen = P_gen + Joule_heat(k,i); %  (W)
      Loss = Loss + Sum_resistance_heat_loss(k,i);
      Energy_in = Joule_heat(k,i)*delta_t; % Units are (J)
      Energy_kept = therm_capacity*density*wh*h*(delta_x)*(T_c(k,i) - T_c(k-1,i));
      E_gen = E_gen + Energy_in;  % Energy IN: THIS time step by Joule heating
      E_kept = E_kept + Energy_kept; % Energy kept (J)
      E_gen_leg = E_gen_leg + Energy_in; % (J)
      E_kept_leg = E_kept_leg + Energy_kept; % (J)

      Rij = Left_cond_R(k,i) + Right_cond_R(k,i) + below_cond_R(k,i) + ...
        (1/(sa_hot*(absortivity_polySi*sigma*((T_c(k-1,i)+Diff) + T_sK)...
          *(((T_c(k-1,i)+Diff))^2 + T_sK^2)))) + (1/(sa_hot*h_conv));
      Rsum = Rsum + (1/Rij);

        if delta_t >= Cap(k,i)/(1/Rij)
          warning('Time step problem');
          i
          k
          pause
        end
    end

  end

  Esum = Esum + E_gen;
  P_in_step = [P_in_step; P_gen];
  E_in = [E_in; Esum];
  E_in_step = [E_in_step; E_gen];
  E_store_step = [E_store_step; E_kept];
  P_out_env = [P_out_env; Ploss_env];

  Ratio1 = P_total/P_gen;
  Ratio2 = E_kept/E_gen;
  Ratio3 = E_kept_leg/E_gen_leg;                    % Same as Ratio2 but just legs

  EffJleg = [EffJleg ; Ratio3];  % Step
  EffJ = [EffJ ; Ratio2];  %Step
  EffP = [EffP ; Ratio1];  %Step pw

end
```

```
losses = sum(Sum_resistance_heat_loss');
Esum = 1000*Esum;
P_in_step = 1000*P_in_step;
E_in = 1000*E_in;
E_in_step = 1000*E_in_step;
E_store_step = 1000*E_store_step;
P_out_env = 1000*P_out_env;

EffJ = 100*EffJ;
EffJleg = 100*EffJleg;
EffP = 100*EffP;
nodes = 1:no_nodes;
prep = -1*(1 - nodes);
unodes = round((delta_x/1e-6)*prep);
[m,n] = size(T_c);

[Y,I] = max(T_c(m,:));

%%%%%%%%%%%%%%%%%%%%%%%%%%%%%%%%%%%%
% Compute growth of one leg on one side
%%%%%%%%%%%%%%%%%%%%%%%%%%%%%%%%%%%%
growth = zeros(m,1);   %0;
Temp_ave = zeros(m,1);
Temp = 0;
T_sub = T_s + 273.15;

for z = 1:m
 for i = round((pad_inc/2) + 1):round(((L/delta_x) + 1)) + round(pad_inc/2)
   temperature = T_c(z,i) + 273.15;
   lamda = polySi_expan(temperature);

   if i == round((pad_inc/2) + 1)
      growth(z) = growth(z) + (lamda*(delta_x/2)*(temperature - T_sub));
      Temp = Temp + T_c(z,i);
   elseif i == round(((L/delta_x) + 1)) + round(pad_inc/2)
      growth(z) = growth(z) + (lamda*(delta_x/2)*(temperature - T_sub));
      Temp = Temp + T_c(z,i);
   else
      growth(z) = growth(z) + (lamda*delta_x*(temperature - T_sub));
      Temp = Temp + T_c(z,i);
   end
 end
 Temp_ave(z) = Temp / round(((L/delta_x)+1));
 Temp = 0;
end
```

```
%%%%%%%%%%%%%%%%%%%%%%%%
% MAX displacement with no bending
%%%%%%%%%%%%%%%%%%%%%%%%
for z = 1:m
  ux(z) = sqrt((Leq + growth(z))^2 - (L^2));
  ux_total(z) = 1e6*(ux(z) - offset);
end
max = ux_total(m)



%%%%%%%%%%%%%%%%%%%%%%%%%%%%%%%%%%%%%%%%
% PRBM for displacement
%%%%%%%%%%%%%%%%%%%%%%%%%%%%%%%%%%%%%%%%
gam = .82;
[gr,place] = max(growth);
Lt = Leq*1e6;
gr = gr*1e6;
grow = 1e6*growth;

for z = 1:m
  Ln = Leq + growth(z);
  x2 = 1 + ((L^2)/offset^2);
  x1 = -2*Ln + 2*Ln*gam - (2*Leq*(L^2))/offset^2;
  x0 = -2*(Ln^2)*gam + Ln^2 + ((L^2)*(Leq^2))/offset^2;
  coef = [x2 x1 x0];
  a = roots(coef);
  move2(z) = 1e6*(L*a(1)/offset - L*Leq/offset);
end
prbd_d2 = move2(m)

%%%%%%%%%%%%%%%%%%%%%%%%
% Graph stuff is here
%%%%%%%%%%%%%%%%%%%%%%%%
if bottom_flag == 0    % or vacuum environment
  figure(1)
  plot(unodes,T_c(m,:),'+:');
  axis([0 1e6*(no_nodes*delta_x-delta_x) 0 1500]);
  xlabel('Location (\mum)');
  ylabel(' Temperature \circC');
  title('Temperature distribution across TIM');
else
  figure(1)
  plot(1e6*(loc+pad_inc*delta_x/2),T,unodes,T_c(m,:),'+:');
  axis([0 1e6*(no_nodes*delta_x-delta_x) 0 1500]);
```

```
   xlabel('Location  (\mum)');
   ylabel(' Temperature  \circC');
   title('Temperature distribution across TIM');
end
p = 0:delta_t:(time_final + delta_t);
if bottom_flag == 0  % or vacuum env.
   figure(2)
   subplot(2,1,1)
   plot(1e3*p,Temp_ave,'-');
   axis([0 tf_ms 0 1000]);
   ylabel('Ave. Temperature  \circC');
   xlabel('Time (ms)');
   title('Temperature Transient and Efficiency');
   subplot(2,1,2)
   pp = delta_t:delta_t:(time_final + delta_t);
   plot(1e3*pp,EffJ,'-',1e3*pp,EffJleg,'--');
   ylabel('Efficiency %');
   xlabel('Time (ms)');
   axis([0 tf_ms 0 100]);
else
   figure(2)
   subplot(2,1,1)
   plot(1e3*p,Temp_ave,'-');
   axis([0 tf_ms 0 1000]);
   ylabel('Ave. Temperature \circC');
   xlabel('Time (ms)');
   title('Temperature Transient and Efficiency');
   subplot(2,1,2)
   pp = delta_t:delta_t:(time_final + delta_t);
   plot(1e3*pp,EffJ,'-',1e3*pp,EffJleg,':');
   legend('Step E','Step E leg',0);
   ylabel('Efficiency as %');
   xlabel('Time (ms)');
   axis([0 tf_ms 0 100]);
end

figure(3)
plot(1e3*p,move2)
xlabel('Time (ms)');
ylabel('Displacement \mum');
title('Predicted Displacement with time from PRBM');
axis([0 tf_ms 0 18]);

he = sum(Joule_heat');           % gets pw in at each time step
hes = he * 1000;         % convert to mW
volts = he / Current;
```

```
figure(4)
subplot(2,1,1)
plot(1e3*p,hes)
xlabel('Time (ms)');
ylabel('Heating Power (mW)');
subplot(2,1,2)
plot(1e3*p,volts);
xlabel('Time (ms)');
ylabel('Voltage requirements (Volts)');

figure(5)
subplot(2,1,1)
plot(1e3*pp,P_in_step)
xlabel('Time  (ms)');
ylabel('Step Power (mW)');
subplot(2,1,2)
plot(1e3*pp,E_in)
xlabel('Time  (ms)');
ylabel('Integrated Energy  (mJ)');

figure(6)
subplot(2,1,1)
plot(1e3*pp,E_store_step)
xlabel('Time  (ms)');
ylabel('Energy kept at time step (mJ)');
subplot(2,1,2)
plot(1e3*pp,abs(P_out_env))
xlabel('Time  (ms)');
ylabel('PWR loss to ENV during each time step (mW)');
```

APPENDIX B

```
! ANSYS Input file for MEMS-TIM
!
! Used to Create the TIM Geometry
! Takes nodal temperatures form finite-difference solution
! And Solves Structural Problem Directly
!
! All dimensions uMKSV
!
/FILNAME,TIM_oneleg
/TITLE,MEMS: TIM fundamental beam
!
/PREP7
!
! Parameters
!
hot_w=3              ! Width of hot leg beam
hot_l=250            ! Length of hot leg beam
offset=3             ! Offset length
mid_l=50             ! Length of shuttle
mid_w=30             ! Width of shuttle
poly_t=3.5           ! Thickness of device
roomt=20             ! Room temperature
delta_x = 10
!
TREF,roomt
! Create geometry
K,,0,0,0                          ! k#1
K,,hot_l,offset,0                 ! k#2
K,,hot_l+mid_l,offset,0           ! k#3
K,,(2*hot_l)+mid_l,0,0            ! k#4
!
!
LSTR,1,2                          ! line 1
LSTR,2,3                          ! line 2
LSTR,3,4                          ! line 3
!
/PNUM,LINE,1                      ! Turns on num/colors for line
```

```
LPLOT                          ! Displays the selected lines
NUMCMP,LINE                    ! Renumber lines from low to high - no gaps
!
! Material properties for Polysilicon
! In uMKSV UNITS
!
MPREAD,linRconsKfullX,mp,,
!
ET,1,3                                                          ! beam3 DOF's
R,1,hot_w*poly_t,poly_t*hot_w*hot_w*hot_w/12,hot_w              !x-section in hot leg
R,2,mid_w*poly_t,poly_t*mid_w*mid_w*mid_w/12,mid_w              !x-section in shuttle
!
! Assign attributes to lines
!
LSEL,s,line,,1
LSEL,a,line,,3
!
LATT,1,1,1,0,,,
LSEL,INVE
LATT,1,2,1,0,,,
ALLSEL,ALL
/REPLOT
!
! Mesh
!
LESIZE,1,,,hot_l/delta_x,1,
LESIZE,3,,,hot_l/delta_x,1,
LSEL,s,line,,1
LSEL,a,line,,3
LMESH,all
LSEL,inve
LESIZE,2,,,mid_l/delta_x,1,
LMESH,all
LSEL,all
/REPLOT
!
FINISH
!
! Apply boundary conditions & loads
!
/SOLU
DDELE,all
LSCLEAR,all
DK,1,ALL,0
DK,4,ALL,0
!
```

```
! PUT IN DATA FROM MATLAB HERE
! BF,NODE,TEMP,VALUE
!
BF,1,TEMP,27.4100
BF,3,TEMP,125.5304
BF,4,TEMP,210.1663
BF,5,TEMP,283.0752
BF,6,TEMP,345.7733
BF,7,TEMP,399.5664
BF,8,TEMP,445.5767
BF,9,TEMP,484.7660
BF,10,TEMP,517.9546
BF,11,TEMP,545.8382
BF,12,TEMP,569.0026
BF,13,TEMP,587.9346
BF,14,TEMP,603.0328
BF,15,TEMP,614.6155
BF,16,TEMP,622.9267
BF,17,TEMP,628.1421
BF,18,TEMP,630.3717
BF,19,TEMP,629.6628
BF,20,TEMP,626.0004
BF,21,TEMP,619.3075
BF,22,TEMP,609.4428
BF,23,TEMP,596.1986
BF,24,TEMP,579.2958
BF,25,TEMP,558.3787
BF,26,TEMP,533.0074
BF,2,TEMP,502.6491
BF,53,TEMP,500.4947
BF,54,TEMP,498.3403
BF,55,TEMP,498.3403
BF,56,TEMP,500.4947
BF,27,TEMP,502.6491
BF,29,TEMP,533.0074
BF,30,TEMP,558.3787
BF,31,TEMP,579.2958
BF,32,TEMP,596.1986
BF,33,TEMP,609.4428
BF,34,TEMP,619.3075
BF,35,TEMP,626.0004
BF,36,TEMP,629.6628
BF,37,TEMP,630.3717
BF,38,TEMP,628.1421
BF,39,TEMP,622.9267
BF,40,TEMP,614.6155
```

```
BF,41,TEMP,603.0328
BF,42,TEMP,587.9346
BF,43,TEMP,569.0026
BF,44,TEMP,545.8382
BF,45,TEMP,517.9546
BF,46,TEMP,484.7660
BF,47,TEMP,445.5767
BF,48,TEMP,399.5664
BF,49,TEMP,345.7733
BF,50,TEMP,283.0752
BF,51,TEMP,210.1663
BF,52,TEMP,125.5304
BF,28,TEMP,27.4100
!
PSTRES,on
SOLCONTROL,on
NLGEOM,ON
TOFFSET,273
TIME,2
DELTIM,0.1
SOLVE
FINISH
! Get max deflection from nodal solution (sort)
/POST1
NSORT,u,y,0,0
*set,maxdisp,0
*get,maxdisp,sort,0,max
FINISH
!
/SOLU
!
DL,2,,uy,maxdisp*.95
LSWRITE,2
DL,2,,uy,maxdisp*.90
LSWRITE,3
DL,2,,uy,maxdisp*.85
LSWRITE,4
DL,2,,uy,maxdisp*.80
LSWRITE,5
LSSOLVE,2,5,1                ! More load steps can be added as desired
!
FINISH
!
/POST1
etable,temp,lbfe,1
ETABLE,smxi,NMISC,1
```

```
ETABLE,smxj,NMISC,3
ETABLE,smni,NMISC,2
ETABLE,smnj,NMISC,4
/plopts,minm,0
/triad,off
PLNSOL,u,y
PLETAB,temp,noave
!
LSEL,s,,,2
NSLL,S,1
*get, n1, node, 0, num, min
*get, n2, node, n1, NXTH
*get, n3, node, n2, NXTH
*get, n4, node, n3, NXTH
*get, n5, node, n4, NXTH
*get, n6, node, n5, NXTH
!
/POST26
NUMVAR,20
NSOL,2,n4,U,Y,uy
RFORCE,3,n1,F,Y,fy1
RFORCE,4,n2,F,Y,fy2
RFORCE,5,n3,F,Y,fy3
RFORCE,6,n4,F,Y,fy4
RFORCE,7,n5,F,Y,fy5
RFORCE,8,n6,F,Y,fy6
Add,9,3,4,5,add1
add,10,9,6,7,add2
add,11,10,8,,addall
/output,results
PRVAR,2,11
/output
FINISH
```

LinRconsKfullX.mp

```
/COM,ANSYS RELEASE  5.5.3  UP19990405       11:53:43    08/29/2000
MPTEMP
MPTEMP,1,0.0000000E+00,
MPDATA,EX,1,1,0.1600000E+06,
MPTEMP
MPTEMP,1, 0.0000000E+00,
MPDATA,NUXY,1,1,0.2300000E+00,
MPTEMP
MPTEMP,1,0.200000E+02,0.200000E+03,0.400000E+03,0.700000E+03,0.100000E+04
MPTEMP,6,0.1400000E+04,
MPDATA,ALPX,1,1,0.25100E-05,0.35094E-05,0.39510E-05,0.42396E-05,0.44270E-05
MPDATA,ALPX,1,6,0.4652900E-05,
MPTEMP
MPTEMP,1,0.0000000E+00,
MPDATA,DENS,1,1,0.2330000E-14,
MPTEMP
MPTEMP,1,0.0000000E+00,
MPDATA,KXX,1,1,0.3200000E+08,
MPTEMP
MPTEMP,1,0.200000E+02,0.200000E+03,0.400000E+03,0.700000E+03,0.100000E+04
MPTEMP,6,0.1400000E+04,
MPDATA,RSVX,1,1,0.24000E-10,0.29400E-10,0.35400E-10,0.44400E-10,0.53400E-10
MPDATA,RSVX,1,6, 0.6540000E-10,
MPTEMP
MPTEMP,1, 0.0000000E+00,
MPDATA,C ,1,1, 0.7050000E+15,
```